THE UNIVERSITY OF CHICAGO

REINING CHAOS: UNDERSTANDING AND MANIPULATING THE MICROSCOPIC UNDERPINNINGS OF TURBULENT FLOWS IN A MODEL OF COLLECTIVE MOTION

A DISSERTATION SUBMITTED TO
THE FACULTY OF THE DIVISION OF THE PHYSICAL SCIENCES
AND
THE FACULTY OF THE DIVISION OF THE BIOLOGICAL SCIENCES
AND THE PRITZKER SCHOOL OF MEDICINE
IN CANDIDACY FOR THE DEGREE OF
DOCTOR OF PHILOSOPHY

GRADUATE PROGRAM IN BIOPHYSICAL SCIENCES

BY
STEVEN ALDEN REDFORD

CHICAGO, ILLINOIS
AUGUST 2023

Dedicated to Heather Redford (1958-2012). Her boundless joy and indomitable courage taught me how to live.

"If we knew what it was we were doing, it would not be called research, would it?"

-Albert Einstein

TABLE OF CONTENTS

LIST OF FIGURES

ACKNOWLEDGMENTS

I am indebted to so many incredible collaborators and friends who have stood by me throughout the years. The science I completed here would not have been possible without Nitin Kumar, Rui Zhang, Danielle Schef, Yashar Bashirzadeh, Wen-hung Chou, Jordan Shivers, Cal Floyd, and Sasha Zemsky. I am especially grateful to Paul Ruijgrok for providing not only amazing tools but also vital expertise. Jonathan Colen has been a constant friend and invaluable sounding board. Chatipat Lorpaiboon bailed me out more than once when I was in beyond my depth. Mehdi Molaei is one of the most brilliant and best people I know. I am honored to call him a friend. Margaret Gardel and Aaron Dinner have been the mentors I needed scientifically. They gave me the space to follow my curiosity and learn all that I could.

In addition to scientific support I am incredibly grateful to the friends who have kept me sane and happy these years. Meike and Emily have been with me since literally day one. The Sunday dinner crew Matt, Florian, Iva, Fernando, and Jimmy kept me fed. Casey, Sabina, and Donald kept me grounded. My quarantine pod Devin, Vaughn, Cat, Evan, and Kourtney kept me sane while the world went up in flames. Liz de Laittre has done nothing less than teach me how to love and for that I am ever grateful.

ABSTRACT

Active materials are those in which individual, uncoordinated local stresses drive the material out of equilibrium on a global scale. Examples of such assemblies can be seen across scales from schools of fish to the cellular cytoskeleton and underpin many important biological processes. Synthetic experiments that recapitulate the essential features of such active systems have been the object of study for decades as their simple rules allow us to elucidate the physical underpinnings of collective motion. One system of particular interest has been active nematic liquid crystals (LCs). Because of their well understood passive physics, LCs provide a rich platform to interrogate the effects of active stress. The flows and steady-state structures that emerge in active LCs have been understood to result from a competition between nematic elasticity and the local activity. However most investigations of such phenomena consider only the magnitude of the elastic resistance and active drive and not their microscopic origins. In this thesis we utilize experiments as well as computer simulations and novel analytical techniques to investigate how the microscopic origins of activity and elasticity in a LC affect the resultant flow. Specifically we query a liquid crystal composed of short actin filaments – the load bearing protein fibers inside of cells – that are driven by myosin motors. We show that by limiting motor activity to one region of the LC we can constrain and direct otherwise chaotic flows. We show that increases in the nematic's bend elasticity caused by alterations in filament length drive the material into an exotic steady state where "elasticity bands" dominate the structure and dynamics. Furthermore, we introduce a novel analytical technique that extends the method of correlation functions to measure material responses from experimental data. Finally, we show that the very nature of the action of a molecular motor inextricably couples activity and material elasticity.

CHAPTER 1

INTRODUCTION

Non-equilibrium systems are an important frontier in science. Not only does some of our basic physical intuition break down far from equilibrium but life, as the famous saying goes, does not exist at equilibrium. Understanding the essential physics of out of equilibrium systems provides insight into not only abiological phenomena but also provides a window into the physical constraints within which life has evolved. Amongst the many ways a system can leave equilibrium one of the most fascinating and visually striking is the independent motion of many constituents (Ramaswamy [2010]). In biology this type of phenomenon is exemplified by flocks of birds or schools of fish (Cavagna and Giardina [2014], Marchetti et al. [2013]). While in these systems evolved behavior plays a large role in the dynamics, purely physical models can recapitulate the long range order and coherent motion of biological flocks (Nitin Kumar and Sood [2014]). Understanding, then, what rules govern abiological flocking provides insight into the limitations and possibilities about which these behaviors evolved. The possible dynamical states for such physical systems in which many components move independently – termed active matter – are myriad from dynamical phase separation to giant number fluctuations and turbulent flows (Wensink et al. [2012], Ramaswamy et al. [2003], del Junco et al. [2018]). The particular phenomena a specific active matter system exhibits is determined largely by its underlying symmetry and hydrodynamic milieu (Giomi [2013], Marchetti et al. [2013]).

A great deal of theoretical and experimental work over the past few decades have shed much light onto how these different contributions affect flows (Doostmohammadi et al. [2016], Duclos et al. [2017]). However while many hydrodynamic scale properties of these systems are well understood there are gaps in our knowledge. In particular the multi-scale nature of active problems means that it is difficult to map the microscopic properties of individual components on to longer, much more well understood scales

(Gao et al. [2015]). In order to address this multi-scale problem, we will couple experimental perturbations of LC dynamics with simulaiton methodologies at multiple scales. Specifically, in this thesis we utilize nematic liquid crystals composed of short actin filaments that are driven by various forms of the molecular motor mysoin as an exceptionally tunable active material within which we may begin to map the microscopic properties of an active system onto the hydrodynamic picture of its mesoscopic flows.

Actin is a naturally occurring semi-flexible protein polymer, which can be found inside of cells from bacteria to humans (Gardel et al. [2004]). Actin architectures provide structure for cells as well as a template for ATP consuming myosin motors to impart force and induce motion (Hotulainen and Lappalainen [2006], Tojkander et al. [2012]). As it underpins cellular motility the interaction between actin and myosin is one of the most fundamental active processes in biology. Constructing an active material from these components provides insight into this fundamental interaction as well as fluid immersed active materials as a whole. The typical dynamics of actomyosin active materials are largely dictated by the length of the actin filaments. When long actin filaments and myosin motors are combined in vitro filament buckling results in irreversible contraction (Murrell and Gardel [2012], Stam et al. [2017]). Such an outcome, while interesting in and of itself, has limited applicability to the study of active materials as a whole as the system never reaches steady state. One way to overcome this limitation is to limit the length of filaments via the addition of the naturally occurring F-actin capping protein (Palmgren et al. [2001]). When actin is limited to around two micrometers it behaves essentially as a rigid rod (Zhang et al. [2017]). These rods do not buckle under myosin stress. Instead the actomyosin forms an extensile nematic liquid crystal (Kumar et al. [2018]). Nematic liquid crystals, or simply nematics, are formed when many elongated components interact at sufficient concentration such that excluded volume interactions cause components to align along their long axis (Gennes and Prost [1993]). This alignment begets a state with

long-range structure in which individual elements can still flow past each other. This combination of structure and fluidity is the hallmark of a liquid crystal.

Liquid crystals are an incredibly useful system in which to ask questions about active matter as their equilibrium physics is well characterized. Since we are interested in nonequilibrium phenomenon it behooves us to study a system in which the equilibrium behavior is well characterized. That way when we push it out of equilibrium we know how the passive forces in the system relax internal stress. We will have much to say about the precise forces at work throughout this thesis, but for now let us summarize the essentials. Without the addition of any activity, liquid crystal structure is dictated by two vital quantities; elasticity and viscosity. Because of the alignment of individual components, a liquid crystal resists long-range distortions to the field with an effective elastic constant (Zhang et al. [2017], Doostmohammadi et al. [2018]). The upshot of such elasticity is that if we were to leave an initially disordered liquid crystal for a long time we would find that it approaches a state where every individual filament is aligned with every other filament. The rate at which the system approaches this lowest-energy state is dictated by the magnitude of the elastic constant and its viscosity (Gennes and Prost [1993], Thampi et al. [2014b]). Nematic elasticity and viscosity are the passive forces against which activity in the liquid crystal pushes. In the case of actin and myosin, activity is generated by the sliding of adjacent filament pairs which results in the net extension of the ends of the pairs relative to each other (Giomi [2015]). Thus we can schematize the action of a myosin motor as generating dipolar force pointing along the local direction of the liquid crystal. We term this outward force extensile stress. Thus we refer to a collection of short actin filaments driven by myosin motors as an extensile liquid crystal. Actin and myosin are a particularly attractive system within which to probe the basis of nematic dynamics as each component is highly tunable. In particular, changing the concentration of capping protein varies the length distribution of filaments within the liquid crystal while advances

in the engineering of synthetic myosin motors allow specific control of individual motor properties (Schindler et al. [2014], Nakamura et al. [2014], Zhang et al. [2017]). These tools allow us to query exactly how filament length or motor properties affect the long-range flows produced in the nematic.

In this thesis we utilize actin based nematic liquid crystals as a system in which to test how microscopic properties of system components effect flows in active systems. Specifically we utilize motors that change their speed in response to optical stimulation to show how spatially varied activity can be utilized as an engineering tool to harness otherwise chaotic active flows. We then utilize the flexibility afforded by our actin based material to systematically alter the length of the filaments that compose the liquid crystal and demonstrate that in the long filament limit a dynamical state emerges that is dominated by material bending deformations independent of the type of motor used to drive said deformations. In order to further understand the turbulent flows produced in an active liquid crystal we also introduce a novel analytical method that recasts correlation functions such that they capture the local material response to a specific perturbation. Finally we bring to bear all of our insights into active liquid crystals and demonstrate through controlled perturbations to the driving myosin that the modality of activity in these systems – the sliding of filament pairs by myosin motors– inherently links active drive and passive material properties through motor cross-linking. Altogether then our results, while focused around extensile liquid crystals, provide tools and important conceptual frameworks with which to understand other active systems.

CHAPTER 2

SPATIOTEMPORAL CONTROL OF LIQUID CRYSTAL STRUCTURE AND DYNAMICS THROUGH ACTIVITY PATTERNING

2.1 Introduction

Soft materials in which individual components convert ambient free energy into mechanical work are commonly referred to as active matter (Marchetti et al. [2013], Ramaswamy [2010]). These systems are compelling in that their relatively simple rules of propulsion and inter-particle interactions can give rise to intriguing collective behaviours and pattern formation across length scales (Vicsek and Zafeiris [2012], Sokolov et al. [2019a]). Active components underpin coherence in a wide range of natural processes. They play a critical role in cellular migration, flocking and long-range flows in dense bacterial suspensions (Saw et al. [2017], Kawaguchi et al. [2017], Bricard et al. [2013], Nitin Kumar and Sood [2014], Dombrowski et al. [2004], Li et al. [2019]). These behaviours are not just interesting in and of themselves, but hold promise as the basis for the design of novel, functional materials (Vizsnyiczai et al. [2017], Needleman and Dogic [2017]). The central challenge of engineering functionality in active materials is that active flows are often turbulent (Sanchez et al. [2012], Wensink et al. [2012], Giomi et al. [2014], Zhou et al. [2014], Ellis et al. [2018]). Efforts to control these flows thus far have utilized physical boundaries to constrain the material, and rely on spontaneous symmetry breaking to yield steady states and coherent dynamics over large scales (Keber et al. [2014], Guillamat et al. [2016], Wu et al. [2017], Opathalage et al. [2019], Duclos et al. [2018]). While these works have demonstrated that a degree of control in active systems is indeed possible, the dependence on physical barriers and spontaneous symmetry breaking limits the amount of control that can be exerted. We seek a different control parameter with which we may direct the flow and dynamics of an active material without the malice of forethought. Ideally, this more

flexible control parameter could direct the material asymmetrically and thus allow for the programming of more complex behaviours in active systems. In this chapter, we introduce spatially dependent activity as this flexible control parameter, and demonstrate both in experiment and simulations how it can be leveraged to direct defect dynamics and control long-range flows in an active nematic liquid crystal.

2.2 Results

2.2.1 High activity regions in nematics are self-contained

Nematic liquid crystals (nematics) are a phase of matter in which extended components — mesogens — align along their long axis to form a material with long-range orientational order, but which can flow like a liquid (Gennes and Prost [1993]). Structural disorder in these systems is stored in distinct regions of discontinuity termed topological defects (Gennes and Prost [1993]). In two dimensions, topological defects carry a 'charge' of either $+\frac{1}{2}$ or $-\frac{1}{2}$, defined by the winding number about the defect core (Fig. 1a). When extensile stress is introduced along the orientation of the mesogens, the asymmetric $+\frac{1}{2}$ defects are propelled along their axis of symmetry (Giomi [2013]). The interplay between the active and elastic stress leads to a steady-state nucleation, motion and annihilation of defects, resulting in a state known as 'active turbulence' (Giomi [2015], Wensink et al. [2012], Doostmohammadi et al. [2018]). One useful class of active liquid crystals is those formed by cytoskeletal polymers (Sanchez et al. [2012], Kumar et al. [2018]). Activity is readily introduced to these systems via the addition of molecular motor proteins that slide adjacent filaments past each other, thereby generating extensile stresses along the nematic orientation (Thampi et al. [2013b]). In this work we construct a nematic liquid crystal by crowding short (1 μm in length) actin filaments (F-actin) onto an oil–water interface (Kumar et al. [2018]) (Fig. 1b). Because of the fluorescent dye and the polarized

laser used in these experiments, filaments that are vertical in the experimental frame appear brighter than those which are horizontal. Thus, pixel intensity tells us about the local orientation of the nematic field (Kinosita et al. [1991], Sase et al. [1997]) (see Fig. 1a and Methods section). While previous realizations of cytoskeletal liquid crystals have harnessed the power of naturally occurring motor proteins (Sanchez et al. [2012], Wu et al. [2017], Kumar et al. [2018]), in this work we produce spatially structured activity by exploiting motor proteins engineered with light-dependent gliding velocities (Nakamura et al. [2014], Ruijgrok et al. [2021]). This strategy is distinct from that employed in earlier work, where optically controlled reversible cross-linking of motors or inhibitor deactivation was used to induce stress in cytoskeletal assemblies (Ross et al. [2019], Linsmeier et al. [2016]). The light-activated gear-shifting myosin motors used here are constructed from myosin XI catalytic heads and a lever arm containing the light-sensitive LOV2 domain. The stimulated unfolding of this LOV2 domain changes the geometry and effective length of the lever arm, conferring optical modulation of motor velocity on the biopolymer F-actin (Nakamura et al. [2014]). To generate local stress on antiparallel F-actin, engineered oligomerization domains are utilized to create motor tetramers (Ruijgrok et al. [2021], Schindler et al. [2014]) (Fig. 1c). These tetramers, when added to actin liquid crystals, produce higher defect densities and a greater average nematic speed upon stimulation. To target this increase in activity to just one region of the liquid crystal a micromirror array is used to selectively target the stimulation wavelength of 470 nm to one portion of the sample, while confocal fluorescence imaging is used to visualize fluorescently tagged actin. We selectively illuminate a large region (2,000 μm^2) (Fig. 1d, red box) in a liquid crystal containing gear-shifting motors. Upon stimulation, the density of topological defects remains low outside of the stimulated region while the activity within leads to defect proliferation (Fig. 1d, yellow circles). This transition from low to high defect density is sharp, occurring within several micrometres of the boundary (Fig. 1e). Moreover,

the nematic spontaneously flows within the illuminated region, with an instantaneous velocity that is threefold larger than that outside the bounds (Fig. 1f). While large when compared with the unstimulated region, this flow is hampered when compared with an unconstrained nematic driven by the same motors. That defect density and nematic velocity sharply decrease as one leaves the stimulated region implies a sort of confinement of activity within the stimulated region. This confinement can be visualized by tracking the location of $+\frac{1}{2}$ defects over time. These trajectories are largely contained within the illuminated region over 400s, only rarely crossing over from one region to another (Fig. 1g). This observation holds promise for engineering applications, particularly for the control of individual defect dynamics. Consider the example in Fig. 1h: as the defect approaches the border it is deflected. That is, it undergoes a sharp reorientation such that it never crosses the boundary. This implies that a judicious choice of border geometry could allow for the design of motile defect trajectories. This key observation motivated us to explore the extent to which patterned activity could be harnessed to control the proliferation and deflection of defects in active nematics. With this, we envision the capability to arbitrarily pattern active flows and manipulate transport.

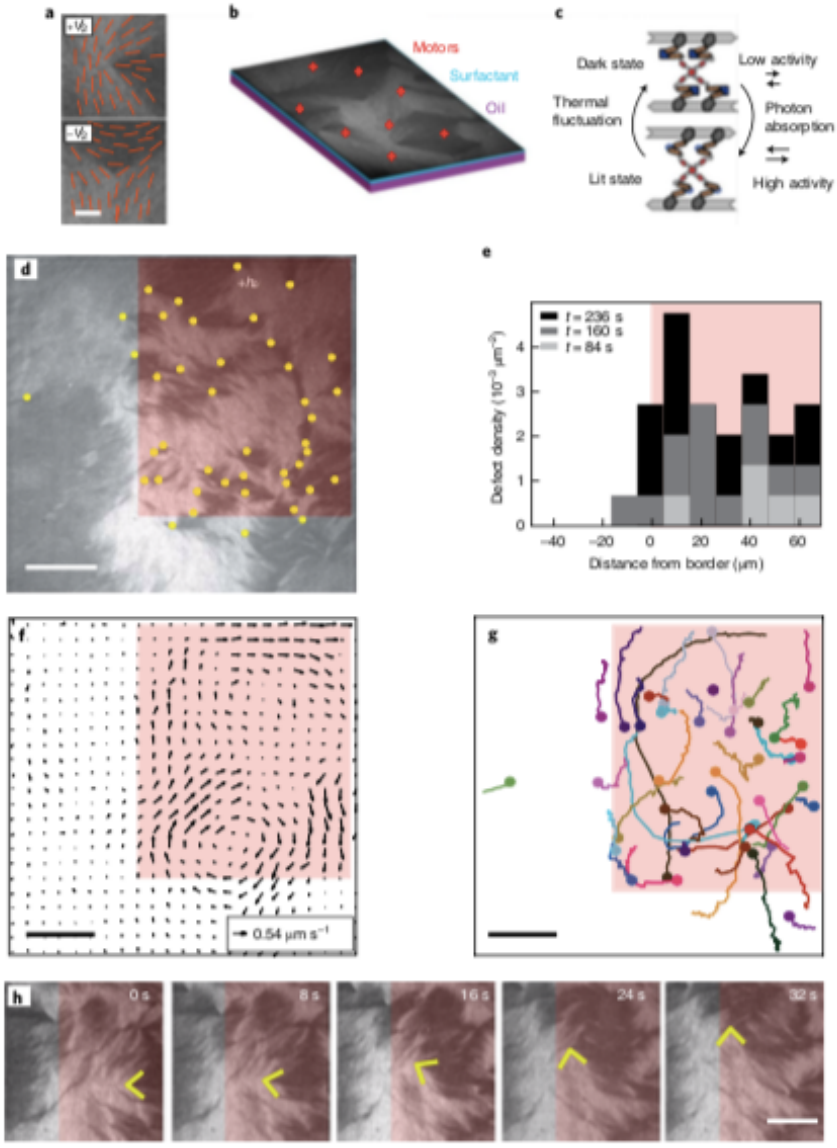

Figure 2.1: **Patterning activity in an actin liquid crystal leads to spatially confined flows and topological defects.** A) Polarization image of actin filaments forming a $+\frac{1}{2}$ (top) and $-\frac{1}{2}$ (bottom) defect. Brighter (darker) pixels in the image are regions in which filaments are vertical (horizontal). Red lines indicate the local average orientation of filaments (director). Scale bar, $5\mu m$. B) Schematic of the experimental setup. Actin is crowded onto an oil–water interface by methylcellulose (not pictured) where engineered myosin motors generate active stress. C) Schematic illustrating the gear-shifting motors. The tetrameric myosin motors are constructed with engineered lever arms that contain the light-sensitive LOV2 domain from Avena sativa. Top (dark state): in the absence of blue light, the LOV2 domain adopts a folded conformation (blue squares), acting as a mechanical element with some rigidity. Bottom (lit state): upon absorption of 470 nm light (downward kinetic arrow) part of the LOV2 undocks and becomes disordered, now acting as a flexible linker

(blue linkages). The undocked LOV2 reverts back to the folded conformation in a thermally activated process (upward kinetic arrow), with motors re-populating the dark state. The light-dependent conformational changes of the lever arm alter the working stroke of the motors; in the context of cross-linked actin filaments we propose that this results in a higher sliding velocity in the lit state ('high activity') than in the dark state ('low activity'), corresponding to the velocity change seen in gliding filament assays Ruijgrok et al. [2021]. D) Experimental polarization microscopy snapshot of fluorescently tagged actin driven by MyLOVChar4 1R TET. Gear-shifting motors were stimulated only within the red box labelled '$+h\nu$'. Topological defects as described above are indicated by yellow dots. Scale bar $20\mu m$. E) Histogram of snapshots of the defect density along the x-axis over time shown in (D). Darker colours indicate later time points. F) Velocity field corresponding to the frame in (D). Scale bars in (F) and (G) $20\mu m$. G) The $+\frac{1}{2}$ defect trajectories for the first 400s of stimulation for the experiment excerpted in (D). H) Example of a trajectory in which a defect 'deflects' off of the boundary of the stimulated region. The defect is marked by a yellow chevron. Scale bar 10 μm.

2.2.2 Relative activity is key for defect confinement

The above experimental observations demonstrate how the difference between the activity in the stimulated and unstimulated regions can be used to spatially confine topological defects. To further understand the extent and utility of such an effect for the precise control of defects, we turn to comprehensive hydrodynamic simulations of active liquid crystals. Our model is based on a Q-tensor representation of the nematic liquid crystal that incorporates hydrodynamic interactions (Beris and Edwards [1994], Marenduzzo et al. [2007b]). The activity α is introduced as a local force dipole such that the active stress in an incompressible active liquid crystal is $\Pi = -\alpha Q$ (Aditi Simha and Ramaswamy [2002]). Previously, we and others have considered α to be constant (Giomi [2013], Kumar et al. [2018], Thampi et al. [2013a], Marenduzzo et al. [2007a], Zhang and Pablo [2016]). We now consider α as a spatial variable, which gives rise to a new stress term due to the gradient of α. Here, a hybrid lattice Boltzmann approach is used to solve the governing equations (see the Simulation model section). This method has been shown to be successful in capturing active nematic behaviours over a range of activities (Kumar et al. [2018], Zhang and Pablo [2016]), including the high activity 'active turbulent' regime in which

topological defects are continuously generated, propelled and annihilated to generate chaotic-like flows (Wensink et al. [2012], Giomi [2015], Doostmohammadi et al. [2018]). While more work is needed to quantitatively relate α to the biophysical properties of actomyosin motors, our experiments show that when optogenetic myosins are switched between low-velocity and high-velocity states, the resulting characteristics of the nematic are consistent with increasing α (Kumar et al. [2018]). As such, we can rely on nematohydrodynamic simulations to explore how spatial variation in activity can be used as a tool to control active matter.

We first consider a nematic comprised of two regions of differing activity, α_1 and α_2, with a flat interface at $x = 0$. For $x < 0$ the nematic has a uniform activity of magnitude α_1, and for $x > 0$ the activity is α_2. Figure 2a,b shows snapshots of the dynamic steady-state configurations of the nematic order (lines) and instantaneous velocity, respectively, for simulations with $\alpha_1 = 0.0001$ and $\alpha_2 = 0.005$. All simulation data are shown in lattice units where the unit length is chosen to be the mesogen length (see the Simulation model section). We identify an interfacial region $x_1 \leq x \leq x_2$ within which the $-\frac{1}{2}$ defect density deviates from that expected for an active nematic of uniform activity equivalent to α_1 and α_2; that is, for $x > x_2$ the $-\frac{1}{2}$ defect density equals that for a bulk nematic with activity α_2 (Fig. 2c). As in experiment, the trajectories of the $+\frac{1}{2}$ defects created in the $x > 0$ region rarely cross into the low activity region $x < 0$ (Fig. 2d). To consider the transition between these two regions, we plot the spatial profile of the both $+\frac{1}{2}$ and $-\frac{1}{2}$ defects across the interface (Fig. 2c). In simulations where $\alpha_1 = 0.0001$ and $\alpha_2 = 0.005$ the density profile for $-\frac{1}{2}$ topological defects exhibits a pronounced peak near the interface. By contrast, the distribution function for $+\frac{1}{2}$ defects is flatter and extends into the less active side. The accumulation of defects at the interface gives rise to a topological-charge dipole moment, similar to a recent theoretical calculation for a dry active nematic (Shankar and Marchetti [2019]), and not unlike that encountered at the interface between

charged species of different dielectric permittivity (Shen et al. [2017]). As defects try to cross from a high (α_2) to a low (α_1) active region, they lose mobility and appear to experience an elastic attraction from the opposite-charge defects in the active region. This prevents them from straying deeper into the low-activity side. To quantify the sharpness of these defect-density distributions, we identify the transition region, $w_\rho = x_2 - x_1$, the ends of which are those points where the defect density deviates from that expected for a nematic with uniform activity (Fig. 2d). This width, w_ρ, is effectively a measure of the confinement induced by the difference in activity at the interface.

To determine how changes in relative activity impact confinement, we explore how the width of the transition region varies as a function of α_1, for simulations with fixed $\alpha_2 = 0.005$. We find that w_ρ is of the same order of magnitude, and approximately 100-fold that of the nematic coherence length (the liquid crystal's intrinsic length scale that is associated with its defect core size), for all relative activities $\frac{\alpha_1}{\alpha_2} < 0.5$ (Fig. 2e). As α_1 approaches α_2, the interfacial width w_ρ increases (see Fig. 2e). Likewise, for a given set of activities, the interfacial width is also quite sensitive to the friction, increasing as the friction is decreased. Thus, both friction and relative activity can be tuned to construct a sharp interface for defect confinement. Note that friction is introduced by the viscous damping of the flow by the confining surfaces where there is a no-slip hydrodynamic boundary condition. This is equivalent to setting a length scale beyond which hydrodynamic forces are screened. One could imagine that this might cor- respond to the amount of fluid that an experimental sample advects due to the thickness of the sample.

In simulations, we also find that the emergence of defect confinement is accompanied by a preferential mesogen orientation perpendicular to the boundary, creating a so-called 'anchoring effect' driven by activity gradients. As seen in Fig. 2a, the directors on the low-activity side adopt a normal orientation to the interface. To characterize the anchoring near to and at the interface, we define an order parameter, $P_2(n \cdot \nu) = \langle 3(n \cdot \nu)^2 - 1 \rangle / 2$

, where n is the director field, ν is the interfacial normal of the activity boundary, and $\langle\rangle$ denotes an ensemble average. At $x = 0$, no anchoring is observed for any relative activity levels (Fig. 2f, blue squares). However, at $x = x_1$, normal anchoring becomes prominent for relative activitiesless than 0.1 when the interface is prominent (Fig. 2f, red triangles). Thus, a sharp gradient in activity simultaneously constrains defects to the region of higher activity and anchors the director field in the low-activity region in the direction normal to the interface. Together, these results further suggest that structured activity is a means to control nematics regionally, at scales much larger than the defect spacing, potentially providing more flexibility than that previously demonstrated with physical barriers (Wu et al. [2017], Opathalage et al. [2019]).

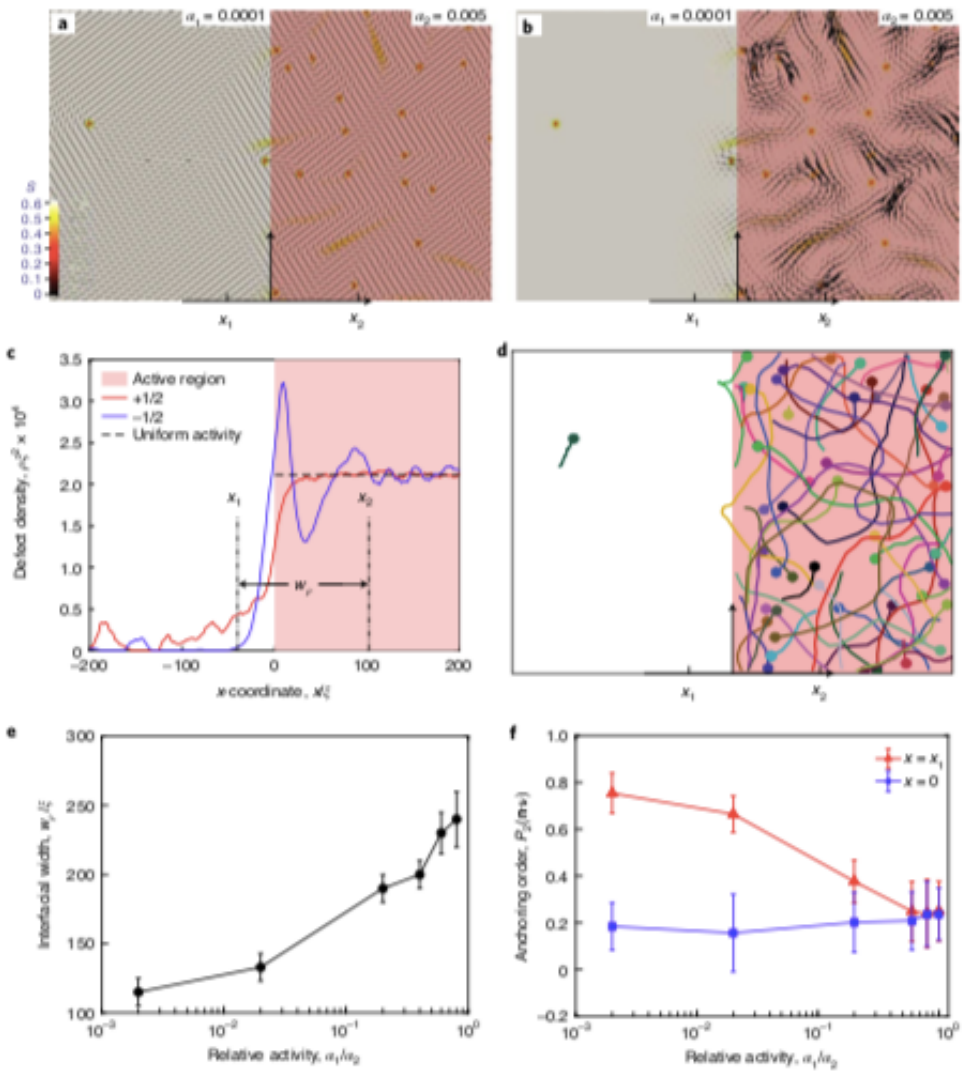

Figure 2.2: **Simulations of defect behaviour in a patterned active nematic.** A-D) Snapshot of the director field near the boundary between the higher and lower activity regions, located at $x = 0$ (A), its corresponding velocity field (B), defect density profile (averaged over ten ensembles of duration $1,000\tau$) (C) and defect trajectories (D). The active region is coloured light red in a–c. The background in (A,B) is coloured with the nematic order parameter S, with dark red indicating defect locations. E) Defect density interfacial width, w_ρ, as a function of relative activity, $\frac{\alpha_1}{\alpha_2}$. F) Scalar order parameter $P_2(n \cdot \nu)$ characterizing the anchoring effect at different locations with respect to the boundary of the activity pattern. The error bars in (E) and (F) represent the standard deviations over 100 ensembles.

2.2.3 *Structured stresses can yield controlled defect nucleation*

We next use simulations to explore the minimum length scale at which structured activity can be used to manipulate liquid crystals. In particular, the extent to which spatially structured activity can be utilized to create and manipulate defects. In nematics with homogeneous activity, defect creation arises from instabilities in bending undulations (Giomi et al. [2014], Thampi et al. [2013a]). The level of active stress sets the undulation wavelength λ and, therefore, sets a length scale required for defect nucleation (Giomi [2013]). We first consider the effects of adding activity ($\alpha = 0.03$) within a rectangular region, with dimensions slightly larger than this natural length scale $\sqrt{\frac{K}{\alpha}}$, with K being the elastic constant, in an initially uniform nematic (Fig. 3a, inset). Because of the mirror or D_2 symmetry of the rectangular pattern, the resulting elastic distortions and hydrodynamic flows preserve such symmetry. Therefore, two bending undulations emerge at the two sides of the activity pattern with equal strength. Each of them gives rise to a pair of $\pm\frac{1}{2}$ defects simultaneously (Fig. 3a). The direction of the initial undulations can be understood by analysing the contribution of the activity gradient at the defect pattern. Note that for an even higher activity level, more than two defect pairs can be generated using this activity pattern. While creating defects in this manner is promising, we desire asymmetric control such that we can create single pairs of defects. To break the symmetry of the rectangle, we consider a triangular region with a base b and height h of similar dimensions to the rectangle (Fig. 3b). In what follows, the length unit ξ of these dimensions is omitted for conciseness. Here, activity-induced bending instabilities incline towards the triangle tip and lead to the formation of a single pair of $\pm\frac{1}{2}$ defects. To determine how defect-pair creation depends on the triangle size and activity level, we perform simulations over a range of activities and pattern size b, for a given aspect ratio $\frac{h}{b} = 3$. For a given size b, we map out the threshold activity required to generate a defect pair (Fig. 3c). When $b > 50$, the pattern becomes sufficiently large that it surpasses the bending

undulation wavelength in a uniform nematic (Fig. 3c, dashed line). Here the threshold level of activity, α_0, required to generate a defect pair is similar to that found in a nematic with homogeneous activity and, as may be expected, more than one defect pair can be created. For $b < 50$, the activity level required to generate a defect pair increases as the required length scale decreases (Fig. 3c, red triangles). However, we find the stress needed is less than would be required for defect generation in the absence of structured activity (Fig. 3c, filled black circles). Indeed, the activity gradient creates an additional stress that contributes to defect nucleation. By changing the geometry of the pattern, the threshold activity of defect generation can be varied. Thus, a judicious choice of activity and geometry allows for control of the nematic field at the scale of individual topological defects.

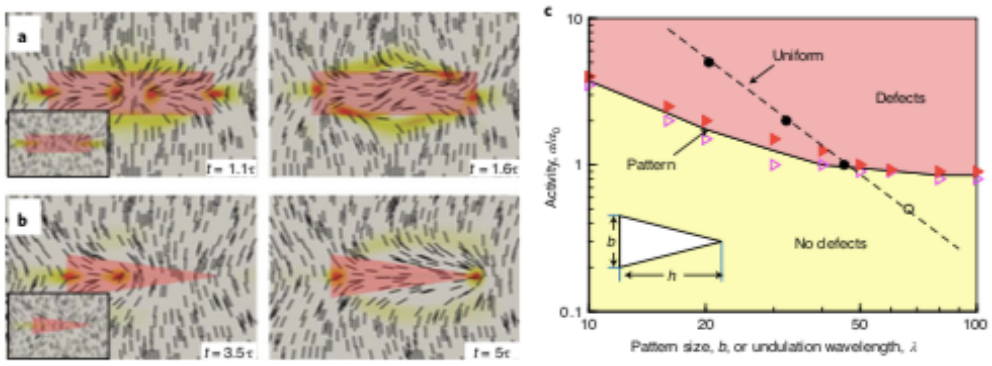

Figure 2.3: **Simulations of defect-pair creation using activity pattern.** A,B) Sequential images of an initially uniform active nematic with a rectangular (A) and a triangular (B) pattern at an activity level $\alpha = 3\alpha_0$. Initial configurations are shown in the insets of (A) and (B). The triangular (rectangular) region has a base (height) $b = 14$ and a height (width) $h = 50$. C) Threshold activity for different pattern sizes at a fixed aspect ratio $\frac{h}{b} = 3$ is shown as triangle symbols. Spontaneous undulation wavelengths at a given activity are shown as circle symbols. Open symbols indicate no defect generation; filled symbols indicate defect generation.

2.2.4 *Confinement affords control of defect trajectories*

Having demonstrated the potential for control over defect creation, we next use simulations to consider the extent to which local activity gradients can control the movement of pre-existing defects. First, we consider a passive nematic in which a $+\frac{1}{2}$ defect is oriented towards a $-\frac{1}{2}$ defect and is separated by a distance $d = 250$, as shown in Fig. 4a. With this geometry, a low amount of uniform activity ($\alpha = 0.2\alpha_0$, where α_0 denotes the activity required to nucleate a defect pair) induces the horizontal motion of the $+\frac{1}{2}$ defect owing to the asymmetric distribution of active stress (Giomi [2013]). Eventually, this leads to annihilation of the defect pair. It is therefore of interest to explore how activity gradients could drive motion that deviates from this behaviour. Using the same initial conditions, we selectively activate a rectangular region of dimensions $290x80$ around the $+\frac{1}{2}$ defect and consider the effect of rotating the rectangle by an angle ϕ. In Fig. 4a, we show a time sequence of the simulations for $\phi = 45^\circ$ and show that the $+\frac{1}{2}$ defect reorients to follow

the long axis of the rectangle and deflects its trajectory. This is consistent with the defect deflection observed experimentally (Fig. 1g). Next, we explore how varying the angle ϕ impacts defect trajectories: we find that defects are faithfully guided up to a threshold angle of 60° (Fig. 4b). Above this, defects are no longer reoriented by the patterned activity (Fig. 4c, purple triangles). We then consider how this threshold angle depends on the active stress by systematically varying the activity. Because an activity value greater than α_0 will result in defect creation and not simply redirection, we consider only activities that are less than α_0. When the activity is increased from $0.2\alpha_0$ to $0.3\alpha_0$ and $0.5\alpha_0$, the threshold angle decreases to 45 and 30°, respectively. This can be understood both by the increased defect speed at higher activities and by the effect of activity on the local bend distortion that limits the reorientation of the $+\frac{1}{2}$ defect. Thus, as the structured activity approaches α_0, the ability to manipulate individual $+\frac{1}{2}$ defects becomes limited. Together with Fig. 3, these data demonstrate how the shape and magnitude of structured activity can be exploited for individual defect generation and manipulation.

To experimentally test for control over individual defects, we construct quarter-annulus regions in which we stimulate the local activity (Fig. 5a). We performed these experiments under conditions resulting in a low defect density, and no creation of defects upon light stimulus. We start with a $+\frac{1}{2}$ defect at the top left and find that the defect moves and reorients as it follows the pattern (Fig. 5a). This motion results in the defect travelling to the other side of the pattern, rotated 90° from its initial alignment (see Fig. 5a). This behaviour can be recapitulated both in simulations and in a number of independent samples (Fig. 5b,c). In the case of simulations, one can directly see that the pattern alters the defect's trajectory from what it would be in the case of uniform activity. Furthermore, the rotation angle probability density function (PDF) of experimental defects in this pattern shows a pronounced, asymmetric peak (Fig. 5d), which indicates that, for the five independent defects considered here, the annulus indeed imposes a preferred turn

angle on defects within the region (Burov et al. [2013]). This is in sharp contrast with a similar histogram constructed from the trajectories obtained from full field activation, which shows a relatively uniform, and notably symmetric, distribution at a number of time lags (see Fig. 5e). The observation that the trajectories from the annulus pattern produce a markedly asymmetric angle-change distribution, while a large stimulated region begets a relatively symmetric PDF, provides further evidence that defects are constrained and directed by the pattern. Such defect deflection events, predicted in simulations and observed in experiments, can be understood theoretically by considering the energetic contribution of an activity gradient at the pattern boundary.

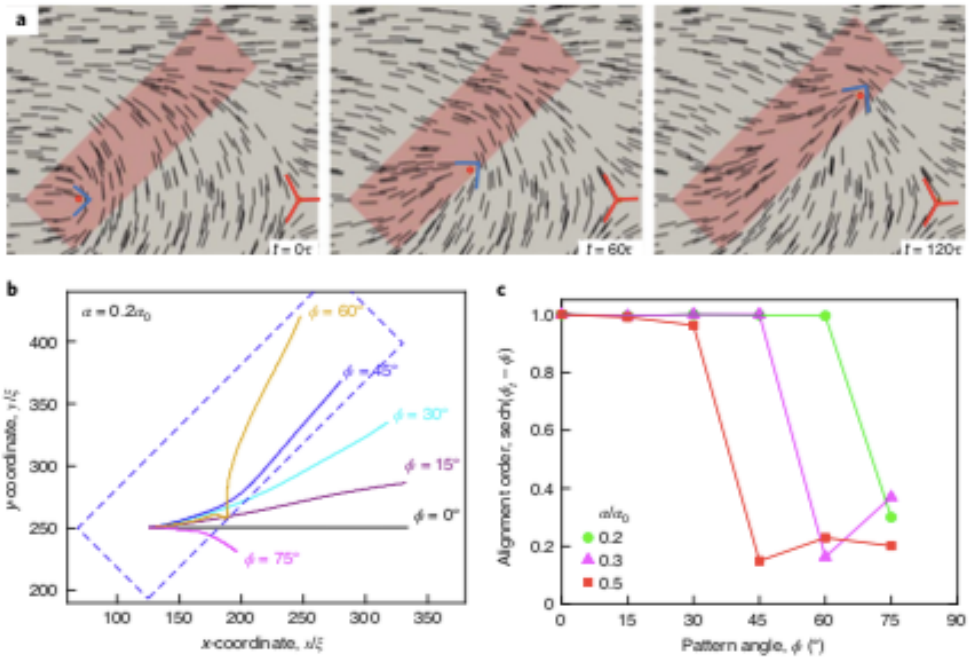

Figure 2.4: **Simulations of defect deflection by a rectangular activity pattern.** A) Sequential images showing defect deflection at activity $\alpha = 0.2\alpha_0$ and box tilt angle $\phi = 45°$. Initial defect separation is 250. A rectangle size (290 × 80) is chosen such that the pattern length can cover the two defects when horizontally placed, and the width is neither too narrow, so that the activity can still drive the defect, nor too wide so as to lose guidance. Defects are marked to aid the eye. B) Defect trajectories for different tilt angles at $\alpha = 0.2\alpha_0$. The activity pattern is shown as a dashed box for $\phi = 45°$. C) The aligning order parameter $sech(\phi_t - \phi)$ as a function of the imposed angle ϕ for various activities where ϕ_t is the angle of the asymptotic trajectory with respect to $+x$.

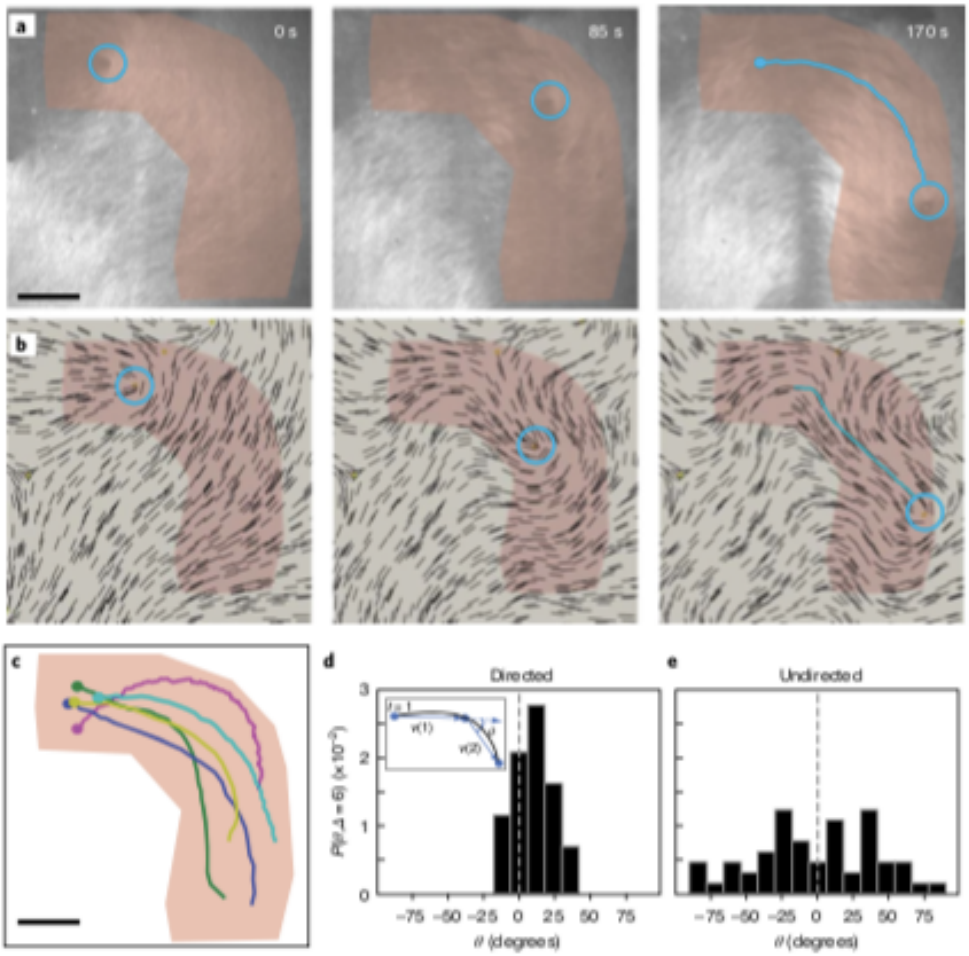

Figure 2.5: **Targeted activation can be used to direct defect trajectories in experiment and simulation.** A) Series of experimental images showing a $+\frac{1}{2}$ defect (circled in blue) moving within the active pattern (red outline). The trajectory of the defect is shown as a tail on the defect in the last frame. B) Series of snapshots from simulations showing the motion of a defect in an activity pattern that mimics the experiment shown in (A). C) Trajectories for five independent experimental samples from two different days (scatterplot) in relation to the activated region. D) PDF for a given change in vector angle, θ, for the trajectories in (C). Inset is a schematic of the method for quantifying the angle change. The grey dashed line indicates an angle of 0°. E) PDF of change in vector angle. The time lag in both (D) and (E) is $25s$, see Methods for a full treatment of the turn angle. Scale bars are $20\mu m$.

2.3 Conclusions

Spatially structured activity presents a promising direction for engineering structure and transport in an active matter at multiple length scales. For one, defects, and the flows they generate, can be confined on a scale larger than the average defect spacing. This results in steady-state defect-density distributions and promises the types of confined flows seen throughout this work. However, the main promise of this approach is not its ability to merely control bulk flow, but its theoretical specificity at a smaller scale. The number and distribution of defects are key state variables of any nematic system. The ability to specifically nucleate a single defect pair and similarly to be able to manipulate the positions of pre-existing defects are steps along the road to controlling these variables. One could imagine composing these two operations spatially to arbitrarily control the entire nematic director. On a wider scale, the flexibility of spatially structured activity is what excites us the most when thinking of its applications in active systems in general. The ability to exert control in both space and time and across length scales opens the door for programming complex behaviours into active systems. Experimentally, future instances of this system may be tuned by making use of optogenetic motors with varied modulation depths (Nakamura et al. [2014], Ruijgrok et al. [2021]), or by taking advantage of the dose-dependent responses of populations of motors to select sub-maximal activation levels (Ruijgrok et al. [2021]). One can imagine leveraging such temporal and spatial control of activity to achieve complex transport tasks or induce novel non-equilibrium steady states. Much work has yet to be done to exert such truly multi-scale control, but we hope that the results presented here may serve as the groundwork for future endeavours.

2.4 Methods

2.4.1 Protein purification

Monomeric actin was purified from rabbit skeletal muscle acetone powder (Pel-Freez Biologicals) as described previously Spudich and Watt [1971] and stored in G-buffer (2 mM Tris buffer pH 8, 0.2 mM ATP, 0.5 mM dithiothreitol, 0.1 mM CaCl2, 1 mM NaN3, pH to 8). Actin was labelled with tetramethylrhodamine — 6 — maleimide (TMR; Life Technologies). F-actin Capping Protein (CP) was a gift from the laboratory of D. Kovar and was purified according to the method in ref. Palmgren et al. [2001]. The optically gear-shifting engineered tetrameric myosin motors were the based on the myosin XI construct MyLOVChar4 1R TET described in ref. Ruijgrok et al. [2021], and a variant with the same lever-arm structure but with mutations to an actin-binding loop in the catalytic domain of myosin XI (MyLOVChar4$_{L2(+4)}$ 1R TET). The mutations introduce four positive charges to actin-binding loop 2, denoted as the mutation L2(+4) in ref. Ito et al. [2009], modifying the wild-type loop sequence FPADEGT**K**APS**K**FMSIG into

FPADEG*GG****KK***G*G*T**K**APS**K***KK*FMSIG (with positive charges in bold, altered amino acids in italic). These mutations to loop 2 have been reported to result in an eightfold increase of apparent actin binding affinity in actin-activated ATPase assays, and a four-fold decrease of velocity in gliding motility assaysIto et al. [2009]. The myosin proteins were purified as described Ruijgrok et al. [2021], flash frozen in small aliquots and stored at $-80°C$. Upon removal from the $-80°C$ freezer, aliquots were used immediately as described below. The myosin constructs include a HaloTag and were labelled with the Alexa 660 fluorophore during purification (Halotag Alexa Fluor 660 Ligand, Promega).

2.4.2 *Assay conditions*

Actin filaments were polymerized at a concentration of 2 μM in 50 μl of various assay buffers. All experiments contained oxygen-scavenging reagents [2.7 mg ml^{-1} glucose oxidase (catalogue no. 345486, Calbiochem), 1700 U ml^{-1} catalase (catalogue no. 02071, Sigma), 4.5 mg ml^{-1} glucose, 0.5% v/v β-mercaptoethanol, prepared at 50× in 1x F-buffer and 2% glycerol] and 0.3% w/v methylcellulose (viscosity 15 cP) as a crowding agent. Experiments were buffered with either F-buffer (10 mM imidazole, 1 mM MgCl2, 50 mM KCl, 0.2 mM egtazic acid, pH 7.5) (Fig. 1) or F-buffer-HEPES (10 mM HEPES, 1 mM MgCl2, 50 mM KCl, 0.2 mM egtazic acid, 1 mM imidazole, pH 7.5) (Fig. 5) with 100 μm ATP, in the presence of 20 nM CP. The actin mixture that was polymerized contained a 1:5 ratio of TMR-labelled to unlabelled monomers. To ensure that the polymerization was complete, mixtures were incubated on ice for one hour before imaging. The imaging chamber was created by first rinsing a small glass cloning cylinder (catalogue no. 09-552-20, Corning) with ethanol and then attaching it to an activated coverslip with two-part epoxy resin. To prevent the actin from sticking and to maintain fluidity the coverslip was first coated with a thin layer of Novec 7500 Engineered Fluid (3M) that included PFPE-PEG-PFPE surfactant (catalogue no. 008, RAN Biotechnologies) at 2% w/v to stabilize the oil–water interface. To coat the chamber, 4 μl of the oil and surfactant mixture was pipetted into the bottom of the chamber and then quickly removed. To minimize evaporation, the polymerized actin and methylcellulose mixture was quickly added to the coated chamber. After addition, the actin mixture was allowed to sit for 20 min so that the actin was given time to crowd onto the oil–water interface and form the liquid crystal. Gear-shifting motors MyLOVChar4 1R TET (Fig. 1) were first diluted into F-buffer and then pipetted directly into the sample chamber. MyLOVChar4 1R TET motors (Fig. 5) were diluted fivefold into 1x F-buffer-HEPES and 5% v/v glycerol. Two microlitres of this dilution was pipetted into the sample chamber.

The sample was imaged using an Eclipse-Ti inverted microscope (Nikon) in confocal mode utilizing a spinning disk (CSU-X; Yokagawa Electric) and a CMOS camera (Zyla-4.2 USB 3; Andor). The experiment in Fig. 1 was imaged using a ×60, 1.20 numerical aperture multi-immersion objective (Nikon) whereas the data in Fig. 5 were collected using a ×40, 1.15 numerical aperture water immersion objective (Nikon). The TMR fluorophore was excited using a 561 nm continuous wave fibre laser (VFL-P series; MPB Communications) at a rate of one frame every four seconds (for ×60 experiments) or one frame every five seconds (for ×40 objective experiments). Microscope components were controlled via the software package MetaMorph (Molecular Devices). Activation was achieved by illuminating the sample with a 400 mW, 470 nm light-emitting diode (ThorLabs) targeted to the region outlined in red in Figs. 1 and 5 using a mosaic micromirror array (Andor). During the period of activation the sample was exposed to the activation wavelength continuously for two seconds of the four-second frame rate or for three seconds of the five-second frame rate.

2.4.3 Image and data analysis.

Velocity fields were calculated using the method of optical flow detailed in ref. Sun et al. [2010] using the Matlab code available at (https:// ps.is.mpg.de/code/secrets-of-optical-flow-code-for-various-methods) and the 'classic+nl-fast' method. Velocity plots were generated using Matlab. The defect density and defect trajectories were plotted using the Matplotlib library in Python. The PDF of the relative angle change given a time lag was calculated using the method detailed in ref. Burov et al. [2013] with a modified definition of the angle. To summarize, we first construct the vector $V(t,\Delta) = X(t+\Delta) - X(t)$ from the trajectory of a defect given by $X(t)$. The angle between adjacent vectors is calculated as $\theta = \sin^{-1}\left(\frac{(V(t,\Delta)xV(t+\Delta,\Delta))\cdot\hat{z}}{(|V(t)||V(t+1)|)}\right)$ where $(V(t,\Delta)xV(t+\Delta,\Delta))\cdot\hat{z}$ denotes the magnitude of the cross product, $|V(t)|$ denotes the Euclidean norm, and $\sin^{-1}$ denotes

the inverse sine function. The probability density of θ is shown in Fig. 5c,d with $n = 15$ bins evenly spaced between -90 and 90°. The velocity correlation length is calculated as $\xi = \int dr \frac{\nu_i(0), \nu_j(r)}{|\nu_i||\nu_j|}$ where i,j denotes the inner product.

2.4.4 Defect localization and tracking.

In two dimensions, the core of a defect is a point where we cannot define the local director field, which is the average orientation of all filaments in that region and is denoted by the unit vector $\hat{n}$. The charge of a defect is given by $\frac{1}{2}\oint_{\pi} d\phi$, where ϕ is the angle between $\hat{n}$ and a reference vector. 2π The intensity of any given pixel in the image is given by $I_i = I_0 + cos^2(\phi_i - \omega)$, where $\omega$is the angle of the polarization of the laser, ϕ_i is the angle of the local director field and I_0 accounts for the fact that orthogonal directions do not truly exhibit zero intensity. The cosine squared function induces a symmetry such that two angles at the same distance from the polarization axis (that is, $\theta \pm \epsilon$) exhibit the same intensity. Because of this polarization symmetry, assigning a director field to every pixel algorithmically is difficult. Thus, in this work we focus instead on the position of defects, which can be readily identified because they are surrounded by all angles of the director field and thus both the highest and lowest pixel intensities in the frame. Defects in these movies have a characteristic shape and look like triangular wedges of either bright (dark) pixels extending into a patch of dark (bright) pixels. We can assign charge by considering the wedge. If the intensity of the wedge indicates that the filaments in this region are aligned along (against) the axis of the wedge, the defect in question carries a charge of $+1/2(-1/2)$. Defects are tracked manually using the manual tracking plugin in ImageJ (https://imagej.nih. gov/ij/plugins/track/track.html, 2005 version).

Active Nematohydrodynamics and Lattice Boltzmann Simulation

Simulation data for training and testing was generated using a hybrid lattice Boltzmann method which has been used in prior studies of active nematics Zhang et al. [2017], Kumar et al. [2018], Zhang et al. [2016]. The symmetric and traceless tensorial order parameter of the nematic is defined as

$$\mathbf{Q} = S(\mathbf{nn} - \mathbf{I}/3) \tag{2.1}$$

with S being the scalar order parameter, $\mathbf{n}$ being the unit vector describing the local nematic orientation, and $\mathbf{I}$ being an identity tensor. The following governing equation of the nematic microstructure, namely Beris-Edwards equation (2.2) reads

$$(\partial_t + \mathbf{u} \cdot \nabla)\mathbf{Q} - \mathbf{S}(\mathbf{W}, \mathbf{Q}) = \Gamma \mathbf{H} \tag{2.2}$$

where $\mathbf{u}$ is the velocity vector and Γ is related to the rotational viscosity γ_1 via $\Gamma = 2S^2/\gamma_1$ Here, the generalized advection term $\mathbf{S}(\mathbf{W}, \mathbf{Q})$ is defined as

$$\begin{aligned} \mathbf{S}(\mathbf{W}, \mathbf{Q}) = &(\xi \mathbf{A} + \blacksquare)(\mathbf{Q} + \mathbf{I}/3) \\ &+ (\mathbf{Q} + \mathbf{I}/3)(\xi \mathbf{A} - \blacksquare) \\ &- 2\xi(\mathbf{Q} + \mathbf{I}/3))\,\mathrm{Tr}(\mathbf{QA})) \end{aligned} \tag{2.3}$$

with $\mathbf{A} = (\nabla \mathbf{u} + (\nabla \mathbf{u})^T)/2$ being the strain rate tensor, $\blacksquare = (\nabla \mathbf{u} - (\nabla \mathbf{u})^T)/2$ being the vorticity, and ξ being a flow-alignment parameter setting the Leslie angle. The molecular field $\mathbf{H}$ is a symmetric, traceless projection of the functional derivative of the free energy of the nematic. Its index form reads

$$H_{ij} = \frac{1}{2}\left(\frac{\delta F}{\delta Q_{ij}} + \frac{\delta F}{\delta Q_{ji}}\right) - \frac{\delta_{ij}}{3}\,\mathrm{Tr}\left(\frac{\delta F}{\delta Q_{ij}}\right) \tag{2.4}$$

in which the free energy functional is $F = \int_V f dV$. Its density f takes the following form:

$$\begin{aligned} f = &\frac{A_0}{2}\left(1 - \frac{U}{3}\right) Q_{ij}Q_{ij} - \frac{A_0 U}{3} Q_{ij}Q_{jk}Q_{ki} \\ &+ \frac{A_0 U}{4} Tr(Q_{ij}Q_{ij})^2 + \frac{1}{2} L \partial_k Q_{ij} \partial_k Q_{ij} \end{aligned} \tag{2.5}$$

where A_0, U are material constants and L is related to the Frank elastic constant under the one-constant-approximation. Eq.2.2 is solved using a finite difference method.

The hydrodynamic flow is governed by a momentum equation:

$$\begin{aligned} &\rho(\partial_t + u_j \partial_j) u_i = \partial_j \Pi_{ij} \\ &+ \eta \partial_j \left[\partial_i u_j + \partial_j u_i + (1 - 3\partial_\rho P_0)\partial_\gamma u_\gamma \delta_{ij}\right] \end{aligned} \tag{2.6}$$

where ρ is density, η is the isotropic viscosity, and $P_0 = \rho T - f$ is the hydrostatic pressure with T being the temperature. The additional stress has two contributions, $\Pi_{ij} = \Pi^p_{ij} + \Pi^a_{ij}$, where the first term is passive in its nature accounting for the anisotropy, and is defined as

$$\begin{aligned} \Pi^p_{ij} = &- P_0 \delta_{ij} - \xi H_{ik}\left(Q_{kj} + \frac{1}{3}\delta_{kj}\right) \\ &- \xi\left(Q_{ik} + \frac{1}{3}\delta_{ik}\right) H_{kj} \\ &+ 2\xi\left(Q_{ij} + \frac{1}{3}\delta_{ij}\right) Q_{kl} H_{kl} \\ &- \partial_j Q_{kl} \frac{\delta F}{\delta \partial_i Q_{kl}} + Q_{ik} Hkj - H_{ik} Q_{kj} \end{aligned} \tag{2.7}$$

The active stress that drives the system out-of-equilibrium reads

$$\Pi^a_{ij} = -\alpha Q_{ij} \tag{2.8}$$

in which $\alpha > 0$ describes an extensile active nematic, as is the case for the experimental systems discussed in this manuscript. Eq.2.6 is solved simultaneously via a lattice Boltzmann method over a D3Q15 grid Guo et al. [2002a]. Additional details on this method

can be found in Zhang et al. [2016].

CHAPTER 3

CATAPULTING OF TOPOLOGICAL DEFECTS THROUGH ELASTICITY BANDS IN ACTIVE NEMATICS

3.1 Introduction

Active materials are those in which components locally break detailed balance (Ramaswamy [2010], Marchetti et al. [2013]). This local energy injection coupled with both local and global dissipative mechanisms—which depend on the exact material properties—leads to complex dynamical states (Ramaswamy [2010], Needleman and Dogic [2017], Hatwalne et al. [2004], Sokolov and Aranson [2009], Rafaï et al. [2010], Wensink et al. [2012], Nitin Kumar and Sood [2014], Fodor et al. [2016], Solon et al. [2015], Cates and Tailleur [2015], Kumar et al. [2019]). Understanding how the interplay between local force generation and specific material viscoelasticity control the emergent structure and dynamics is an outstanding challenge in active matter. Generalized hydrodynamic approaches have proven successful in understanding active fluids at large length and time scales (Marchetti et al. [2013], Joanny and Prost [2009]). However, the peculiarities of specific systems can lead to exotic dynamical states at more immediate scales.

Due to their intrinsic and tunable elasticity, nematic liquid crystals (LC) are an ideal system to answer questions about the interplay of elastic dissipation and active driving (Gennes and Prost [1993]). Formed from dense packings of rod-like constituents, LCs elastically resist distortions to their mesoscopic order while remaining locally fluid like. When an extensile (contractile) active stress outcompetes this nematic restoring force, the material is rendered bend (splay) unstable and can be deformed. Sufficient deformation of this kind results in the nucleation of $\pm$ 1/2 topological defect pairs (Aditi Simha and Ramaswamy [2002], Giomi et al. [2014], Thampi et al. [2013a], DeCamp et al. [2015]). Once defects are created, LCs driven by extensile (contractile) stresses results in the propulsion

of comet-like +1/2 defects along (against) their orientation. At sufficiently high activity level, an “active turbulent” state develops. In this regime, topological defects constantly form, move, and annihilate creating complex hydrodynamic flows (Narayan et al. [2007], Kumar et al. [2018], Thampi et al. [2014a]). In well developed turbulence, the dynamical properties of the active nematic are well described by hydrodynamic models (Giomi [2013], Giomi et al. [2014], Zhang and Pablo [2016], Thampi et al. [2014b]). These models show that when elastic force is much less than the active force, hydrodynamic effects dominate the dynamics. At lower activity levels, however, one expects elasticity to play an greater role in the dynamics and for emergent structural patterns to potentially deviate from those predicted in the hydrodynamic limit. Indeed, one example of such a structure is found in transient, elongated bend deformations which have been observed at low activity levels in numerical and experimental systems generally preceding from globally aligned initial states (Zhou et al. [2014], Martínez-Prat et al. [2019], Sokolov et al. [2019b], Patelli et al. [2019], Chandrakar et al. [2020], Senoussi et al. [2019], Nejad et al. [2021]).

Here we explore structure and dynamics in active nematics where active and elastic stresses are similar in magnitude. We exploit a highly tunable biomolecular nematic LC that is comprised of the biopolymer F-actin and driven by the molecular motor myosin II (Kumar et al. [2018]). In this system, modulation of nematic elasticity can be achieved either through control over F-actin length, l, or by the addition of small quantities of microtubule biopolymers, which are 100-fold stiffer than F-actin (Zhang et al. [2017]). Further, time-dependent variation in myosin II concentration facilitates exploration of nematic structure and dynamics over a large range of activities. Recently, we showed that, for high activity, this system is well described by a hydrodynamic model of active nematics (Kumar et al. [2018]). However, for LC with high bend elasticity and at intermediate activity, we observe a dynamical steady state comprised of elongated "bands" of bend deformations. These “elasticity bands” undergo continuous creation and destruc-

tion, with highly variable length and width. The presence and persistence of these structures is highly dependent on nematogen length, indicating an important role of nematic elasticity in their formation. To isolate the contributions of splay and bend elasticity, we perform experiments where we selectively modify bend elasticity and find its increase to be sufficient to control band formation. Measuring the elastic distortion within the nematic as a function activity, we find that bands observed at intermediate activity coincide with a state of maximal elastic distortion. This likely reflects the increased energetic barrier for defect creation in LC with high bend elasticity. This observation is confirmed with hydrodynamic simulations, which also reveal that the elastic distortion of high elasticity LC increases non-monotonically with activity in a history dependent manner. Finally, we show that the elastic distortion stored in bands is relieved by a rapid motion, or "catapulting", of +1/2 defects. Taken together, our results demonstrate a new dynamic steady state in active nematics governed by the interplay of activity and bend elasticity.

3.2 Results

3.2.1 Observation of elasticity bands in F-actin based active nematics

A thin nematic LC was formed by crowding short ($\sim \mu$m) F-actin to a surfactant-stabilized oil-water interface using the depletant methylcellulose and waiting 30-45 minutes (Fig. 1A). The average F-actin length (l) is controlled by varying the concentration of F-actin capping protein (CP) (Palmgren et al. [2001], Weirich et al. [2017]). Our previous work showed that the splay (K_{11}) and bend (K_{33}) elasticity of such a nematic can be varied as $\sim l$ and $\sim l^3$, respectively (Zhang et al. [2017]). Utilizing this tool, we investigate the activity of liquid crystals with three different elasticities: l = 1 μm (K_{11} = 0.26 pN, K_{33} = 0.13 pN), l = 1.5 μm (K_{11} = 0.44 pN, K_{33} = 0.56 pN) and l = 2 μm (K_{11} = 0.52 pN, K_{33} =1.04 pN) (Zhang et al. [2017]). Active stress is introduced to the system by the addition of the

molecular motor myosin-II. Upon their addition, myosin-II motors slide antiparallel actin filaments past each other resulting in net extensile stresses in the LC. This activity results in the spontaneous creation of topological defect pairs and emergent complex flows with a typical active state shown in Fig. 3.1B. The optical contrast in these panels arises from the polarized excitation laser stimulating fluorophores that label the length of the actin filament (Kinosita et al. [1991], Sase et al. [1997]). Thus, this optical contrast provides a direct readout of the local nematic director field up to a symmetry factor (Zhang et al. [2021]). The bright and dark regions of the image correspond to actin filaments aligned in the vertical and horizontal directions, respectively (see colorbar in Fig. 3.1B). From these images, the local nematic director field is determined (Kumar et al. [2018]), and indicated by the blue lines. The local nematic director field is utilized to identify important features such as $\pm$ 1/2 topological defects, points of vanishing nematic order, in the LC. Such a defect pair is shown in Fig. 3.1B with a schematic of their shapes.

In addition to point-like topological defects we notice–in certain cases–extended two dimensional structures that we term "elasticity bands". Elasticity bands, or simply bands, are extended regions between a pair of defects that are perpendicular to the surrounding director field. An example of an elasticity band in a nematic with K_{11} = 0.26 pN and K_{33} = 0.13 pN is outlined by black solid lines in Fig. 3.1B. To understand the structure of these interesting features we measure the director field orientation across a line segment locally perpendicular to the band with coordinate d. A plot of the director field angle θ as a function of d is shown in Fig. 3.1F and reveals a region where θ varies linearly as a function of d flanked by regions of constant θ. We then can define the width as the distance over which theta varies linearly. One can also measure the length of a band as the distance between the flanking defects. When we do so for nematics of varying elasticity we notice that higher elasticity LCs sport bands of dramatically increased length as seen in Fig. 3.1C. The band length, l_{band}, and defect spacing, l_{defect}, for nematics at low

and high elasticity are shown in Fig. 3.1D. For nematics with shorter filaments and thus lower elasticity, the band length is similar to the mean defect spacing. By contrast, in high elasticity nematics, the bands can be much longer than the mean defect spacing and become more prominent features. While variable elasticity clearly changes the structures present we also quantified the differences in these active nematics by measuring their elastic energy distributions, $E_{splay} = |(\boldsymbol{\nabla} \cdot \mathbf{n})|^2 da$ and $E_{bend} = |(\boldsymbol{\nabla} \times \mathbf{n})|^2 da$, for splay and bend respectively. Fig 3.1E shows the probability distribution function (PDF) of local splay and bend distortions in the nematic. For the low elasticity nematic (K_{11} = 0.26 pN, K_{33} = 0.13 pN), the PDFs of the splay and bend energies both decay as power law with an exponent $n \simeq 1.7$, consistent with hydrodynamic simulations for active nematics. For the higher elasticity nematic (K_{11} = 0.52 pN, K_{33} = 1.04 pN), the PDFs for both splay and bend distortions deviate significantly from the power law at high energies indicating that this high elasticity nematic is more likely to store energy structurally than its low elasticity cousin.

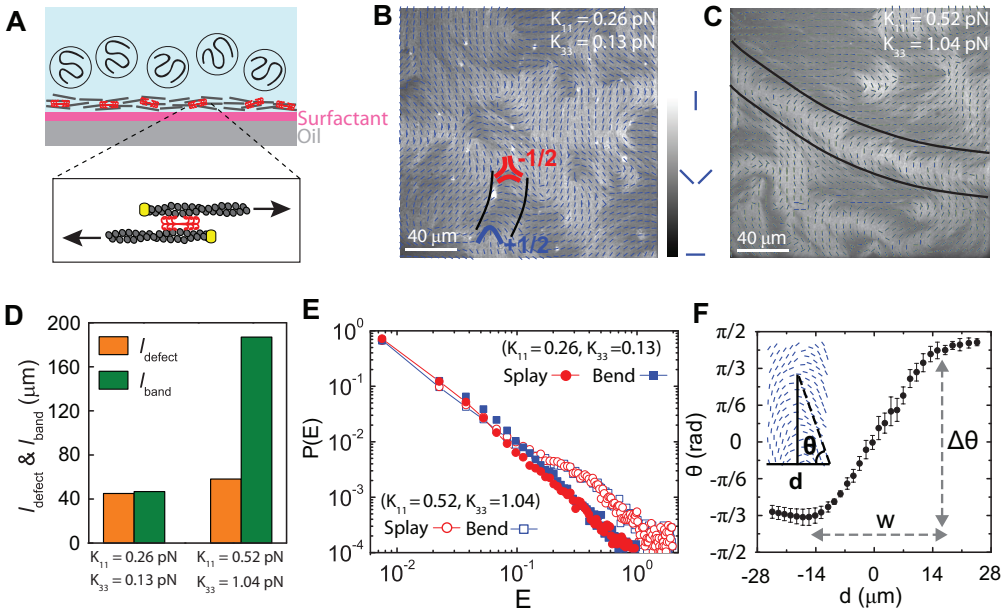

Figure 3.1: **Observation and Characterization of elasticity bands in active nematics** A) Schematic representation of the experiment showing F-actin (grey) crowded to an oil-water interface using methylcellulose (circles). Inset shows myosin II motors (red) translocating short F-actin, with capping protein (yellow) indicating the F-actin barbed end. B-C) Images of fluorescent F-actin in LC of low elasticity (K_{11} = 0.26 pN, K_{33} = 0.13 pN) (B) and high elasticity LC (K_{11} = 0.52 pN, K_{33} = 1.04 pN) (C). The local director field superposed with the colorbar showing how the intensity variations map to the local nematic field. A pair of $\pm 1/2$ defects are separated by a region of bend deformation (band) outlined by solid black lines. D) Maximum band length (l_{band}) and mean defect spacing (l_{defect}) for the two nematics shown above. E) Probability distribution of the bend and splay elastic distortion for the two nematics described above. The higher elasticity nematic, plotted with open symbols, exhibits a heavy tail corresponding to bands. F) The variation of the director field across an elastic band as shown in the inset. The band width, w, is determined by distance over which the director field orientation θ changes linearly.

3.2.2 *Bands form topologically neutral branches*

In addition to the increased band length, we also observe an increase in their structural complexity. Previous observations of similar structures have noted not only the simple structures such as the schematic shown in Fig. 3.2A but also branching phenomena such as that shown in Fig. 3.2B (Sokolov et al. [2019b]). These schematics of topologically neutral structures indicates how a stable branch might be formed. In its simplest form

a band is anchored on either side by a $\pm$ 1/2 defect pair. Thus even though the length of the band is perpendicular to the surrounding director field, the structure as a whole is topologically neutral. The schematic in Fig. 3.2B demonstrates that if a band were to branch, the three free ends would all be anchored by defects as one might expect, but to maintain local topological neutrality a fourth defect that is not "attached" to the band must nonetheless be associated with the structure and oppose the branch point.

Such a prediction bears out when we observe the branching of a band in experiment. Fig. 3.2C shows a series of experimental snapshots where an initial band, anchored on one side by a +1/2 defect, branches towards the -1/2 defect initially visible on the left hand side of the image. This branching proceeds from an initially aligned region (purple line) which appears to buckle as the movie proceeds, steadily reducing in width. A similar pattern of region buckling and band width reduction can be seen in hydrodynamic simulations shown in Fig. 3.2D where the color underneath the director field is a measure of nematic order with a darker color indicating less ordered regions. In this series of simulation snapshots we can see, just as in the experiment, an initially aligned region begin to buckle and the resultant band reduce in width over time. In both experiment and simulation, the final mature branched structures exhibit +1/2 defects pointed "towards" the branch point as in the schematic in Fig. 3.2B. Having examined the geometry of a band we now ask how the mechanics of the LC might contribute to their formation.

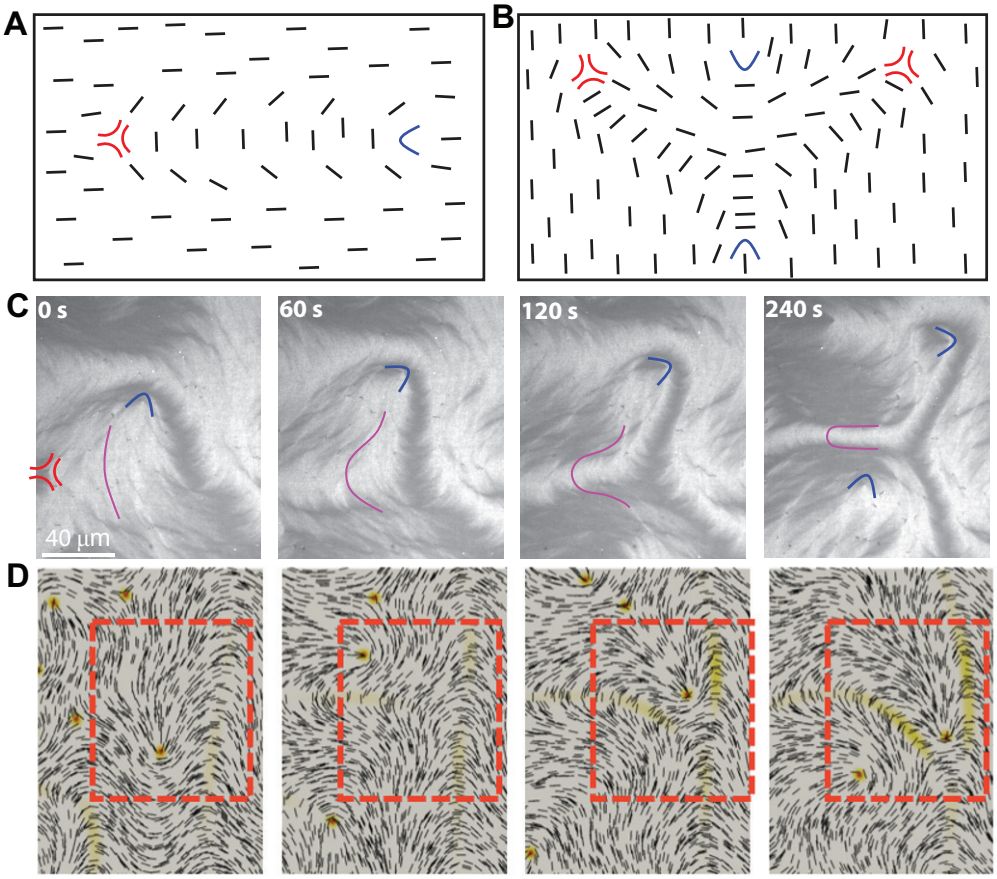

Figure 3.2: **Formation and structure of branched bands** A) Schematic of topologically neutral structure containing a simple band. B) Schematic of a topologically neutral structure of a branched band. Note how the +1/2 defect that is not attached to the band opposes the branch point to maintain topological neutrality. C) Time series of experimental snapshots of a branched band forming in a nematic with (K_{11} = 0.52 pN, K_{33} = 1.04 pN). An initially aligned region (purple line) adjacent to an extant band buckles towards a -1/2 defect (red trefoil). As the bend distortion increases, a +1/2 defect appears opposing the branch point similar to the schematic in (B). D) Time series snapshots of a band forming in hydrodynamic simulation. As the local bend distortion (yellow color) in the nascent band increases, a +1/2 defect approaches the branch point, stabilizing the structure.

3.2.3 *Increasing bend modulus leads to band formation*

To isolate the role of bending modulus in the formation of elasticity bands, we build a composite LC, formed by a low elasticity actin nematic (l=1 μm) sparsely doped with microtubules (1:84 molar ratio) and shown in Fig. 3.3A. As previously described, the

inclusion of microtubules, due to their higher bending rigidity, increases K_{33} without influencing K_{11} (Zhang et al. [2017]). Thus, while the undoped nematic had splay and bend moduli of K_{11}=0.26 pN and K_{33}=0.13 pN respectively, the doped sample exhibited K_{11} = 0.26 pN and K_{33} = 1.04 pN. This difference is particularly striking when activity is added. Whereas the undoped sample featured bands only of approximately the length of average defect spacing (Fig. 3.1B), the doped sample sample supported bands that were much longer (Fig. 3.3B). Active nematic dynamics arise from the competition between elasticity and activity. Thus, in order to fully understand the consequences of increased bend rigidity we consider the state of the nematic over a range of activities.

Thus far we have focused only on a narrow range of activities. We now exploit the time-dependent variation in motor concentration to explore how changes in activity impact band formation (Kumar et al. [2018]). We track the magnitude of active flows measured in terms of root mean squared velocity, $v_{rms} = \sqrt{\langle v^2 \rangle}$ where v is the local velocity measured by particle imaging velocimetry (PIV) as a function of time. Since v_{rms} is proportional to active stress, the activity in our system can be conveniently expressed in terms of v_{rms} (Doostmohammadi et al. [2016], Kumar et al. [2018]). To quantify the magnitude of banding in our experiments, we define the band index ϕ as the area occupied by bands in the experimental field of view divided by the total area (see Methods). This index is low for all velocities in the nematic with low bend elasticity (Fig. 3.3C). By contrast, when K_{33} = 1.04 pN the band index is high for low velocities and then drops suddenly to a lower value for $v_{rms} > 0.14$ μm s^{-1}.

To further understand this, we track the amount of bend distortion as a function of v_{rms}. For the low K_{33}, this distortion is minimal for the lowest velocities and, beyond a threshold v_{rms} shows a monotonic increase (Fig. 3.3D). The threshold beyond which distortion increases is the minimal energy needed for new defect creation. For the high K_{33} case, we find that elastic distortion increases even at low v_{rms} and, there exists a range

of activities where the elastic distortion plateaus (Fig. 3.3E). This plateau corresponds with the range of activities at which bands are a long lived phenomenon. At even higher activities, the bend distortion abruptly drops. Here the activity is high enough that defect nucleation dominates the dynamics and any bands that form are short lived. This suggests that, for nematics with high bend elasticity, bands are an energy barrier which the nematic must cross before reaching the well known turbulent regime. This is in contrast to nematics with low bend elasticity where there is a direct transition to turbulence without ever creating long bend deformations. We summarize these results in Fig. 3.3F through a state diagram of K_{33} and v_{rms} which shows that the width of the stable band regime is strongly dependent on the strength of bend elasticity K_{33}. This phase diagram– while not precisely the same–bears notable resemblance to one previously predicted from simulation (Srivastava et al. [2016]). To further explore the stability of bands we turn to hydrodynamic simulations of active nematics.

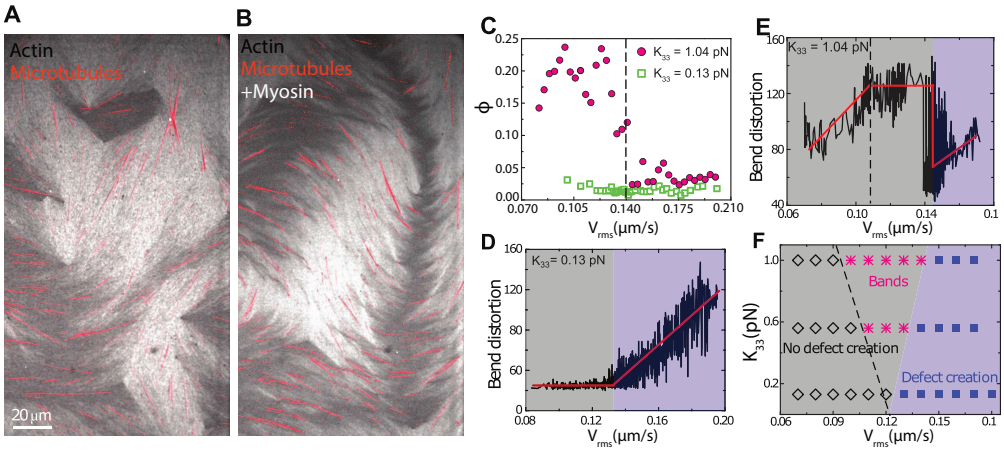

Figure 3.3: **Increased bend elasticity promotes band formation at intermediate activities** A) Optical images of actin LC containing a sparse concentration of microtubules in red with bend modulus K_{33} = 1.04 pN. B) The same nematic as in (A) after the addition of myosin-II. Note the long band reminiscent of Fig. 3.1C. C) Band index (ϕ), defined as the area fraction occupied by bands, plotted as a function of root mean squared velocity, (v_{rms}). While for low K_{33} no significant population of bands is observed, nematics with high elasticity only exhibit large area fractions of bands below a certain critical v_{rms} (black dashed line). D) Bend distortion ($E_{bend} = |(\boldsymbol{\nabla} \times \mathbf{n})|^2 da$) in a high elasticity nematic plotted as a function of v_{rms}. The purple region corresponds to the right hand side of the black line in (C). The black dased line here corresponds to the onset of an energetic plateau. E) Total bend elastic distortion plotted as a function of v_{rms} for K_{33} = 0.13 pN. The purple region beyond 0.12 μm/s indicates the region of defect creation. F) State diagram summarizing the dynamic states observed as a function of K_{33} and v_{rms}. The data points are from three samples K_{11}=0.26 and varying K_{33} over a range of activities and are color coded for regimes with no defect creation (open black diamonds), elastic bands (magenta stars) and defect creation (blue squares). The transition from gray to blue shading indicates a crossover to active stresses sufficient for defect creation.

3.2.4 *Band stability is initial condition dependent*

The model we employ here has proven successful in understanding many of active nematic phenomena in lyotropic systems, including actin, microtubule and living-liquid-crystal systems (Zhang and Pablo [2016], Kumar et al. [2018], Sokolov et al. [2019b]). To understand the stability of elasticity bands and their relationship with defects, we prepare the initial director field in two ways, one random and the other uniform (Fig. 3.4A,B, inset). For a random initial configuration, simulations show that at sufficient high activity

when active turbulence is fully developed, short and transient elasticity bands are seen (Fig. 3.4A). In contrast, at the same activity level, a simulation instantiated with uniform initial conditions exhibits a series of oppositely directed bands that span the simulation box (Fig. 3.4A). To understand the differences between these two cases we plot the system's steady-state elastic energy as a function of time (Fig. 3.4C,D). We find that in simulations stemming from random initial conditions two basic trends hold. First, we observe that the average steady state value of the elastic energy monotonically increases with activity. Similarly, we find that the frequency of fluctuations in elastic energy increases with activity (Fig. 3.4C). These trends can be understood simply in terms of defect dynamics. As activity increases, the average number of defects at steady state increases while the frequency of creation and annihilation events experiences a similar increase. With this in mind, it is notable that in simulations stemming from uniform initial conditions, the average steady state energy is in fact not a monotonic function of activity (Fig. 3.4D). In fact, what we see is that the elastic energy increases with activity to a point (dashed black line) and then decreases. This decrease corresponds to the emergence of fluctuations in the steady state elastic energy and thus the emergence of defects. Previous studies have pointed out that elasticity bands are formed from a uniform director field due to bend-driven hydrodynamic instabilities, and are precursors to the defect state. Interestingly, our results show that the longevity of bands in simulations with uniform initial conditions is a consequence of the symmetry of the initial state and that breaking this symmetry leads to the breakdown of bands at much lower activities. This breakdown of bands is due to their decomposition into and interactions with topological defects which have very interesting consequences for the dynamics of the system.

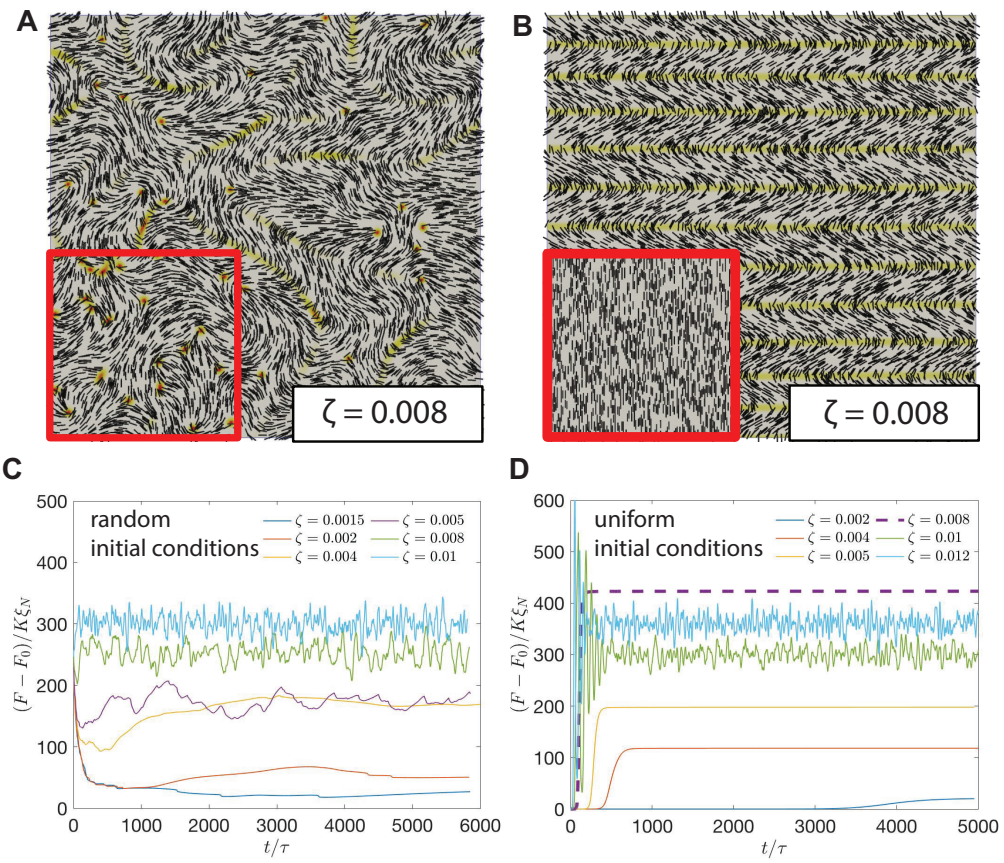

Figure 3.4: **Band stability is a history dependent phenomenon** A) Simulation snapshot of fully developed active turbulence stemming from random initial conditions (inset). With these initial conditions, bands (yellow) are relatively short. B) Simulation snapshot of stable structures formed in a nematic at the same activity level stemming from uniform initial conditions (inset). Note that the bands arising from these initial conditions are a stable series of oppositely directed bands that span the space of the simulation box. C) Steady state elastic energy plotted over time for simulations with random initial conditions across a range of activities. D) Steady state elastic energy for simulations stemming from uniform initial conditions. The dashed purple curve is the highest activity level that does not produce defect pairs and only exhibits stable bands.

3.2.5 *Bands catapult defects through nematics*

Bands are highly dynamic and, much like defects, undergo spontaneous creation and annihilation. While bands are created from a 'buckling' of the director field as in Fig. 3.2C, they are annihilated by the motion of defects. Due to their compatible geometries, a +1/2 defect moving along a band–such as the schematic Fig. 3.2A–will lead to a shortening of

the band. This can be clearly seen in the experimental snapshots in Fig. 3.5A where a +1/2 defect moves along a band leaving an aligned director field in its wake. Band shortening in this manner can also proceed after a severing event. As bands mature, they thin to a width set by the competition between activity and elasticity. If bands become sufficiently thin, they can sever via the formation of a $\pm$ 1/2 defect pair as seen in Fig. 3.5B. These nascent defect pairs move quickly through the band leading to rapid annihilation after nucleation. To understand this phenomenon, we plot the probability density of +1/2 defect speeds in the nematic. We find that while most defects are distributed gaussianly around a single speed, a small population move significantly faster resulting in a bimodal distribution of defect speeds, Fig. 3.5C. This anomalous defect speed is the result of the release of stored elastic energy from the band in the form of defect motion. To see this point concretely we plot the speed of defects moving through bands as a function of band strength, $\Delta\theta/w$, as defined in Fig. 3.1F, in Fig. 3.5D. The data from experiments with myosin-II can be seen in blue and clearly show that thinner bands result in faster defect propulsion. To ensure that such an effect is indeed due to the bands themselves and is not in fact a product of motor driven activity, we perform experiments with a synthetic myosin-VI motor (Schindler et al. [2014]). We find that band-associated defects in this system follow the same trend as in the myosin-II nematic. This indicates that the catapulting of defects through bands is indeed a product of stored bend elasticity in the material and not the specifics of motor propulsion. In this manner, the presence of bands in the nematic system leads to a novel dynamical steady state where defects are propelled not only by molecular motors but also by stored elastic energy.

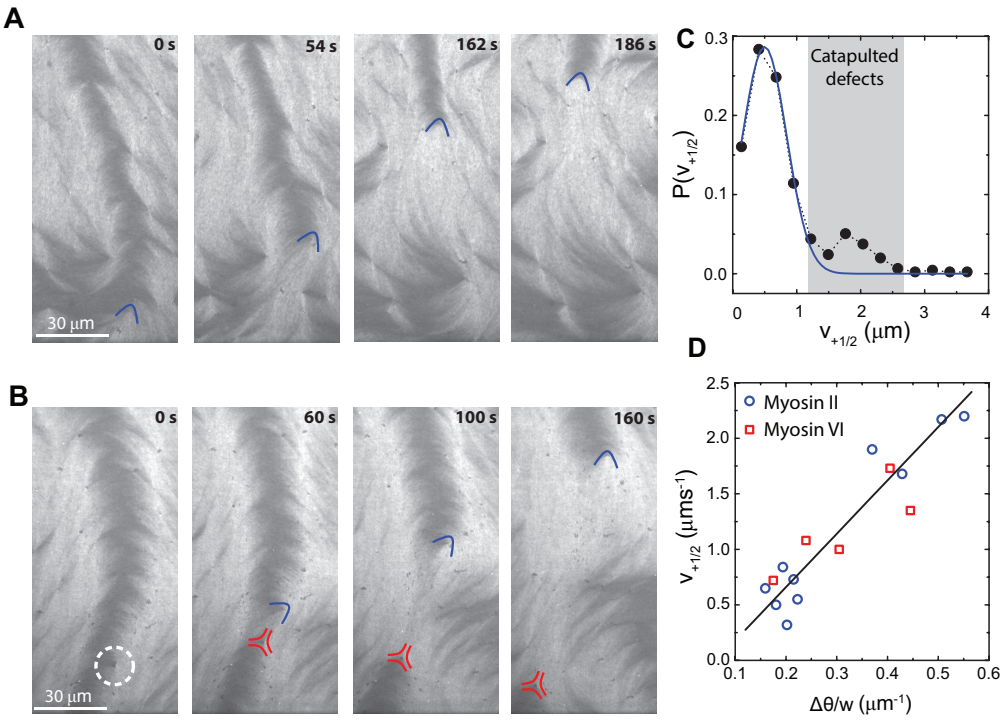

Figure 3.5: **'Catapulting' of +1/2 defects through elasticity bands** A)Time-series of fluorescent images of actin LC (K_{11} = 0.52 pN, K_{33} = 1.04 pN) showing a +1/2 defect (blue chevron) moving along a band leaving a uniformly aligned region in its wake. B) Time series of images showing a band severing event. The band separates near its thinnest point into a $\pm$ 1/2 defect pair after which dynamics proceed as in (A). C) Distribution of speeds of +1/2 defects in the movies from which A & B originated. The blue line coreresponds to a Gaussian fit of the data (black circles). The second peak (outlined in gray) deviates significantly from this single Gaussian fit and corresponds to defects we term 'catapulted'. D) The speed of +1/2 defects within bands tracked over multiple experiments. Defect speed scales inversely with the band strength defined in Fig. 3.1F. The data includes actin LCs driven by both myosin-II (red squares) as well as synthetic myosin-VI motors (blue circles). The solid line is the fit to the analytical model.

3.3 Conclusions

Here we explored the effect of nematic bend elasticity on emergent flows in active nematics. By utilizing experimental control over specifically bend elasticity, we found a novel dynamical phase where defects and elongated elasticity bands coexist and interact to alter the nature of complex flows. We described the structure of these bands in terms of

their width and the change in director angle from one side to the other. Furthermore, we saw that bands can exist not only in their simplest linear form but also in higher order branched structures. We showed that increases in the bend elastic modulus are sufficient to control band formation. This further strengthens previous findings that disparate elastic constants (i.e. $K_{11} \neq K_{33}$) not only play an important role in determining the shape of topological defects (Zhang et al. [2017]) and defect density (Kumar et al. [2018]), but also in predicting the dynamics of complex active flows.

Previous work has suggested that active nematics are endowed with a characteristic length scale which depends on the ratio of elasticity to activity given by K and α respectively. In this framework, an increased K corresponds to a higher energy barrier required to undergo defect formation. While our system does not map perfectly onto this description due to disparate elastic constants, we nonetheless see similar phenomena with bands. Bands are less prevalent at high activities and low bend elasticities. Furthermore, at intermediate activity and high bend elasticity, a state occurs in which bands are long lived, corresponding to the increased barrier for defect creation at these high elasticity values. When the activity is increased further however we find a state that is dominated by defects, akin to the active turbulence described previously.

Bands are not a stranger in the active nematic literature, however discrepancies have existed between the long lived structures described in simulations at low activity (Fig.3.4D) and the transient structures in experiments (Fig.3.5B). Here we showed that this discrepancy can be explained by initial conditions. We found that simulations started from uniform initial conditions supported long lived bands over a very large range of activities and resulted in a decrease in stored elastic energy upon their disintegration. Meanwhile, simulations that proceeded from random initial conditions showed monotonic energy scaling and shorter lived bands. This further underlines how bands are not merely a structural quirk but an important player in the LC dynamics.

When bands are present in a system with intermediate activity, they play a central role in the dynamics. For one, bands dictate the path of +1/2 defects in the system as they 'zips' up bands, leaving a uniformly aligned director field in their wake. Furthermore, a band itself can not only nucleate a defect pair but also convert stored bend elastic energy into motion in the form of catapulting defects. The combination of these effects leads to an exotic dynamical state when bend elasticity is about equal in strength to extensile activity.

Overall then, bands are an example of a situation in which the interplay of nematic elasticity and activity produces a novel dynamical state. While the state described in this work is due to the competition between specifically bend elasticity and extensile stress, one could imagine that different combinations of stress modalities and specific elasticities might result in many interesting states.

3.4 Methods

3.4.1 Experimental methods

Proteins

We purify monomeric actin purified from rabbit skeletal muscle acetone powder purchased from Pel-Freez Biologicals, Rogers, AR) Spudich and Watt [1971] and stored at -80^0C in G-buffer containing 2mM Tris HCL pH 8.0, 0.2 mM APT, 0.2 mM $CaCl_2$, 0.2 mM DTT, 0.005% NaN_3). For fluorescence microscopy, we label G-actin with Tetramethylrhodamine — 6 — maleimide dye (Life Technologies, Carlsbad, CA). Capping protein (with a His-tag) is used to regulate actin filament length purified from bacteria (plasmid gifted by Dave Kovar lab, The University of Chicago) Palmgren et al. [2001]. Mictotubules are polymerized in PEM-100 buffer at 37° C (100mM Na-PIPES, 1mM $MgSO_4$, 1mM EGTA, pH 6.8) in the 1:10 ratio of fluorescently labeled tubulin (Cytoskeleton, cat# TL488M) and

unlabeled tubulin (Cytoskeleton, cat# HTS03) in the presence of 1 mM GMPCPP (Jena Biosciences, cat # NU-405L). They are later stabalized by adding 50 μM Taxol. The microtubule length is shortened by shearing through Hamilton Syringe (Mfr # 81030, Item # EW-07939-13). Skeletal muscle myosin II is purified from chicken breast Margossian and Lowey [1982] and labeled with Alexa-642 maleimide (Life Technologies, Carlsbad, CA) Murrell and Gardel [2012]. Synthetic myosin-VI motors were purified from the construct $M6DI_{816}2R_TET$ from Schindler et al. [2014] and were a gift from the lab of Zev Bryant.

Experimental assay and microscopy

Actin from frozen stocks stored in G-buffer is added to a final concentration of 2 μM with a ratio 1:5 TMR-maleimide labeled:unlabeled actin monomer. We polymerize actin in 1X F-buffer (10 mM imidazole, pH 7.5, 50mM KCL, 0.2mM EGTA, 1mM $MgCl_2$ and 1mM ATP). To minimize photobleaching, an oxygen scavenging system (4.5 mg/mL glucose, 2.7 mg/mL glucose oxidase(cat#345486, Calbiochem, Billerica, MA), 17000 units/mL catalase (cat #02071, Sigma, St. Louis, MO) and 0.5 vol. % β-mercaptaethanol is added. We use 0.3 wt % 15 cP methylcellulose as the crowding agent for actin filaments. Frozen capping protein stocks are thawed on ice and are added at the same time (6.7 and 3.3 nM for 1 μm and 2 μm long actin filaments respectively). Myosin-II is mixed with phalloidin-stabilized F-actin at a 1:4 myosin/actin molar ratio in spin-down buffer and centrifuged for 30 min at 100,000 × g. The supernatant containing myosin with low affinity to F-actin is used in experiments whereas the high-affinity myosin is discarded. For experiments with microtubules, taxol-stabilized microtubules are added to the final concentration of 1 μg/mL, a 1:84 ratio of microtubules to actin.

We use a glass cylinder (cat# 09-552-22, Corning Inc.) glued to a coverslip as an experimental sample same as Kumar et al. [2018]. Coverslips are cleaned by sonicating in water and ethanol. To create a hydrophobic surface, they are further treated with tri-

ethoxy(octyl)silane in isopropanol. For creating an oil-water interface, PFPE-PEG-PFPE surfactant (cat # 008, RAN biotechnologies, Beverly, MA) is dissolved in Novec-7500 Engineered Fluid (3M, St Paul, MN) to a concentration of 2% wt/volume. To prevent bulk flows at the surface, a small 2×2 mm teflon mask is placed on the treated coverslip before exposing it to UV/ozone for 10 minutes. A glass cylinder thouroughly cleaned with water and ethanol and is glued to the coverslip using instant epoxy. 3 μL of oil-surfactant solution is added into the chamber, and quickly pipetted out (3 s) to leave a thin oil coating. The polymerization mixture is immediately added afterwards. $30-60$ minutes later, a thin layer of actin LC is formed. The sample is always imaged in the middle of the film over the camera field of view, which is approximately 200 μm $\times$ 250 μm to make sure that the sample remains in focus over this area, which is far away from the edges. Myosin II **or tetrameric myosin** motors are added to the polymerization mixture at $5-10$ nM and 200 pM respectively.

The sample is imaged using an inverted microscope (Eclipse Ti-E; Nikon, Melville, NY) with a spinning disk confocal head (CSU-X, Yokagawa Electric, Musashino, Tokyo, Japan), equipped with a CMOS camera (Zyla-4.2 USB 3; Andor, Belfast, UK). A 40X 1.15 NA water-immersion objective (Apo LWD; Nikon) was used for imaging. Images were collected using 491 nm, 568 nm and 642 nm excitation for microtubules, actin, and myosin-II respectively. Image acquisition was controlled by Metamorph (Molecular Devices, Sunnyvale, CA).

PIV and root-mean-squared velocity

The active flows are quantified using particle image velocimetry (available at `www.oceanwave.jp/softwares/mpiv/`) to extract local velocity field, $\mathbf{v}$. The images were processed through unsharped masking and then background subtraction using built-in plugins in ImageJ software Rasband [1997]. The grid size of 2.4 μm was used for PIV vector calcula-

tion and images were separated by a time-interval of 5 s.

Band Characterization and Band Index

To identify bands in fluorescent images, we perform a series of image processing algorithms in ImageJ software. We first enhance the contrast of our images using the CLAHE plugin. Later we use "shape index map" plugin to separate the bands which are later outlined using "edge detection" plugin. This image is then thresholded which marks the band outlines and separate them from the rest of the image. Using this, we then calculate the area inside the bands and divide it by the total area to calculate ϕ.

3.4.2 Numerical methods

Continuum Model

The total free energy of the nematic LC, F, consists of a bulk and a surface term:

$$\begin{aligned} F &= \int_V dV f_{bulk} + \int_{\partial V} dS f_{surf} \\ &= \int_V dV (f_{LdG} + f_{el}) + \int_{\partial V} dS f_{surf}, \end{aligned} \tag{3.1}$$

where f_{LdG} is the short-range free energy, f_{el} is the long-range elastic energy, and f_{surf} is the surface free energy associated with preferred nematic orientation. f_{LdG} is the Landau-de Gennes in the Doi formGennes and Prost [1993]:

$$f_{LdG} = \frac{A_0}{2}(1 - \frac{U}{3}) \operatorname{tr}\left(\mathbf{Q}^2\right) - \frac{A_0 U}{3} \operatorname{tr}\left(\mathbf{Q}^3\right) + \frac{A_0 U}{4} (\operatorname{tr}\left(\mathbf{Q}^2\right))^2. \tag{3.2}$$

Parameter U controls the magnitude of q_0, namely the equilibrium scalar order parameter via $q_0 = \frac{1}{4} + \frac{3}{4}\sqrt{1 - \frac{8}{3U}}$. The elastic energy f_{el} is written as ($Q_{ij,k}$ means $\partial_k Q_{ij}$):

$$\begin{aligned} f_{el} =& \frac{1}{2}L_1 Q_{ij,k}Q_{ij,k} + \frac{1}{2}L_2 Q_{jk,k}Q_{jl,l} \\ &+ \frac{1}{2}L_3 Q_{ij}Q_{kl,i}Q_{kl,j} + \frac{1}{2}L_4 Q_{ik,l}Q_{jl,k}. \end{aligned} \tag{3.3}$$

If the system is uniaxial, the above equation is equivalent to the Frank Oseen elastic energy expression:

$$\begin{aligned} f_e = &\frac{1}{2}K_{11}(\nabla \cdot \mathbf{n})^2 + \frac{1}{2}K_{22}(\mathbf{n} \cdot \nabla \times \mathbf{n})^2 + \frac{1}{2}K_{33}(\mathbf{n} \times (\nabla \times \mathbf{n}))^2 \\ &- \frac{1}{2}K_{24}\nabla \cdot [\mathbf{n}(\nabla \cdot \mathbf{n}) + \mathbf{n} \times (\nabla \times \mathbf{n})]. \end{aligned} \tag{3.4}$$

The L's in Eq. 3.3 can then be mapped to the K's in Eq. 3.4 via

$$\begin{aligned} L_1 &= \frac{1}{2q_0^2}\left[K_{22} + \frac{1}{3}(K_{33} - K_{11})\right], \\ L_2 &= \frac{1}{q_0^2}(K_{11} - K_{24}), \\ L_3 &= \frac{1}{2q_0^3}(K_{33} - K_{11}), \\ L_4 &= \frac{1}{q_0^2}(K_{24} - K_{22}). \end{aligned} \tag{3.5}$$

Point wise, $\mathbf{n}$ is the eigenvector associated with the greatest eigenvalue of the $\mathbf{Q}$-tensor at each lattice point.

To simulate active LC's dynamics, a hybrid lattice Boltzmann method is used to simultaneously solve a Beris-Edwards equation and a momentum equation which accounts for the hydrodynamic flows. By introducing a velocity gradient $W_{ij} = \partial_j u_i$, strain rate

$\mathbf{A} = (\mathbf{W} + \mathbf{W^T})/\mathbf{2}$, vorticity $\blacksquare = (\mathbf{W} - \mathbf{W^T})/\mathbf{2}$, and a generalized advection term

$$\begin{aligned}\mathbf{S}(\mathbf{W},\mathbf{Q}) =&(\xi\mathbf{A} + \blacksquare)(\mathbf{Q} + \mathbf{I}/3) + (\mathbf{Q} + \mathbf{I}/3)(\xi\mathbf{A} - \blacksquare) \\ &- 2\xi(\mathbf{Q} + \mathbf{I}/3)\,\mathrm{tr}(\mathbf{QW}),\end{aligned} \tag{3.6}$$

one can write the Beris-Edwards equationBeris and Edwards [1994] according to

$$(\partial_t + \mathbf{u}\cdot\nabla)\mathbf{Q} - \mathbf{S}(\mathbf{W},\mathbf{Q}) = \Gamma\mathbf{H}. \tag{3.7}$$

The constant ξ is related to the material's aspect ratio, and Γ is related to the rotational viscosity γ_1 of the system by $\Gamma = 2q_0^2/\gamma_1$Denniston et al. [2001b]. The molecular field $\mathbf{H}$, which drives the system towards thermodynamic equilibrium, is given by

$$\mathbf{H} = -\left[\frac{\delta F}{\delta \mathbf{Q}}\right]^{st}, \tag{3.8}$$

where $[...]^{st}$ is a symmetric and traceless operator. When velocity is absent, i.e. $\mathbf{u}(\mathbf{r}) \equiv 0$, Besris-Edwards equation Eq. 3.7 reduce to Ginzburg-Landau equation:

$$\partial_t \mathbf{Q} = \Gamma\mathbf{H}.$$

To calculate the static structures of $\pm 1/2$ defects, we adopt the above equation to solve for the $\mathbf{Q}$-tensor at equilibrium.

Degenerate planar anchoring is implemented through a Fournier-Galatola expressionFournier and Galatola [2005] that penalizes out-of-plane distortions of the $\mathbf{Q}$ tensor. The associated free energy expression is given by

$$f_{surf} = W(\tilde{\mathbf{Q}} - \tilde{\mathbf{Q}}^{\perp})^2, \tag{3.9}$$

where $\tilde{\mathbf{Q}} = \mathbf{Q} + (\mathbf{q_0}/\mathbf{3})\mathbf{I}$ and $\tilde{\mathbf{Q}}^{\perp} = \mathbf{P}\tilde{\mathbf{Q}}\mathbf{P}$. The evolution of the surface $\mathbf{Q}$-field is governed byZhang et al. [2016]:

$$\frac{\partial \mathbf{Q}}{\partial t} = -\Gamma_s \left(-L\nu \cdot \nabla \mathbf{Q} + \left[\frac{\partial f_{surf}}{\partial \mathbf{Q}} \right]^{st} \right), \tag{3.10}$$

where $\Gamma_s = \Gamma/\xi_N$ with $\xi_N = \sqrt{L_1/A_0}$, namely nematic coherence length.

Using an Einstein summation rule, the momentum equation for the nematics can be written asDenniston et al. [2001a, 2004a]

$$\rho(\partial_t + u_j\partial_j)u_i = \partial_j \Pi_{i_j} + \eta\partial_j[\partial_i u_j + \partial_j u_i + (1 - 3\partial_\rho P_0)\partial_\gamma u_\gamma \delta_{i_j}]. \tag{3.11}$$

The stress

$$\Pi = \Pi^p + \Pi^a$$

consists of a passive and an active part. The passive stress Π^p is defined as

$$\begin{aligned} \Pi^p_{ij} = &- P_0\delta_{ij} - \xi H_{i\gamma}(Q_{\gamma j} + \frac{1}{3}\delta_{\gamma j}) - \xi(Q_{i\gamma} + \frac{1}{3}\delta_{\gamma j})H_{\gamma j} \\ &+ 2\xi(Q_{ij} + \frac{1}{3}\delta_{ij})Q_{\gamma\epsilon}H_{\gamma\epsilon} - \partial_j Q_{\gamma\epsilon}\frac{\delta \mathcal{F}}{\delta \partial_i Q_{\gamma\epsilon}} \\ &+ Q_{i\gamma}H_{\gamma j} - H_{i\gamma}Q_{\gamma j}, \end{aligned} \tag{3.12}$$

where η is the isotropic viscosity, and the hydrostatic pressure P_0 is given byFukuda et al. [2005]

$$P_0 = \rho T - f_{bulk}. \tag{3.13}$$

The temperature T is related to the speed of sound c_s by $T = c_s^2$. The active stress readsMarenduzzo et al. [2007b]

$$\Pi^a_{ij} = -\alpha Q_{ij}, \tag{3.14}$$

in which α is the activity in the simulation. The stress becomes extensile when $\alpha > 0$ and contractile when $\alpha < 0$.

Numerical Details

We solve the evolution equation Eq. 3.7 using a finite-difference method. The momentum equation Eq. 3.11 is solved simultaneously via a lattice Boltzmann method over a D3Q15 gridGuo and Shu [2013]. The implementation of stress follows the approach proposed by Guo *et al.*Guo et al. [2002a]. The units are chosen as follows: the unit length a is chosen to be $a = \xi_N = 1\ \mu m$, characteristic of the filament length, the characteristic viscosity is set to γ_1=0.1 Pa·s, and the force scale is made to be $F_0 = 10^{-11}$ N. Other parameters are chosen to be $A_0 = 0.1$, $K = 0.1$, $\xi = 0.8$, $\Gamma = 0.13$, $\eta = 0.33$, and $U = 3.5$ leading to $q_0 \approx 0.62$. The simulation is performed in a rectangular box. The boundary conditions in the xy plane are periodic with size $[N_x, N_y] = [250,\ 250]$. Two confining walls are introduced in the z dimension, with strong degenerate planar anchoring, ensuring a quasi 2D system with z-dimension $N_z = 9$. We refer the reader to Ref. Zhang et al. [2016] for additional details on the numerical methods employed here.

3.4.3 Estimate Viscosity

To understand defect's high velocity in the elastic band, we build on elasticity theory at over-dumped limit. Say an elastic band has width b and depth t (thickness of the 2D film). Given the one-elastic-constant K, the elastic force that drives the defect motion can be written as

$$F_e = \frac{1}{2} K \pi^2 t / b.$$

The viscous drag force is written asKleman and Lavrentovich [2007]

$$F_d = \pi\gamma_1 k^2 v \ln(3.6/Er)t,$$

where $\gamma 1$ is the rotational viscosity, k is the topological charge of the defect, v is the defect velocity, and $Er = \gamma_1 v r_c/K$ is the defect core's Ericksen number with r_c the core radius. At steady state, the above two forces are equal. We find a rigorous formulus for the defect velocity:

$$v = \frac{2\pi K}{\gamma_1 b \ln\left(\frac{3.6}{Er}\right)}.$$

At low Ericksen number or low defect velocity when $Er \ll 3.6$, one has $v \propto 1/b$. To extract rotational viscosity of the nematic in the experiment, we fit the measured data with the above equation with two fitting parameters γ_1 and K.

CHAPTER 4

RESPONSE FUNCTION OF ACTIVE MATERIALS

4.1 Introduction

Active systems can be found at various scales across the natural world. From flocks of birds and schools of fish (Cavagna and Giardina [2014], Marchetti et al. [2013]), to swarms of bacteria (Dombrowski et al. [2004], Wensink et al. [2012]) and the protein filaments inside of cells (Needleman and Dogic [2017]), a system is considered active if individual agents– birds or molecular motors– locally convert energy into mechanical work (Ramaswamy [2010]). These small local injections of energy combine in complex ways to produce long range flows and striking non-equilibrium patterns (Giomi [2015], Gao et al. [2015]). While all active systems share an underlying character, the flow patterns and scaling behaviors exhibited by each is a consequence of their specific mechanisms of energy injection, long range structural interactions, hydrodynamic milieu, and boundary conditions (Marchetti et al. [2013]). Understanding the interactions between these factors and how they lead to the emergent phenomena we observe is an important challenge not just for understanding complex natural systems but also for designing novel and potentially autonomous materials. At the heart of active systems are multiple important length and time scales within the dynamics. These scales and the spectral properties thereof help us to characterize and compare various active systems that are often turbulent or chaotic (Koch and Wilczek [2021]).

One of the most prevalent and powerful tools in the analysis of active systems is the construction of correlation functions Kadanoff and Martin [1963]. These analytical tools allow us to measure the decay and propagation of some important relationship in space or time. Perhaps the most classic example of this type of analysis is the velocity autocorrelation function which measures the similarity of a velocity field to itself as a function

of distance or time (Forster [2018]). Traditional interpretations of these functions usually seek to extract a correlation length or time scale from a one dimensional projection (Thampi et al. [2013b]). Frustratingly, there is no guaranteed scaling in such functions. Therefore, fitting a decay function and extracting, say, an exponent to compare between correlation functions is impossible. As there is no consistent scaling amongst all of these functions, the length scales extracted from such analysis must come from some ansatz – such as the length at which the correlation reaches half its maximum value – and can be ambiguous and difficult to compare or interpret. To overcome these shortcomings, methods have been introduced in recent years to extract unambiguous quantities like average vortex size (Martínez-Prat et al. [2021]) or temporal decorrelation time from experimental measurements in active systems (Reufer et al. [2012]). These methods unfortunately can require different raw inputs or assumptions about an underlying dynamical model. Of great utility then would be a method that meaningfully extracts unambiguous length and time scales for active materials from a single method in a model free manner.

Here we introduce just such a method. We build off of recent work that extends the utility of correlation functions in thermally driven systems by taking into account the internal directions of a velocity field to extract the maximal amount of information from the correlation (Molaei et al. [2021]). We extend these directionally rectified correlation and introduce a generalized cross correlation function that effectively measures material response functions in active systems from data. Specifically, we set our function to work interpreting two dimensional displacement fields from a number of materials composed of the biopolymer F-actin driven by molecular motors from the myosin family. In these systems we show that this framework extracts model-free, unambiguous length scales as well as interpretable timescales from these easily accessible experimental fields. We show that the variety of measurements that can be made from our method are consistent with multiple, disparate established methods. Utilizing this technique we extract a

number of critical length and time scales that quantify complex dynamics, characterize disparate modes of relaxation, and presage incipient dynamical transitions across these diverse materials from liquid crystals to cells.

4.2 Method and Results

4.2.1 Measurement of response functions in 2D active materials

To begin, let us consider in the abstract the displacement field for a two dimensional active material. Fig. 5.1A shows one such field from an experimental active system. We will deal with the specifics of this experimental system in the next section but for now will treat it simply as some displacement field we wish to analyze. As typical active materials contain a number of length and time scales, our approach here will be to extract as much information as we can from this important dynamical field. To do so, we will approach correlation analysis not as conventional autocorrelation but as generalized cross correlation between some important field $\boldsymbol{p}$ and the displacement field $\boldsymbol{u}$. The real trick here will be to take special notice of any directional information in $\boldsymbol{p}$. This directional information will help the correlation to represent an averaged response of $\boldsymbol{u}$ to the specific perturbation represented by $\boldsymbol{p}$.

Because $\boldsymbol{p}$ could in principle be a high rank tensor field and interpreting high ranked correlation functions is difficult, we introduce the general correlation function $\chi_{\boldsymbol{p}}$.

$$\chi_{\boldsymbol{p}}(\boldsymbol{R},\tau) = \langle p(\boldsymbol{r}_1,t)\boldsymbol{u}(\boldsymbol{r}_2,t+\tau)\delta(\boldsymbol{R}-\boldsymbol{r}'_{12})\rangle_{r_1,r_2,t}, \tag{4.1}$$

here p is the scalar magnitude of the field $\boldsymbol{p}$ which renders $\chi_{\boldsymbol{p}}$ the same rank as $\boldsymbol{u}$. $\langle\cdot\rangle_{r_1,r_2,t}$ denotes averaging over space and time. Since p and $\boldsymbol{u}$ are often discrete measurements, the average is computed by binning our data over a window of chosen size, which is represented by the finite width delta function δ. $\boldsymbol{R}$ is the location in a new Euclidean

space with the same dimensionality as $\boldsymbol{u}$. Finally, $\boldsymbol{r}'_{12}$ is the distance vector between $\boldsymbol{p}$ and $\boldsymbol{u}$, which will be constructed in this new coordinate system to report on the location of $\boldsymbol{u}(\boldsymbol{r}_2)$ with respect to the position and heading of $\boldsymbol{p}(\boldsymbol{r}_1)$. The purpose of $\boldsymbol{r}'_{12}$ is to center the average such that each $\boldsymbol{p}(\boldsymbol{r_1})$ is located at the origin of $\boldsymbol{R}$. In practice, we will be dealing not with χ itself but rather the normalized correlation field $\boldsymbol{U_p} = \chi_p / \sqrt{\langle p^2 \rangle}$. In tandem with the field $\boldsymbol{p}$ the choice of coordinate system in which $\boldsymbol{r}'_{12}$ is measured is a critical one and has important ramifications for how we interpret these correlations. To see why let us consider a concrete example.

Let us consider the displacement-displacement auto-correlation function in this new setting; $\boldsymbol{U_u} = \chi_u / \sqrt{u^2}$. Our objective is to understand how the displacement field responds to each specific $\boldsymbol{u}(\boldsymbol{r_1})$. This means we want to take into account not only the location $\boldsymbol{r_1}$ but also the heading of $\boldsymbol{u}(\boldsymbol{r_1})$. To do so, we set up a new coordinate system whose Y axis aligns with $\boldsymbol{u}(\boldsymbol{r_1})$. That is, we define $\boldsymbol{r'_{12}} = \boldsymbol{M}(\boldsymbol{r_2} - \boldsymbol{r_1})$, where $\boldsymbol{M} = \begin{pmatrix} cos(\theta_1) & -sin(\theta_1) \\ sin(\theta_1) & cos(\theta_1) \end{pmatrix}$ is the rotation matrix in which θ_1 is the angle between $\boldsymbol{u}(\boldsymbol{r_1})$ and the Y axis of the lab frame. By defining $\boldsymbol{r}'_{12}$ in this way, $\boldsymbol{U_u}$ reports on the correlation of the displacement field with a perturbing vector pointing along the Y axis. By normalizing by $\sqrt{\langle u^2 \rangle}$ this correlation reports on the average behavior of the displacement field with respect to an impulse of defined direction and magnitude, (Fig. 5.1C). Put differently, the function $\boldsymbol{U}_u$ reports on the averaged *response* of the displacement field $\boldsymbol{u}$ to a perturbation of unit magnitude along the Y axis. This procedure is closely related to what was utilized recently to measure the Stokeslet flow induced by Brownian motion of passive colloids at an interface (Molaei et al. [2021]). By taking this directional information into account, the resulting response function is not radially symmetric as one would expect from traditional auto-correlation. Rather, the resulting displacement response function is reflectively symmetric about the Y axis and anticorrelated about the X axis (Fig. 5.1C,ii). As one might expect, the response to a displace-

ment along one axis decays at different rates for different angles with respect to that impulse. The response in the longitudinal direction $U_{u,\parallel} = U|_{X=0}$ propagates over the largest distance and in the transverse direction, $U_{u,\perp} = U|_{Y=0}$ over the shortest distance (Fig. 5.1C,ii). The difference between these two length scales is mainly related to the hydrodynamic coupling of the active material to the viscous bulk fluids (Levine and MacKintosh [2002], Chisholm and Stebe [2021], Martínez-Prat et al. [2021]). The ratio of these two length scales quantifies the ratio of the kinetic energy that is dissipated within the 2d system (active nematic in this case) and kinetic energy dissipated externally. These two spatial length scales, however, get convoluted when calculating conventional displacement auto-correlation function $C_{\boldsymbol{u}\cdot\boldsymbol{u}} = \langle \boldsymbol{u}(\boldsymbol{r}) \cdot \boldsymbol{u}(\boldsymbol{r}+\boldsymbol{R})\rangle_r / \sqrt{\langle \boldsymbol{u}(\boldsymbol{r}) \cdot \boldsymbol{u}(\boldsymbol{r})\rangle_r}$ as all perturbations $\boldsymbol{u}$ are treated identically regardless of heading. In fact, this traditional auto-correlation function is equal to the azimuthal average of the response function we consider, $C_{\boldsymbol{u}\cdot\boldsymbol{u}} = 1/2\pi \int_0^{2\pi} U_Y(\boldsymbol{R}) d\theta = (U_\perp + U_\parallel)/2$; where θ is the angle in polar coordinates. By taking into account the headings of each element of the displacement field as we construct the correlation function we are able to access important two dimensional features of flow responses. Unfortunately, while this description of the auto-correlation response contains more information than the previous version, determining a length scale from these functions still requires a model. This stems from the fact that any auto-correlation function must inherently be maximally correlated with itself at the origin. Without any universal scaling describing the decay of this correlation in active systems we are left to approximate. We will show that such ambiguity may not exist in higher order response functions.

To capture the response of the displacement field to high order modes of deformation, we explore the response of the displacement field to its own gradients, $\nabla \boldsymbol{u}$. In a linear system, we begin by decomposing displacement gradient tensor $\partial_i u_j$ into the anisotropic symmetric traceless strain rate tensor, $S_{ij} = (\partial_i u_j + \partial_j u_i)/2 - \partial_k u_k I_{ij}/2$, the isotropic sym-

metric strain rate tensor $D_{ij} = \partial_k u_k I_{ij}/2$, and the circulation tensor $\Omega_{ij} = (\partial_i u_j - \partial_j u_i)/2$. Here, $\boldsymbol{I}$ is an identity tensor with the same rank of $\partial_i u_j$. As we will see, this choice of decomposition has great physical utility as in two dimensions it corresponds to separating the contributions of pure shear, normal, and vortical deformation from one another. Having performed this decomposition, we construct a family of response functions $\boldsymbol{U_S}, \boldsymbol{U_D}, \boldsymbol{U_\Omega}$ corresponding to the response of the deformation field to the different perturbations, each of which quantifies different flow structures in $\boldsymbol{u}$. We will defer the physical interpretation of these response functions in the various systems for the later sections but will focus here on the methodology for constructing each. Specifically, let us focus on the critical question of how to choose a coordinate system.

Among these tensors, $\boldsymbol{D}$ – which quantifies bulk contraction or extension – does not have a unique eigendirection and can be fully described by its first principal invariant. Therefore it can be treated as scalar field, D. As scalar fields do not have headings, we cannot choose a meaningful angle about which to rotate. In such cases, we default to a translation of the lab frame (Fig. 5.1D,i). More precisely, in the case of a scalar perturbation field we simply take $\boldsymbol{r'_{12}} = (\boldsymbol{r_2} - \boldsymbol{r_1})$. A similar situation arises with the circulation tensor $\boldsymbol{\Omega}$ in two dimensions. This tensor has only one pseudovector which is normal to the plane of observation with rotation rate equal to vorticity $\nu = \hat{\boldsymbol{e}}_z \cdot \boldsymbol{\nabla} \times \boldsymbol{u}$. As the pseudovector of $\boldsymbol{\Omega}$ provides no extra information, we will use the scalar vorticity field, ν, throughout this work and choose the simple translation of the lab frame as our coordinate system (Fig. 5.1D,i). In the case of both D and ν, the resulting response function is radially symmetric which is a product of the lab frame coordinate that we have chosen (Fig. 5.1D,ii). Intuitively also, we expect a system's response to vortical perturbation, $\boldsymbol{U}_\nu$ or normal deformation to be radially symmetric which is the case in the measured responses (Fig. 5.1D,ii).

Unlike its cousins, $\boldsymbol{S}$ is not a scalar field and thus requires more care when choosing co-

ordinates. $\boldsymbol{S}$ possesses two eigenvectors which identify pure shear directions with eigenvalues $\pm\lambda$ indicating shear rate. To construct $\boldsymbol{\chi}_S$ in this case we setup a coordinate system similar to the case of displacement auto-correlation where the Y axis is aligned with the eigendirection corresponding to the positive eigenvalue, (Fig. 5.1E,i). It is important to note here that it does not truly matter which eigenvector we choose so long as we are consistent while constructing the response function. As a convention we have chosen the eigenvector associated with positive shear as we will eventually turn this method on an extensile system. The eigenvalue of $\boldsymbol{S}$ in this direction, λ, is used as the scalar field which normalizes the correlation. The shear response function we construct, $\boldsymbol{U_S} = \boldsymbol{\chi}_S/\sqrt{\lambda^2}$ is therefore the response function of the system to a pure extensile shear perturbation at the origin pointing outwards along the Y axis as seen in Fig. 5.1E,i. Since $\boldsymbol{S}$ is a symmetric and traceless tensor, the resulting response function $\boldsymbol{U_S}$ is symmetric about both X and Y axes (Fig. 5.1E,ii). This is the high rank extension of what we have seen already. Scalar fields, having no internal directions in the plane, form radially symmetric correlation functions while vector fields yield only one axis of symmetry. This response to a second rank tensor which represents bidirectional motion yields a response function that is symmetric about two separate axes.

So far we have only measured equal-time response functions. Evaluating the response after some lag time however is straightforward. Taking a perturbation field $\boldsymbol{p}(\boldsymbol{r}_1)$ at time t the delayed response function is constructed from $\boldsymbol{u}$ measured after some delay time $t + \tau$. A snapshot of the velocity field from Fig. 5.1A measured at $\tau = 12s$ is shown in Fig. 5.1B. From these two displacement fields corresponding response functions $\boldsymbol{U_u}(\tau)$, $\boldsymbol{U}_v(\tau)$, and $\boldsymbol{U_S}(\tau)$ are computed at $\tau = 12s$ (Fig. 5.1C-E,iii). The spatiotemporal response functions as measured here provide useful information about spectral properties of the dynamics of active matter in the time domain to which has proven challenging so far to gain access to (Alert et al. [2022]).

Thus far then we have focused solely on technical implementation. We have demonstrated that by taking into account internal headings of a perturbing filed, we can use the familiar language of correlation functions to construct functions that report on the response of a displacement field to these specific perturbations. After decomposing the displacement gradient tensor into constituent parts we demonstrated how to construct similar response functions for various ranks of perturbing inputs. Finally we have seen a simple procedure to extend this framework into the time domain. Having detailed these technical steps, we now turn our analysis on a few real systems. We will ask what information our method can give us and compare to previously established methods for a few well characterized active systems.

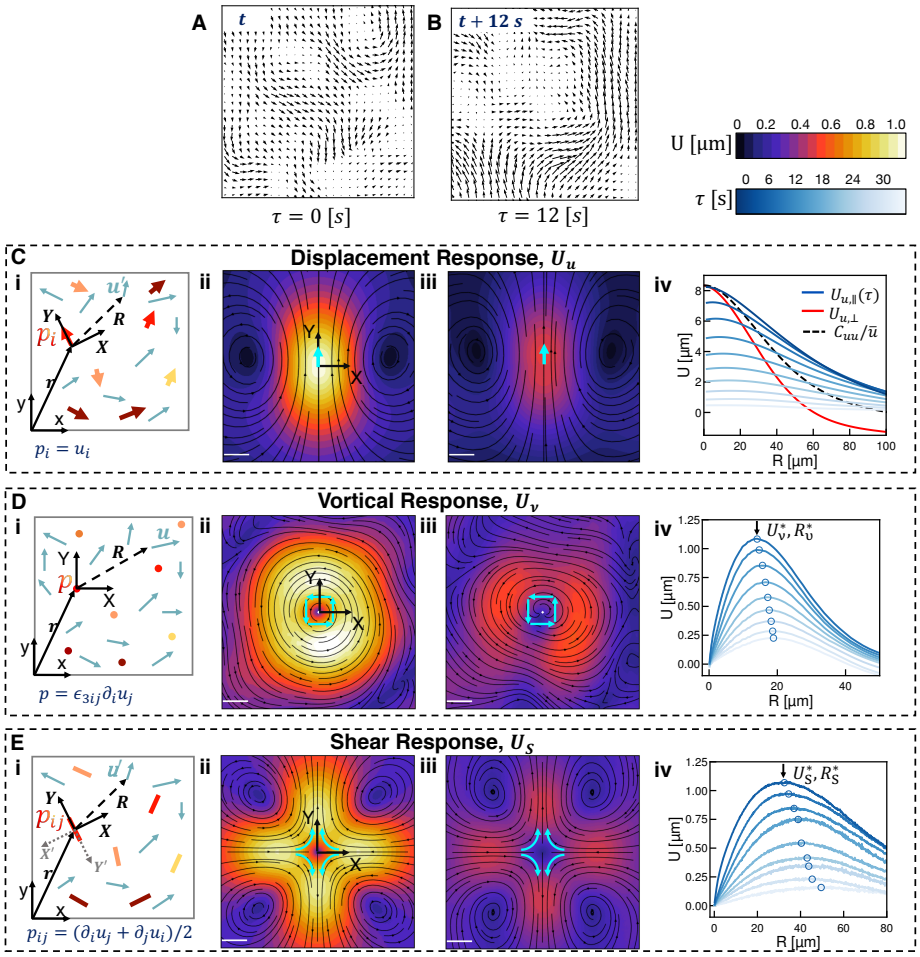

Figure 4.1: **Measuring directionally rectified correlations reveals response functions in active materials.** A,B) Displacement fields measured by optical flow from fluorescence microscope images of an active nematic liquid crystal composed of actin filaments at $t = 0s$ (A) and $t = 12s$ (B). Displacements measured over $\Delta t = 2s$. (i) Schematic of coordinate transformation and ensemble formation for the response of the two dimensional displacement field $\boldsymbol{u}$ to various perturbation fields $\boldsymbol{p}$. $\boldsymbol{p}$ is either the displacement field itself (C), the vorticity field (D), or the shear field (E). (ii) Equal time two dimensional correlated displacement field. The response of the displacement field in (A) to each of the respective perturbations. Ensembles are constructed such that the Y axis in (i) is the same as (ii). Streamlines indicate the direction of the resulting correlation field and color indicates the magnitude; scale bars are $5\mu m$. (iii) The $\tau = 12s$ time delayed correlated displacement fields. The perturbation coordinate system is set at $\tau = 0s$ and the response is measured at $\tau = 12s$. (iv) One dimensional profiles of the fields calculated at various lag times. Lighter colors indicate longer lag times. C,iv) One dimensional profile is constructed by tracing along the major axis (blue). Note that the azimuthal average is simply the average of the major axis trace and the minor axis trace (red). D,iv) One dimensional profile is constructed by azimuthally averaging. Model free characteristic deformation

U^* and length R^* scales at the various lag times indicated by open circles. E,iv) One dimensional profile constructed as a trace along the Y axis. The origin symmetry of the field shown is unique to divergence free systems. Note the large characteristic length scale in comparison to vortical deformation fields.

4.2.2 Flow Structures Reveal Characteristic Length Scales in 2D Active Nematics

We will begin analyzing the dynamics of real active systems by analyzing the flow structures of an active nematic liquid crystal. Nematic liquid crystals, or simply nematics, are materials composed of elongated components called nematogens that interact through excluded volume. At sufficient concentration nematogens locally align which yields a material with long range structure (Gennes and Prost [1993]). However, because the nematogens are not bound to each other, individual components and even entire structures can flow and move within the material. These temporal dynamics are particularly interesting when local stresses drive the nematic out of thermal equilibrium leading to an active state (Doostmohammadi et al. [2018]). Here we consider a nematic composed of short actin filaments into which activity can readily be introduced via the addition of mysoin motors which slide antiparallel pairs of filaments past each other generating local extensile stresses (Kumar et al. [2018]). These stresses propel and nucleate topological defects within the nematic and result in long range flows (Giomi et al. [2014]). Figure 5.1A presents a snapshot of displacement field $\boldsymbol{u}$ measured over $\Delta t = 2s$ for one instance of such a system.

Nematics are an attractive system to test our method as their steady state dynamics in two dimensions feature well studied length and time scales (Thampi et al. [2014a]). As we saw earlier, using our formulation of $\boldsymbol{U_u}$ we see a difference in decay length between in the directions parallel and perpendicular to the motion heading (Fig. 1C,ii). However, as already discussed, these traces unfortunately do not allow for the extraction of

an unambiguous length scale as quantifying the decay would require a model or ansatz, Fig. 5.1C,ii. Luckily, not all of the response functions we constructed monotonically decay.

One such example is the vortical response function $\boldsymbol{U}_\nu$. When we azimuthally average the vortical response function and plot the resulting one dimensional projection, $U_\nu(R)$, we find a clear maximal value (Fig. 5.1D,iv). Since the helicity $\langle \nu(\boldsymbol{r})\boldsymbol{u}(\boldsymbol{r})\rangle_{\boldsymbol{r}}$ in a 2D nematic field is zero–at least in the linear region where there is no energy transfer across scales (Alert et al. [2020])– U_ν starts from zero at the origin and rises to the characteristic value before decaying at large distances due to various viscous and frictional dissipation mechanisms. The peak of this function gives a critical magnitude U_ν^* at a characteristic distance of R_ν^* which we interpret as the characteristic magnitude and length scale of vortically driven flows (Fig. 5.1D,iv). In the case of the nematic considered here the critical length scale is $R_\nu^* = 14.1\mu m$. In order to put this number in the context of previous work, we compare this length scale to the average vortex size in the nematic. We measure the distribution of vortex sizes in the current system using the standard Okubo-Weiss parameter and velocity winding number (Lemma et al. [2019], Giomi [2015], Guillamat et al. [2017]). In 2D active nematics, it is expected that vortex area follows an exponential distribution with rate parameter of average vortex size a_ν^* (Lemma et al. [2019]). Applying this assumption to our distribution we find an average vortex area of $a_\nu^* = 688 \pm 9\mu m^2$. This average vortex size is in close agreement with vortex area calculated from our model free vorticity length scale which gives $\pi(R^*)^2 = 624\mu m^2$. As we expected, the length scale that this response function returns is that of high order flow structures arising from the specific perturbation considered. Specifically in this case, the vortical response function sports a critical length scale that is commensurate with the radius of an average vortex in the system. Given this meaningful response, we now turn to the flow structures associated with higher order, shear deformations.

The shear response function $\boldsymbol{U}_S$ measures the response of the material to shear stresses

at the origin (Fig. 5.1E,ii). One striking feature of $\boldsymbol{U_S}$ in the context of an active nematic is the high degree of reflective symmetry. In this case $\boldsymbol{U_S}$ is symmetric about not only the X and Y axes as we would expect from the response to a second order tensor, but also the diagonal $Y = X$. As we will see, this diagonal symmetry is not general to every system. In fact, this symmetry arises from the incompressibility of the nematic film which is critical for its dynamics. This incompressibility is also why the normal response $\boldsymbol{U}_D$ is insignificant in this context as there is no significant contraction and thus the response of the system to this negligible perturbation is itself negligible. As in the case of the vortical response, we want to consider a simplified one dimensional representation of this two dimensional function. Because $\boldsymbol{U_S}$ is diagonally symmetric, we can consider only the one dimensional trace along the Y axis (Fig. 5.1E, iv). Similarly to the vortical response, this one dimensional trace rises from zero at small length scales and decays due to various dissipation mechanisms giving a critical magnitude, U_S^*, and length scale, R_S^*, of flow structures associated with shear perturbation. In this case, this one dimensional response trace starts from zero at the origin because inertial advection $\boldsymbol{u} \cdot \boldsymbol{\nabla u}$ at small length scales in an active nematic is zero.

It is interesting to note that while both U_ν and U_S have characteristic length scales these two scales are disparate. In fact, we find that in general $R_S^* > R_\nu^*$. This is because the shear deformation field $\boldsymbol{U_S}$ is coupled to pressure gradients in the system while the vortical deformation field, in the absence of inertial effects, is not (Batchelor [2000], Marchetti et al. [2013]). Vortical perturbation at the origin only propagates by the curl of force density due to elastic, flow-alignment, and active stresses and thus is dictated in large part by the systems shear rheology (Martínez-Prat et al. [2021]). While the characteristic length scales quantifies the size of the flow structures, the characteristic displacement scales U_S^* and U_ν^* identify the energy level within these flow structures.

Together model-free characteristic deformation scales, U^*, and length scales, R^* pro-

vide scaling factors that map high order flow structures on unified interpretable profiles. Here we have focused on how to extract and interpret these scales for a single system. However, because these scales are model-free and unambiguous they easily allow for comparisons between experiments. For example, the normalized correlated deformation profiles $U' = U/U^*$ plotted as a function of the normalized distance $R' = R/R^*$ for active nematics with different levels of activity exhibit a scaling law across length scales. Scaling laws in active turbulence have been an ongoing topic of scientific discussions in recent years (Alert et al. [2020], Koch and Wilczek [2021]) and we hope the generality of our framework will prove a useful tool in their investigation. We will next turn our attention to a system that is in many ways more complicated than a nematic; a contractile gel.

4.2.3 Spatial features of deformation fields reveal the onset of contractile instability in an active gel

Thus far we have only considered an active nematic which is an incompressible material with steady state dynamics. To test the broad applicability of our method to dynamics not necessarily at steady state we now turn to a different type of active actomyosin material; a contractile actin gel. Unlike ordered nematics formed by short, rigid actin filaments, disordered gels are formed by networks of long semi-flexible filaments (Gardel et al. [2004]). Because the filaments in these gels are semi-flexible the application of myosin stresses leads in general not to extensile stresses but rather contraction (Murrell and Gardel [2012], Lenz et al. [2012]). Irreversible local contraction is mediated by local filament buckling which at a large scale manifests as macroscopic structural changes and unstable contractile flow (Stam et al. [2017]). These structural rearrangements can be seen in the accumulation of actin fluorescence in micrographs of the system and cluster formation of associated myosin motors (Fig. 5.2 A-C,i, actin fluorescence in grey scale, myosin

fluorescence in magenta). The contractile flow can be seen in the increased coherence of the displacement field (Fig. 5.2 A-C,i, cyan arrows). This qualitative metric of contractility can be quantified by measuring the divergence of the displacement field $\langle \boldsymbol{\nabla} \cdot \boldsymbol{u} \rangle$ (Fig. 5.2D, black circles). One interesting feature of this system is that after the addition of myosin motors the system does not contract immediately. Rather as myosin filaments settle onto the network and stresses slowly build up, the divergence of the system remains negligible for a time before rapidly decreasing as the system irreversibly contracts (Fig. 5.2D). This delay has been a particular focus of studies on active gels, specifically the relation between the buildup and spectrum of internal stresses and the stability or contractility of the system (Marchetti et al. [2013]). To capture this interesting temporal evolution in detail we consider the system at three different stages of contractility with divergences $\langle \boldsymbol{\nabla} \cdot \boldsymbol{u} \rangle$ of ~ 0, ~ 0.01, and ~ 0.1 and measure the shear response, $\boldsymbol{U_S}$ and normal response $\boldsymbol{U}_D$ at these stages (Fig. 5.2D, time points analyzed labeled upper axis). As we should expect, the normal response increases with increasing divergence (Fig. 5.2A-C,iii). While this result straightforwardly corresponds to our intuition, something more interesting arises in the case of shear response. Note here that whereas in the extensile nematic we constructed the response function from positive eigenvalues with the corresponding eigenvectors pointing along the Y axis, for the contractile gel we will perform the same procedure but pointing the eigenvectors from the negative eigenvalues along the Y axis (Fig. 5.1E,ii and Fig. 5.2A,ii blue arrows).

One striking feature of the shear response is the conspicuous symmetry breaking in highly contractile regimes. Specifically, we find that in this system, the shear response in the transverse direction decays more quickly than the major axis of contraction (Fig. 5.2B,ii, comparing the X (transverse) and Y (contraction) axes). As divergence increases from $\langle \boldsymbol{\nabla} \cdot \boldsymbol{u} \rangle \sim 0.01$ to $\langle \boldsymbol{\nabla} \cdot \boldsymbol{u} \rangle \sim 0.1$ this asymmetry becomes even more pronounced (Fig. 5.2B-C,ii). This is precisely because the gel is compressible and is the counterpoint to the sym-

metry observed in the incompressible nematic (Fig. 5.1E,ii). Invoking incompressibility in the nematic is simply another way to say that the velocity flux around the point of perturbation must be zero. We can think about the deviation from this idealized behavior in the gel as the addition of an isotropic response that represents the net contraction of the system due to shear perturbations. To isolate these different modes of deformation $\boldsymbol{U_S}$ can be separated into an isotropic and anisotropic part $\boldsymbol{U_S} = [-U_{\boldsymbol{S}R,aniso}\cos 2\theta + U_{\boldsymbol{S},iso}]\hat{\boldsymbol{e}}_R + U_{S_{\theta,aniso}}\sin 2\theta\hat{\boldsymbol{e}}_\theta$, where $\boldsymbol{U_{S,aniso}}$ gives the strain dipolar modes, and $\boldsymbol{U_{S,iso}}$ gives the compressional mode. Splitting the response in this fashion allows us to track the progression of contraction in the gel directly from the shear response. Specifically, the azimuthal average of the isotropic shear response per unit area at $R^*_{\boldsymbol{S}}$, $U_{\boldsymbol{S},R^*,iso}/R^*_{\boldsymbol{S}}$, is equal to average divergence of the displacement field (Fig. 5.2D, solid black line). The isotropic shear response $\boldsymbol{U_{S,iso}}$ then, is reporting on the magnitude of contractile flows induced by local shear. Thus in this system which is driven by the local sliding of pairs of filaments (Murrell and Gardel [2012]), this response captures the global divergence. It should be noted here the difference between $\boldsymbol{U_{S,iso}}$ and $\boldsymbol{U}_D$. While $\boldsymbol{U_{S,iso}}$ captures the contractions due to local shear, the normal response $\boldsymbol{U}_D$ measures the system's response to these contractions. Considering the azimuthal average of each, we find that both $U_{\boldsymbol{S},iso}$ (Fig. 5.2E, dots) and U_D (Fig. 5.2F) increase as contractility increases (Colors correspond to divergences indicated in Fig. 5.2D). However while $U_{\boldsymbol{S},iso}$ is more or less constant as a function of distance R, U_D exhibits a clear peak indicating a length scale over which contractility driven flows are maximally felt in the material (Fig. 5.2E,dots and Fig. 5.2F). While this peak does not appear in the isotropic response, it does emerge in the anisotropic part of the shear response (Fig. 5.2E, solid lines). Furthermore, as contractile flows in the material increase, the energy scale and extent of this local shear response – both R^* and U^* – grow monotonically. Interestingly, after these peaks none of these responses decay fully to zero (Fig. 5.2E,F). As noted in the nematic, at steady state we expect dissipation to cause this

far field response to decay to zero. The lack of such a complete decay in the far field ($R > R^*$) indicates that the dynamics in highly contractile gels do not occur at steady state.

In addition to specifically enumerating these bulk consequences of contractile stress, the resolution of our measurement reveals features of the deformation fields that seem to presage the onset of contractility. As discussed earlier, since shear deformation is coupled to the pressure field, the length scale associated with its response, R_S^* is larger than the length scale in the vortical response R_ν^*. Interestingly, the ratio R_ν^*/R_S^* in the gel increases almost to a value of one while the gel is stable and before the appearance of negative net divergence (Fig. 5.2D). The ratio reaches its maximum value just at the onset of global contractility $\langle \boldsymbol{\nabla} \cdot \boldsymbol{u} \rangle < 0$. It has been shown that as a network of semi-flexible F-actin is driven out of equilibrium, the rate of energy dissipation and filament bending energy increases in the stable state until the appearance of contractile motion (Seara et al. [2018]). In this light, it appears that as motor stresses in gel increase, the bending and buckling deformations of filaments begin to decouple the pressure and shear deformation fields until bulk contraction once again suppresses these fluctuations. These insights into material properties have been garnered from equal time responses. We now explore what additional information can be gained by considering responses in the time domain.

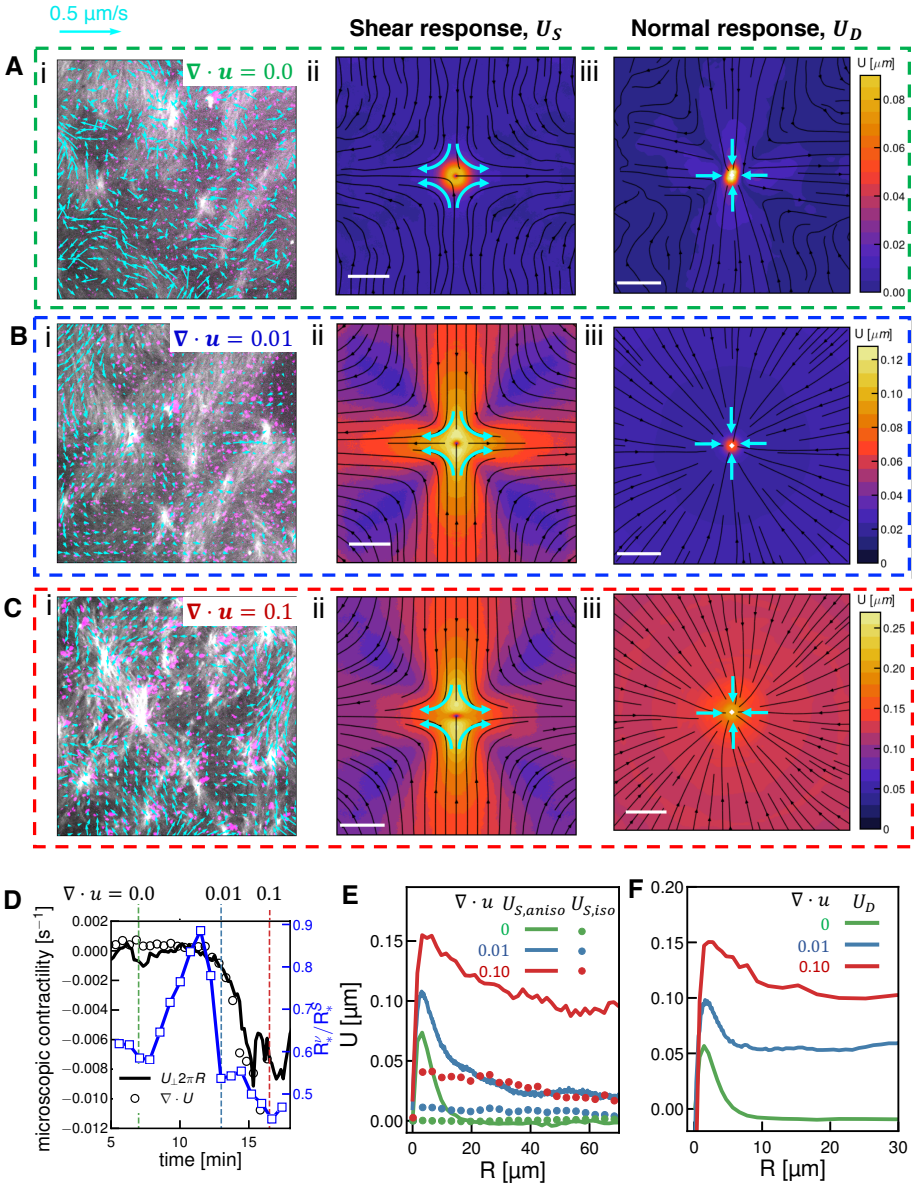

Figure 4.2: **Response functions identify key dynamical consequences of contraction in *in vitro* actomyosin networks.** i) Micrographs of fluorescent actin (gray) overlaid with scaled velocity vectors (blue) for the active gel at various divergences (A-C). Colors correspond to divergences indicated in (D), each box is $100x100\mu m^2$ of the field of view. ii) Equal time shear response for the velocity fields in (i). iii) Normal (compression) response for the velocity fields in (i). Streamlines indicate the direction of the resulting correlation field and color indicates the magnitude; scale bars are $5\mu m$. D) Divergence of the velocity field (black circles) as a function of time for a contractile active gel. The azimuthal average of the isotropic shear response at $R = R_S^*$ per unit area $U_{S,iso}(R_S^*)/R_S^*$ (solid black line) agrees with the calculated divergence. The green, blue, and red dashed lines

indicate the points taken as characteristic of the gel before contraction, at the onset of contraction, and deep in the contractile regime. Numerical labels indicate the value of divergence at these points. Ratio of characteristic length scales R_ν^*/R_S^* as a function of time (solid blue line, open blue squares) presage the onset of contractility. Time axis indicates elapsed time after the addition of myosin motors. (E) One dimensional traces of the symmetric $U_{S,iso}$ (solid lines), and anisotropic $U_{S,aniso}$ (dashed lines) decomposition of the shear response function in (ii). The symmetric response gets stronger and propagates to larger distances and the asymmetric response becomes non-zero as the magnitude of contraction increases. (F) One dimensional traces of the normal (compressional) response function in (iii).

4.2.4 *Temporal features of deformation fields reveal length scale dependent phenomena*

So far we have focused on response functions in the spatial domain, extracting characteristic deformation magnitudes and length scales. There is however more information that can be extracted from these functions in the time domain. Specifically we will examine the relaxation of response functions as the lag time between the perturbation and measured response increases. These time delayed response functions help elucidate the spectral features of active structures in the time domain which gives a great deal of insight into material properties and remains an active area of interest in active materials (Alert et al. [2022]).

Consider the one dimensional profile of the shear response in an active nematic $U_S(\tau)$ as a function of lag time (Fig. 5.3A, red curve). While all of the delayed responses share a similar form, the characteristic deformation magnitude U_S^* decreases and the critical length scale R_S^* increases as τ grows until at longer lag times the response is negligible (Fig. 5.3A, red curves; lighter colors indicate longer lag times). This steady decorrelation in time is characteristic of viscous dissipation. The magnitude of the response in an active gel similarly decays for a time. However instead of monotonically approaching zero as in the nematic, after seeming to decorrelate fully the response of the gel becomes

negative before settling back to zero at long lag times (Fig. 5.3A, blue curves). This anticorrelated signal is a strong signature of elastic behavior in the network. However it should be noted that the magnitude of the negative signal is never as large as the $\tau = 0s$ signal. This is because these networks are not purely elastic, rather they are viscoelastic; containing some character of an elastic network and some character of a viscous fluid. To confirm this interpretation, we compare gels with and without the addition of the actin severing protein cofilin which dissipates elastic stress through filament severing (McCall et al. [2019]). We find that a gel with cofilin never anticorrelates as is consistent with its role in preventing stress buildup in actin networks. Given sufficient temporal resolution then, measuring response functions in the time domain allow for an understanding of the balance of viscous and elastic behaviors in a given system.

Temporal responses are not only useful for enumerating the differences in dynamics between systems but also for extracting scale dependent phenomena within the same system. To extract such scale dependent information we consider the magnitude of the shear response within the nematic system $U_S(\tau)$ at a number of length scales relative to that of the peak R_S^*. These magnitudes are normalized by $U_S(R, \tau = 0s)$ to give length scale dependent relaxation, Fig. 5.3B. This analysis reveals that in an active nematic relaxation time is scale-dependent, with smaller scale structures relaxing faster than those with larger length scales (Fig. 5.3B). To quantify these relaxation profiles, they are fit to a scaled exponential function, $U(\tau) = \exp\Big(-[\tau/\tau_r(R)]^{\gamma(R)}\Big)$; where $\tau_r(R)$ is the size dependent decay time and $\gamma(R)$ is the scale dependent scaling factor. At short length scales, the shear response relaxes with exponent $\gamma = 1$ which is the scaling expected from diffusive relaxation (Fig. 5.3B, red curve). At large scales however, the relaxation profile follows a compressed exponential with $\gamma = 2$, diagnostic of ballistic type motion with a smooth transition between these two extremes at intermediate scales (Cipelletti et al. [2000], Lee et al. [2021]) (Fig. 5.3B, blue to green).

Previous studies have analyzed similar scale-dependent relaxation in active systems using the technique of differential dynamic microscopy (DDM) which treats dynamics from microscopy experiments as a scattering problem (Reufer et al. [2012], Lee et al. [2021]). This approach is necessarily agnostic of the differences between temporal decorrelations born of stationary structural rearrangements and those due to flow. Analyzing the scale-dependent dynamic structure function $D(q, \tau)$ for the same active nematic considered above gives qualitatively similar results. Figure 5.3C shows dynamic structure function for several wave numbers q. At small length scales i.e., large wave numbers, the relaxation of $D(q, \tau)$ follows a power law with scaling exponent one indicative of diffusive motion (Fig. 5.3C, light blue). Echoing our response function analysis, we find at longer scales the power law relaxation of $D(q, \tau)$ approaches two; indicating ballistic like scaling (Fig. 5.3C, blue). While the types of scaling extracted by each method agree in extreme scales, the characteristic decay times each extract do not agree.

The relationship between the characteristic decay time and the spatial scale is a useful measure to capture the detailed dynamics of active nematics. We define the decay time from scale-dependent response measurements, $\tau_r(q = 2\pi/R)$ as the time that the normalized response profile (Fig. 5.3B) relaxes to the inverse of the Euler number, ~ 0.368. We similarly define the relaxation rate $\tau_r(q)$ from DDM as the time when D reaches 63.2% of $D(q, \infty)$; where $D(q, \infty)$ is the plateau value at long lag time. Comparing the characteristic times extracted from these two methods as a function of spatial scale we find that the characteristic times that DDM extracts are uniformly shorter than relaxation times found using our response analysis (Fig. 5.3D, black squares DDM, colored squares response analysis). Furthermore, this is not the product of a mere baseline shift but rather of markedly different scaling (Fig. 5.3D). As length scale decreases, the relaxation time predicted by DDM scales as $\tau \sim 1/q$ while over the same range displacement response relaxation becomes q independent, $\tau_r \sim q^0$ widening the discrepancy between the two

predictions (Fig. 5.3D). This is all the more curious as the types of relaxation found as a function of lag time is commensurate between the two methods (Fig. 5.3B-C). This disconnect can be understood as DDM relaxation necessarily combines advection of material structure and dynamical relaxation processes. As such DDM correlations relax quickly. The displacement response on the other hand stops scaling below the agent size in the system which is $\sim 1\mu m$ here (Fig. 5.3D, colors). This indicates that this measure is providing direct access to meaningful dynamics within the active system. The decay rates of shear and vortical responses do not fully become scale independent but rather scale weakly with the wave number in small scales, $\tau_r \sim q^{-0.2}$ (Fig. 5.3D, blue and red). The distinguished scaling for different types of flow structures gives us confidence that correlated displacement fields are indeed capturing important dynamical features in this active system. However, this scaling is not universal and changes as the dynamics and flow structures in the active turbulent state change.

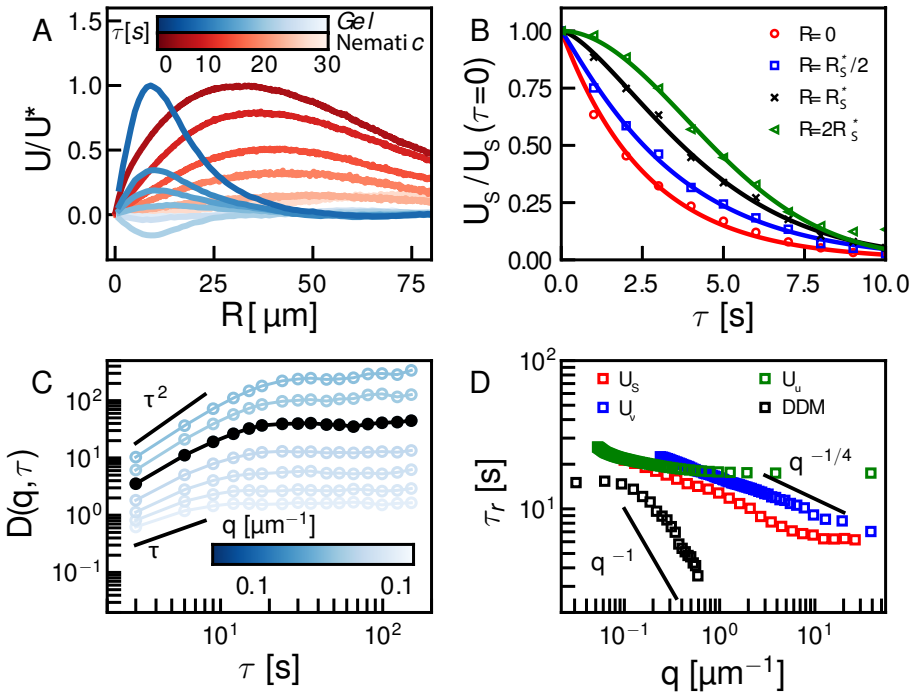

Figure 4.3: **Temporal dependence of correlated displacement field reveals characteristic time scales of active materials**. A) Normalized correlated displacement fields for a nematic (black) and active gel (red) at $\tau = 0s$ (open symbols) and $\tau = 10s$ (closed symbols). B) Normalized strain correlated displacement as a function of delay time τ at different spatial scales with respect to the critical length scale R^* showing different scaling at various length scales. Experimental data in indicated with symbols solid lines are fit to stretched exponential. C) Dynamic structure function $D(q, \tau)$ (open circles) measured with differential dynamic microscopy (DDM) as a function of spatial scale (circle color). q^2 and q scaling at low τ indicate ballistic and diffusive like scaling respectively. Characteristic time scales τ as a function of spatial scale q for DDM (black) and displacements correlated with monopolar (green), dipolar(red), or vortical (blue) perturbations.

4.2.5 *Response functions differentiate modes of cellular contractility*

We now explore whether our method can distinguish different modes of contractility in subcellular actomyosin architectures. In adherent cells actomyosin is organized into networks and bundles with highly stereotyped architecture and dynamics. Transverse arcs are actomyosin bundles formed near the cell periphery and oriented parallel to the cell edge. Myosin activity continually drives the coalescence and contraction of transverse

arcs resulting in their in continual inward motion; a dynamic process known as retrograde flow (Gardel et al. [2008], Ponti et al. [2004], Lin et al.). In contrast, ventral stress fibers are highly stable actomyosin bundles anchored on each end by focal adhesions (Hotulainen and Lappalainen [2006], Tojkander et al. [2012]). While both architectures can coexist, U2OS and NIH 3T3 cells predominantly display transverse arcs and ventral stress fibers, respectively (Fig. 5.4A,B). We probe the dynamics over 10 second intervals using time-lapse imaging of fluorescent myosin II puncta and calculate displacement fields (Fig. 5.4A,B, stress fibers grey, flow field blue arrows).

The shear response $\boldsymbol{U_S}$ is then calculated for different lag times (Fig. 5.4ii) and as in Fig. 5.2E is split into one dimensional traces of the anisotropic $U_{S,ansio}$ (Fig. 5.4iii) and isotropic $U_{S,iso}$ (Fig. 5.4iv) components. The most dramatic difference between these architectures is in the isotropic shear response. In transverse arcs this response increases linearly as a function of distance and does not diminish over time, reflecting long range and coherent retrograde flow (Fig. 5.4A,ii,iv). The isotropic shear response is entirely absent in ventral stress fibers reflecting a lack of contractile dynamics (Fig. 5.4B,ii,iv). In contrast to the differences in the isotropic shear response, in both cases the anisotropic shear response at $\tau = 0s$ is peaked around $1\mu m$ (Fig. 5.4A-B,iii red). This reflects a similar length scale of maximal shear distortion. By $\tau = 10s$ the anisotropisc shear response in transverse arcs decays completely (Fig. 5.4A,iii blue). This indicates that shear deformations in transverse arcs decorrelate faster than the time scale τ. In contrast, in ventral stress fibers $U_{S,ansio}$ persists at $\tau = 10s$ (Fig. 5.4B,iii blue) reflecting longer lived shear distortions. The disparity in anisotropic shear response at later lag time reveals differences in local dissipation of shear stress arising from differences in boundary conditions and local mechanical properties.

Both ventral stress fibers and transverse arcs reflect steady state dynamics common in adherent cells. Perturbations around these steady states can be queried via recently

developed optogenetic techniques. Regional activation of RhoA in NIH 3T3 cells drives increased local actomyosin contractility and induces flow of adjacent ventral stress fibers portions (Oakes et al. [2017]). We measure the shear response of ventral stress fibers prior to (Fig. 5.4B) and during (Fig. 5.4C) $5min$ optogenetic activation in the orange box indicated in Fig. 5.4C,i. Activation induces a shear response qualitatively similar to transverse arcs but with some important distinctions. The most notable similarity is that upon optogenetic activation, ventral stress fibers exhibit a linearly increasing isotropic shear response that is consistent over $\tau = 10s$ but with a decreased magnitude (Fig. 5.4C,iv). This underscores that a spatial gradient of contractile stress is sufficient to induce long range coherent flows in ventral stress fibers (Fig. 5.4C,iv). Interestingly, the anisotropic shear response at short scales of ventral stress fibers with and without regional activation are qualitatively similar (Fig. 5.4A-C,iii). In longer length scales however, while the anisotropic response decays to 0 in the case without regional activation, the stimulation of RhoA induces a far field response that does not fully decay reflecting the departure of the system from steady state dynamics (Fig. 5.4A-C,iii). This plateau indicating a departure from steady state is similar to what was observed in the case of the active gel as divergence increased (Fig. 5.2E, solid lines). The short and long range behavior of $U_{S,ansio}$ over lag times allow us to discern local mechanical properties and degree of mechanical homeostasis in cellular actomyosin architectures.

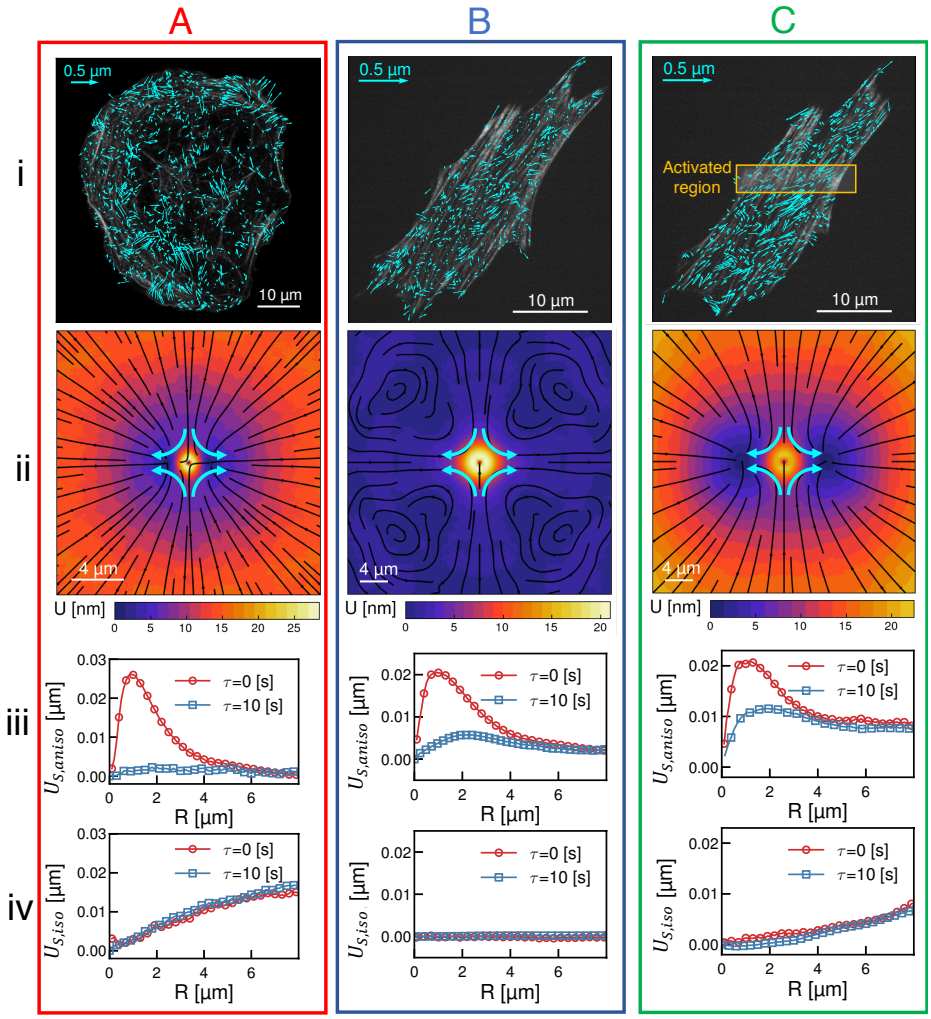

Figure 4.4: **Spatiotemporal features of response functions differentiate complex deformation modalities in living cells.** (i) Micrographs of the actin fibers (grey) overlaid with myosin displacement vectors (blue) for different contractile modalities. The modalities considered are A) transverse arcs (in a U2OS cell), B) ventral stress fibers (in an NIH 3T3), and C) optogenetically activated ventral stress fibers (NIH 3T3). 1 out of 6 displacement vectors are shown. The orange box in (C,i) indicates the region of optogenetic activation. (ii) Shear response $\boldsymbol{U_S}$ for the displacement fields shown in (i). Streamlines indicate the direction of the response and color indicates the magnitude. (iii, iv) One dimensional traces of the anisotropic, $\boldsymbol{U_{S,aniso}}$ (iii), and isotropic $\boldsymbol{U_{S,iso}}$ (iv), parts of the shear response shown in (ii) measured at lag times of $\tau = 0s$ (red) and $\tau = 10s$ (blue).

4.3 Conclusions

As we can see from the above examples, by constructing correlation functions in an appropriate frame of reference we measure an averaged material response function that provides a wealth of information about active materials distilled only from easily accessible experimental data. By constructing correlations with respect to an appropriate internal heading and considering meaningful cross correlations we are able to extract a family of functions that characterize the response of a system to defined perturbations. Specifically we focused here on how material response to vortical, displacement, and shear perturbations shed important light onto the dynamics of active actomyosin materials. Specifically we found that the critical length scale of the vorticity response in an active nematic, R_V^*, was equal to the average vortex radius measured with traditional analyses. The shear response, appropriately decomposed, captured not only the magnitude of bulk contractions but also far field shear driven rearrangements in a contractile gel. Furthermore, the ratio of vortical to shear correlation allowed us to characterize the onset of contractility in an active gel. Harnessing correlations in the time domain we were able to differentiate viscous and elastic responses to shear as well as scale dependent relaxation phenomena. Finally, combining both spatial and temporal analyses of shear correlations allowed us to differentiate between types of actomyosin dynamics and mechanics inside of living cells and enumerate the consequences of optogenetic RhoA activation. The measurements highlighted here though are just the beginning of what can be understood with this method.

The specific measurements presented in this work are in many ways simply the lowest hanging fruit. With only moderate effort one could imagine straightforward extensions or applications of this method that could elucidate important dynamics well beyond what we have shown here. We saw earlier how the temporal relaxation of the model free characteristic length scale R_S^* and deformation scale U_S^* elucidated the signatures of viscoelas-

ticity. One could imagine making this notion much more precise by explicitly tuning the mechanics of a cell or in vitro system and characterizing these varied responses. Such analysis would allow for the explicit understanding of the viscoelastic consequences of such perturbations. We showed that relaxation – and thus material responses – varied as a function of spatial scale. By the same token, we expect the far field portion of the response function, $\boldsymbol{U}(R > R^*)$ to reveal important hydrodynamic and physical coupling both within various systems and with their external environments. These, as all of the measurements presented in this work, are only a few of the possible quantification of active systems using data derived response functions.

Throughout this work we considered the response of the displacement field $\boldsymbol{u}$ to some perturbative fields $\boldsymbol{p}$. This was motivated by our specific interest in active systems and their dynamics. However, this method is not limited to these specific fields. In fact, the method presented here can be applied to the response of any tensor field $\boldsymbol{q}$ to a meaningful perturbative field $\boldsymbol{p}$. The interpretation of the resulting correlations can become complicated as the ranks of the tensors grow. However, given sufficient physical insight this generalized correlation measure can be a powerful tool outside of active materials. Whether applied to a high order quantum correlation or the active matter systems considered in this work, the fundamental insight of this method is to consider correlations from an internal frame of reference. Such a perspective begets meaningful response functions that describe important spatial and temporal characteristics of the fields considered.

4.4 Materials and methods

4.4.1 Active nematics and gel preparation

Experiments were performed as described previously (Zhang et al. [2021], Murrell and Gardel [2012]). Briefly, actin was polymerized in F-buffer [10 mM imidazole, 1 mM

MgCl2, 50 mM KCl, 0.2 mM egtazic acid (EGTA), pH 7.5] in the presence of 1mM ATP. To minimize photobleaching, an oxygen scavenging system (4.5 mg/mL glucose, 2.7 mg/mL glucose oxidase(cat#345486, Calbiochem, Billerica, MA), 17000 units/mL catalase (cat #02071, Sigma, St. Louis, MO) and 0.5 vol. % β-mercaptaethanol is added to the actin mixture. 0.3% w% 400 cP methylcellulose is added to this mixture to crowd actin filaments to the bottom of the sample volume. Nematic samples also included 30nM f-actin capping protein to limit filament growth while gels were uncapped. Nematic samples were driven by 100nM synthetic tetrameric motors as described in Schindler et al. [2014], while gels were driven by 50nM rabbit skeletal muscle Myosin II (Murrell and Gardel [2012]).

The sample was imaged on an Eclipse-Ti inverted microscope (Nikon, Melville, NY) in confocal mode utilizing a spinning disk (CSU-X, Yokagawa Electric, Musashino, Tokyo, Japan) and a CMOS camera (Zyla-4.2 USB 3; Andor, Belfast, UK). Nematic experiments were imaged collecting one frame every 2 seconds, while gels were imaged one frame every 5 seconds.

4.4.2 Flow field measurement

In nematics velocity fields were calculated using the method of optical flow detailed in Sun et al. [2010] using the Matlab code available at (https:// ps.is.mpg.de/code/secrets-of-optical-flow-code-for-various-methods) and the 'classic+nl-fast' method. These predictions were processed into proper units in Matlab. Velocity fields in cells were determined using Quantitative Fluorescence Speckle Microscopy, QFMS (Ji and Danuser [2005], Danuser and Waterman-Storer [2006]).

4.4.3 *Response function measurement*

Gradient of the velocity fields $\boldsymbol{\nabla u}$ is calculated using localized polynomial fitting and finite element method for the fields measured by the optical flow and QFSM respectively. The eigenvalues, λ, of the strain rate tensor, $\boldsymbol{S}_{ij}$ which is symmetric part of the $\boldsymbol{\nabla u}$, is calculated by solving the characteristic equation $|\boldsymbol{S} - \lambda \boldsymbol{I}| = 0$, and eigendirections are obtained by plugging λ in the systems of equation $\boldsymbol{S} - \lambda \boldsymbol{I} = 0$ where $\boldsymbol{I}$ is the identity tensor. For the active nematic the eigendirection associated with the positive eigenvalue and for active gel and cell data the eigendirection associated with the negative eigenvalue are chosen as direction to setup the coordinate system for ensemble averaging as described in Molaei et al. [2021]. The data measured close to the edge of the field of view is discarded to prevent error from optical flow measurement to propagate to the measured response functions. $\boldsymbol{\nabla u}$ and its decomposed components, $\boldsymbol{S}$, $\boldsymbol{\Omega}$, and $\boldsymbol{D}$ are measured over grid points with spacing large enough to prevent oversampling the data. The correlation length of these components in different systems are used to select the spacing; for example, we chose the distance where the normalized auto-correlation functions of vorticity or strain rate tensor drops to 0.5. In general, in the chaotic and noisy system the grid spacing should be smaller than grid spacing in highly coherent systems.

4.4.4 *Cell culture*

U2OS cells with NMIIA endogenously tagged with eGFP is a generous gift from Dr. Jordan Beach (Loyola University Chicago). U2OS cells were cultured in McCoy's 5A Medium (Sigma-Aldrich) supplemented with 10% FBS (Corning) and $2mM$ L-glutamine (Invitrogen).

Microscopy and live cell imaging

For the imaging of myosin dynamics in U2OS cells, Airyscan imaging was performed on a Zeiss LSM 980 microscope equipped with the Airyscan 2 detector. Images were acquired using the MPLX SR-4X mode and processed by Zen Blue 3.0 software using the Airyscan processing feature with default settings. During live cell imaging, cells were mounted on an imaging chamber (Chamlide) and maintained at 37^0C. For live cell imaging, cell medium was replaced with Dulbecco's Modified Eagle Medium (DMEM) without phenol red (Corning) supplemented with 10%FBS, $2mM$L-glutamine, 1% penicillin-streptomycin, $10mM$ HEPES and $30\mu L/mL$ Oxyrase (Oxyrase Inc.).

CHAPTER 5

MICROSCOPIC CROSSLINKING COUPLES ELASTICITY AND ACTIVITY IN A CYTOSKELETAL ACTIVE NEMATIC

5.1 Introduction

Systems composed of active agents that locally break detailed balance can exhibit striking collective behaviors that are inaccessible to assemblies that couple to energy sources in a nondirected fashion (e.g., thermally) Ramaswamy [2010], Marchetti et al. [2013]. These behaviors include collective motion, enhanced information storage, giant number fluctuations, self sorting, and phase separation Sanchez et al. [2012], del Junco et al. [2018], Kumar et al. [2019], Ramaswamy et al. [2003]. A better understanding of active systems can also inform our understanding of the interaction rules of agents in natural systems Cavagna and Giardina [2014], Dombrowski et al. [2004], Wensink et al. [2012], enable control of nonequilibrium pattern formation, and guide the design of new materials with tunable or actuatable dynamics Guillamat et al. [2016], Wu et al. [2017], Ross et al. [2019], Zhang et al. [2021,?]. One of the most well-studied classes of active materials is nematic liquid crystals Kumar et al. [2022], Zhang et al. [2021]. In nematics, elongated components (mesogens) at high densities exhibit long-ranged orientational order while maintaining translational fluidity Gennes and Prost [1993], Doostmohammadi et al. [2017]. The tendency of the mesogens to align gives the nematic an effective elasticity Marchetti et al. [2013]. The addition of activity induces distortions and flow. This competition between microscopic activity and material elasticity lies at the heart of nematic dynamics.

Nematic dynamics are characterized by their degree of disorder and the magnitude of flows which relate to the number and speed of topological defects respectively Giomi [2015]. There are various ways that one can characterize disorder in an active nematic. These include the spacing of topological defects, the correlation length of the orientation

of the mesogens (director field), the correlation length of the velocity, and the length scale of the vorticity. However, theory Giomi [2015], simulation Hemingway et al. [2016], and experiments Kumar et al. [2018], Lemma et al. [2019] suggest that these quantities all scale identically with activity—i.e., for a given set of conditions, these systems are governed by a single length scale. This length scale, ℓ, arises from the balance of the elastic stress, K/ℓ^2 where K is the elastic constant, with the active stress scale, α, such that $\ell = \sqrt{K/\alpha}$ Hemingway et al. [2016]. In turn, the magnitude of flows in a nematic can be characterized by the average flow speed, which is expected to scale as $v \sim \alpha\ell/\eta \sim \sqrt{K\alpha}/\eta$, where η is the solvent viscosity Hemingway et al. [2016].

While the dependence of nematic dynamics on mesoscopic parameters such as K and α is well-characterized, how those parameters relate to microscopic properties of the elements that make up actual nematics is not. Here we consider nematics composed of cytoskeletal elements: semiflexible filaments, molecular motors, and crosslinkers **?**. In these nematics, the molecular motors hydrolyze ATP to slide pairs of filaments, giving rise to extensile force dipoles. For the specific case of actin filaments and myosin II motors, the elastic constant was shown to depend on filament length Kumar et al. [2022]. For nematics composed of microtubules and kinesin motors, it was shown that $1/\ell^2 \sim ([\text{ATP}]/(K_m + [\text{ATP}]))^\beta$, which, given the known dependence on [ATP] of the speed of single kinesin motors walking on single filaments Verbrugge et al. [2009], is consistent with the idea that $\alpha \sim \varepsilon^\beta$, where ε is the filament strain rate induced by the motors and β is a fitting parameter Lemma et al. [2019]. However, it remains unclear whether these observations are sufficient to capture the diversity of cytoskeletal elements.

In particular, the number of steps that a molecular motor takes on a filament before detaching is an important parameter of motor proteins known as processivity. Previous studies of cytoskeletal nematics have employed motors such as kinesin and myosin II, which have high processivity—that is, they almost never detach from filaments be-

fore reaching their ends Verbrugge et al. [2009], Bloemink and Geeves [2011]. However, myosin motors range in their propensities for binding filaments, both due to the intrinsic affinities of their heads and due to their valencies Bloemink and Geeves [2011], Stam et al. [2015]. Because a motor must link a pair of filaments to generate extensile stress one would expect that differences in filament binding propensities would lead to differences in force transmission capabilities. Indeed, filament crosslinking has been observed to impact local rigidity and force transmission in other cytoskeletal contexts Stam et al. [2017].

In this work we utilize synthetic motors based on myosin XI Schindler et al. [2014] to explore how processivity affects speed and correlation length in cytoskeletal nematics. We tune processivity through both the motor valency and [ATP]. We find that nematic speed depends nonmonotonically on [ATP], reflecting opposite trends in filament strain and crosslinking with [ATP]. We find that the latter modulates the elasticity, and we introduce a simple model that accounts for the observed trends. Consistent with the model, we show that the addition of the passive crosslinker filamin also modulates elasticity and in so doing alters the energetic balance in active flows. Our results reveal a previously unappreciated connection between activity and elasticity through motor proteins and show how these quantities can be tuned independently through molecular composition.

5.2 Results

To probe how the microscopic interactions between a motor and filament control nematic structure and dynamics, we pair *in vitro* experiments with modeling. Experimentally, we can alter the availability of ATP or the number of heads in a motor—its valency—to alter processivity. Specifically we employ synthetic myosin motors that consist of the enzymatic head from Chara myosin XI which is linked via a flexible lever arm to a coiled-coil domain; we consider clusters with three, four, and eight heads (Fig. 1A) Schindler et al. [2014]. At saturating ATP the Chara myosin XI head has a duty ratio—the proportion of time it spends bound—of $\sim$0.3 Ito et al. [2007]. This low duty ratio allows motors to cycle quickly leading to high velocities but also leads to quite dramatic ATP dependent run lengths on single filaments. At 6 μm ATP, tetrameric clusters exhibit single filament velocities of 0.5 μm s^{-1} with run lengths of 3 μm, while at 500 μm ATP these motors exhibit a velocity of 10 μm s^{-1} with run lengths of 0.5 μm (Fig. S1) Schindler et al. [2014].

5.2.1 A microscopic model predicts non-monotonic nematic speed in tetrameric driven nematics.

As described above, it was previously observed for cytoskeletal nematics that $\alpha \sim \varepsilon^{\beta}$, where α is the active stress scale, ε is the filament strain rate, and β is an exponent that is expected to depend on microscopic details Lemma et al. [2019]. To understand how the activity depends on [ATP] in our system and in turn to make predictions for the nematic speed and correlation length through the relations $v \sim \sqrt{K\alpha}$ and $\ell \sim \sqrt{K/\alpha}$, we developed a microscopic model of the motors.

Our model can be viewed as a simplified version of that in Vilfan [2005]. In the model, we model the catalytic cycle of each head by three states: (1) unbound from the filament with ATP, (2) bound to the filament in the post-powerstroke state with ADP, and (3)

bound to the filament without a nucleotide (Fig. 1B). Transitions between these states are irreversible and the rate of the transition state 3 to state 1 is linearly dependent on [ATP]. The essential idea is that a head with ATP has low affinity for the filament. As a result, the transition from state 1 to state 2 occurs successfully only if the motor hydrolyzes ATP, the head quickly releases the filament once it exchanges ADP for ATP. We simulate the cycle independently for each head with the Gillespie algorithm Gillespie [1977].

In the case of a motor walking along a single filament, the heads are coupled through the coiled-coil domain position, $x(t)$. We take $x(t)$ to be a distance $s/2$ ahead of the rearmost bound head, where s is the average step length of a motor. When a head undergoes a transition from state 1 to state 2, we draw its position from the normal distribution $N(x(t) + s/2, s/2)$. When the rearmost bound head detaches, the coiled-coil domain moves forward. We scan the three rate constants (k_{12}, k_{23}, k_{31}) to identify values that yield average single-filament speeds and run lengths (i.e., the length traveled between the first time a head is bound to the last time) in agreement with measured values Schindler et al. [2014].

Given the single-filament parameterization, we model the action of a motor on a pair of antiparallel filaments, the minimal active unit in an extensile nematic Marchetti et al. [2013], Gao et al. [2015]. In this case, when a head undergoes a transition from state 1 to state 2, we choose between the filaments randomly with equal probability. The rearmost head on a given filament affects the position of the coiled-coil domain relative to that filament and in turn the positions that other heads bind that filament, but not the positions that other heads bind the other filament. We compute the filament strain rate, ε, by measuring the total movement along the two filaments and dividing by the total time that the filaments are crosslinked. We also compute the probability of crosslinking, P_{cl}, as the fraction of time that both filaments are bound simultaneously. Results for a tetrameric motor cluster are shown in Figs. 1C,D. These simulations show that P_{cl}, decreases while

ε increases with [ATP].

As described above, we use the computed strain rate to estimate the activity by $\alpha \sim \varepsilon^{\beta}$. We use $\beta = 0.1$ to account for the significant flexibility of the synthetic myosin XI motor Schindler et al. [2014] (for comparison, values ranging from 0.31 to 1.54 are considered for kinesin in Lemma et al. [2019]). Substituting the resulting α into $v \sim \sqrt{K\alpha}$ and $\ell \sim \sqrt{K/\alpha}$, we obtain an increase in v and a decrease in ℓ with [ATP], for fixed K (Fig. 1E).

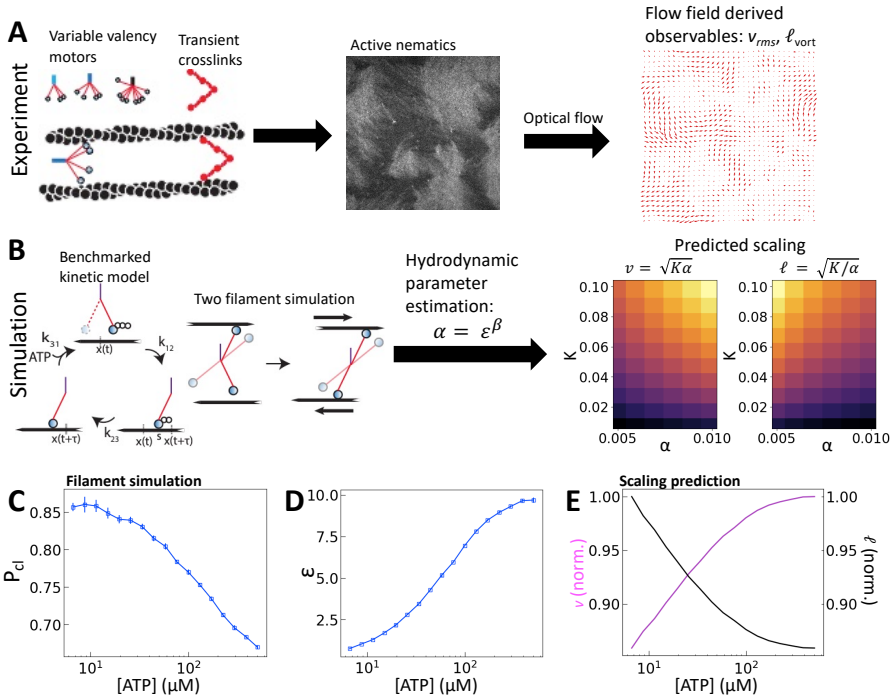

Figure 5.1: **[ATP] and activity can be related through a microscopic model.** A) Schematic of the experiments. We study synthetic motors with controlled numbers of myosin XI enzymatic heads binding to and sliding actin filaments of length 2 μm at an oil-water interface. Due to the polarized binding of the dye to actin filaments, regions with predominantly vertical orientation in the lab frame appear brighter than those oriented horizontally Kumar et al. [2022, 2018]. The experimental images are analyzed by optical flow to estimate the horizontal and vertical components of the velocity at each pixel. From the velocity field, we calculate the average flow speed, v_{rms} and average vortex radius ℓ_{vort} as in Molaei et al. [2023]. B) We model the catalytic cycle of myosin XI with three states: (1) unbound with ATP (top), (2) bound with ADP (right), and (3) bound while nucleotide free (left). Rate constants are tuned to correspond to reproduce single-filament speed and run length (Fig. S1). We extend the model to two filaments as described in the text and compute the filament extension rate, ε, and the probability of crosslinking, P_{cl}. These quantities are used to compute the nematic speed and correlation length as $v = \sqrt{K\alpha}$ and $\ell = \sqrt{K/\alpha}$, respectively. C) P_{cl} and D) ε from two-filament simulations for a cluster with four heads. E) Predicted scaling of v (magenta) and ℓ (black) for activity derived from (D) assuming constant elasticity, $K = 0.001$.

5.2.2 *Nematic elasticity depends on the probability of crosslinking.*

As noted above, we use nematics composed of short (2 μm) actin filaments labelled with tetramethylrhodamine (TMR) and synthetic motors with Chara myosin XI enzymatic heads Schindler et al. [2014] to test the predictions. We form nematics by crowding the actin filaments to a surfactant stabilized oil-water interface through depletion forces imposed by methyl-cellulose (Fig. 1A). Once the nematic is formed, we add 100 pM tetrameric motors to the sample to initiate activity. We image the sample with time-lapse fluorescence microscopy at a rate of 0.5 frames/s for 100s. Because of the polarization of TMR dye along filaments and the polarization of our excitation laser brighter (darker) patches represent filaments oriented vertically (horizontally) in the imaging plane Kumar et al. [2022, 2018]. Given the video microscopy data, we estimate the nematic velocity at each pixel using optical flow, as described in Materials and Methods (Fig. 1A) Sun et al. [2010]. Unless otherwise indicated, we plot the root mean squared velocity, v_{rms}, as a summary statistic. To quantify the length scale, we use the critical vorticity length scale, ℓ_{vort}, calculated using correlated displacement velocitometry which has been shown to equal the average vortex radius Molaei et al. [2023].

The results are shown in Fig. 2. As we expected, ℓ_{vort} decreases as [ATP] increases (Fig. 2A,C). On the other hand, v_{rms} exhibits a nonmonotonic dependence on [ATP], with a peak at 50 μm ATP (Fig. 2A,B). This behavior contrasts with the model prediction (Fig. 1E), suggesting that something is missing from the model. Given previous work in which material elasticity depends on the concentration of crosslinkers Ahmadi et al. [2006], Kruse et al. [2004], we reasoned that the elastic constant K should depend (linearly) on the effective concentration of crosslinkers, c_e:

$$K \sim K_0 + \kappa c_e \tag{5.1}$$

where K_0 is the baseline nematic elastic modulus that arises from excluded volume interactions between filaments Zhang et al. [2017], Ahmadi et al. [2006], and κ represents the energetic penalty for filament deformation at a given concentration of crosslinker. Here, because the only crosslinkers are motors, we expect $c_e = c_m P_{cl}$, where c_m is the concentration of motors. Using (5.1) for K with P_{cl} from the simulation in the scaling relations $v \sim \sqrt{K\alpha}$ and $\ell \sim \sqrt{K/\alpha}$, we obtain nonmonotonic v with decreasing ℓ with increasing [ATP] (Fig. 2D,E). Physically, there is a competition between the tendency for increased [ATP] to make the motor walk faster, resulting in a higher strain rate, and to make the motor unbind from the filament, resulting in lower P_{cl}. In the case of kinesin, the latter tendency is negligible and thus was not necessary to consider in previous studies Lemma et al. [2019].

The effect becomes more pronounced as the second term in (5.1) becomes large compared with the first (Fig. 2D). To understand this behavior mathematically, we differentiate $v = \sqrt{K\alpha}$ with respect to [ATP] and solve for the maximum by setting the resulting expression equal to zero. This yields

$$\alpha_{\text{peak}} = -\frac{K\alpha'}{K'}, \tag{5.2}$$

where α_{peak} is the activity that corresponds to the maximum velocity. For a fixed dependence of the strain rate and thus the activity on [ATP], larger κ results in larger K' and thus smaller α_{peak} (i.e., lower [ATP]). Consistent with this reasoning, the peak in Fig. 2D moves to the left as κ increases. It is also worth noting here that changes in β affect the balance in this equation as well. If we increase β, we find an ablation of peaked nematic speed similar to decreased κ. As such we set $\kappa = 10K_0$ and $\beta = 0.1$ for the rest of this work.

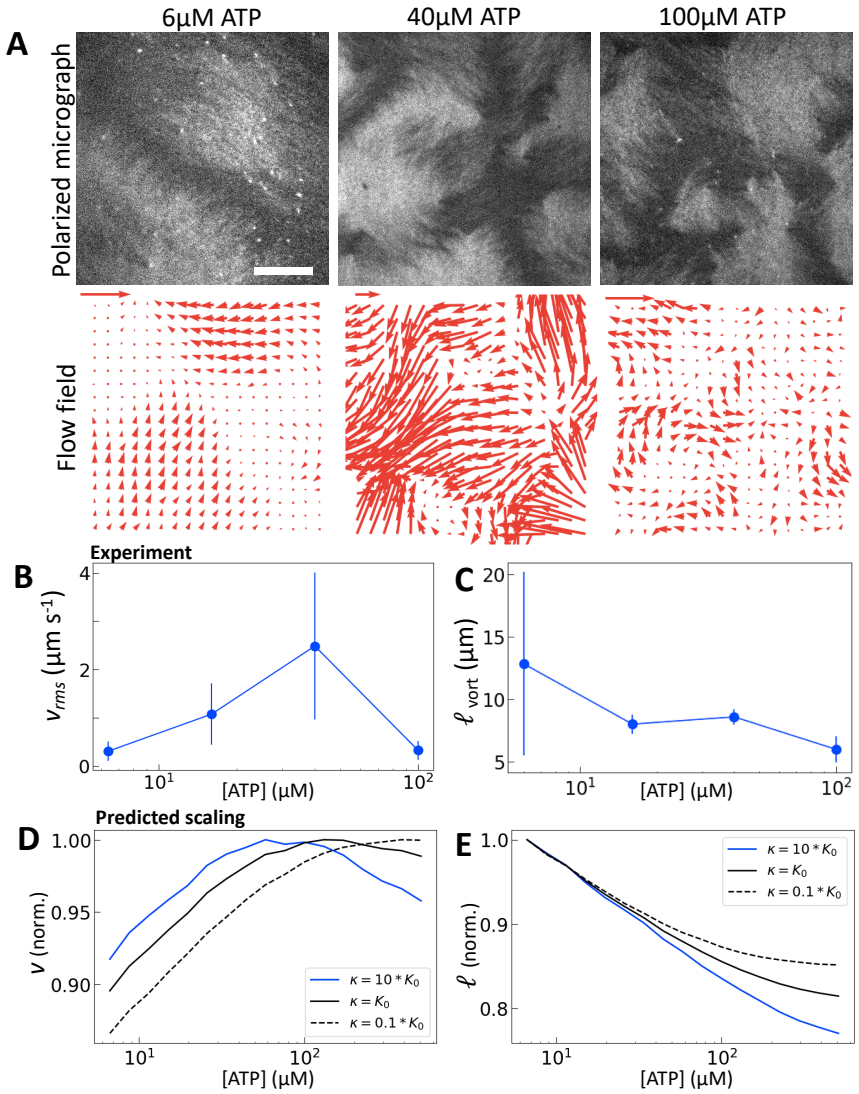

Figure 5.2: **Motor crosslinking modulates nematic elasticity.** A) Polarized fluorescence micrographs of nematics (gray scale) driven by 100pM tetrameric motor clusters from Schindler et al. [2014] containing 6, 40 or 100 μM ATP with corresponding optical flow estimated velocity fields underneath (red arrows). Scale arrows are $3\mu m/s$. B) Average flow speed v_{rms} for the full series of experiments in (A). Error bars represent the standard deviation of speed over 100s of steady state activity. C) Critical vorticity length scale ℓ_{vort} as measured in Molaei et al. [2023] for the experiments plotted in (B). D) Normalized v as a function of ATP for tetrameric motors calculated from scaling relationships with various ratios of κ to K_0. E) Normalized nematic length scale ℓ calculated as in (D). Blue curves utilize the parameters we use moving forward; $\kappa = 10K_0$ and $\beta = 0.1$.

5.2.3 *Motor valency tunes nematic dynamics.*

To understand how microscopic motor properties can tune nematic hydrodynamic parameters we turn to motor clusters with variable valencies; the number of heads in a cluster. On single filaments, increased motor valency leads to slightly reduced maximal velocity as well as dramatically increased processivity in simulation (Fig. S3). In two filament simulations, this leads to a shift in the ATP dependence of ε such that a higher ATP concentration is required to reach the same relative extension rate (Fig. 3A). Furthermore, larger cluster valencies lead to not only a greater probability of crosslinking across all ATP concentrations but a smaller relative decrease in crosslinking from low to high ATP concentrations (Fig. 3B). To see how these microscopic changes manifest at a hydrodynamic scale, we plot state spaces of v and ℓ as a function of ATP concentration and cluster valency (Fig. 3C,D). In this space, we observe a valency dependent shift in the location of maximal v with higher valencies leading to peaks at increased ATP concentrations (Fig. 3C, dotted line). Furthermore, we find a less dramatic drop off in speed after the peak as valency increases (Fig. 3C). Additionally, we observe that the relative change in ℓ between low and high ATP concentrations decreases as valency increases (Fig. 3D).

Experimentally, we utilize the control afforded by the motor's coiled-coil domain to consider clusters with $n = 3, 4$, or 8 heads. We take into account the contributions of cluster valency and total number of motor heads by considering trimeric and tetrameric motors at 100 pM and octameric motors at 50 pM (Fig. 3E). This separates the potential contributions from cluster valency and total head number in dictating dynamics. We find in these experiments that the peak of v_{rms} is indeed dependent on cluster valency and shifts rightward as valency increases (Fig. 3E). In fact, the shift we find in experiment closely matches that predicted by our model (Fig. 3C, cyan vs black dots). Furthermore, as valency increases, ℓ_{vort} at a given ATP concentration increases (Fig. 3F). These results indicate that we can tune nematic dynamics with microscopic motor properties. How-

ever, separating the contributions of P_{cl} and ε in these experiments is not possible as these quantities vary simultaneously as valency changes (Fig. 3A,B).

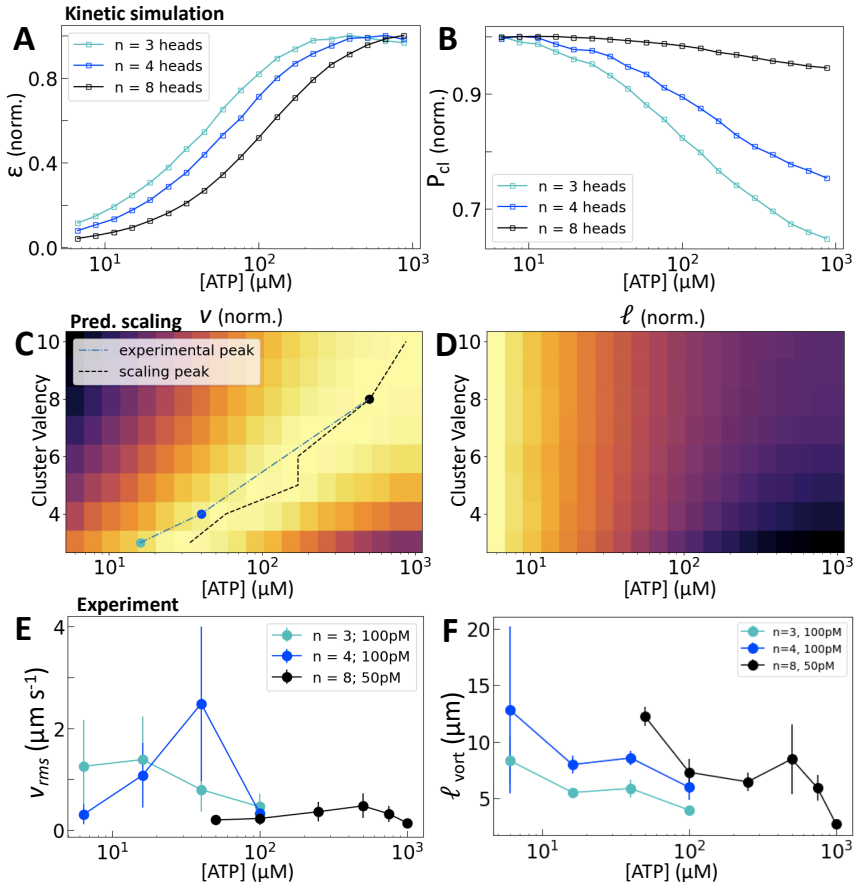

Figure 5.3: **Motor valency tunes nematic dynamics.** A) Normalized ε measured from kinetic simulation as a function of ATP concentration for clusters of variable valency. Trimers (n = 3, cyan), tetramers (n = 4, blue), or octamers (n = 8, black). B) Normalized P_{cl} for the same range of oligomers considered in (A). C) State space of normalized v from scaling predictions as a function of ATP concentration and cluster valency. Black dotted line straces the location of the peak in nematic speed. D) Normalized ℓ for the state space considered in (C). E) v_{rms} for a range of ATP concentrations and cluster valencies; n = 3 (cyan), n = 4 (blue), or n = 8 (black) measured in experiment. Colored dots in (C) correspond to peak locations here. F) ℓ_{vort} measured for the experiments in (E).

5.2.4 Crosslinking modulates the efficiency of nematic energy transfer.

To isolate the effects of crosslinking and extension rate we consider how the addition of a transient crosslinker affects nematic dynamics. Specifically, we consider the addition of the crosslinker filamin (FLN) to nematics driven by trimeric constructs as they

have the lowest baseline level of crosslinking. We consider the effects of crosslinking in our model only at the hydrodynamic scale, meaning that passive crosslinkers have no effect on the underlying ε and P_{cl} calculated from simulation (Fig. 4A). To incorporate the contributions from passive crosslinkers we simply add a contribution to the effective concentration of crosslinkers as $c_e = c_m P_{cl} + c_p$; where c_p is the concentration of passive crosslinkers. Utilizing this form and varying c_p from 0.75 to 1.5 while c_m remains 1, our scaling predicts that the addition of passive crosslinker should lead to a shift in peak location to higher ATP concentrations (Fig. 4B). This shift at first appears similar to that observed for variable cluster valency, however this shift occurs while ε and P_{cl} remain constant. Experimentally, we find that adding crosslinker to these samples yields a dramatically longer length scale as is expected from increased K (Fig. 4C,E). Furthermore, we find that increased concentrations of passive crosslinker do indeed lead to a shift in the peak v_{rms} to higher ATP concentrations (Fig. 4D,E). These shifts as a function only of passive crosslinking indicate a deep role for crosslinking and thus elasticity in determining nematic dynamics.

To see what this role is we once again consider (5.2). Recall that increasing κ resulted in greater K', shifting α_{peak} to smaller ATP concentrations. By adding crosslinker we leave K' unchanged while increasing overall K. Thus, the addition of crosslinker results in a shift of α_{peak} to higher ATP concentrations. It is interesting to note in this case that the shift occurs solely due to material changes in the nematic. These results suggest that such shifts in material properties affect how the activity supplied by motors manifests in nematic dynamics. Indeed, well characterized lattice Boltzmann simulations show that in the high activity regime total energy in the nematic actually increases with higher K (Fig. S3). This indicates a crucial role for filament crosslinking in determining the efficiency of energy transfer from motor stress into nematic motion.

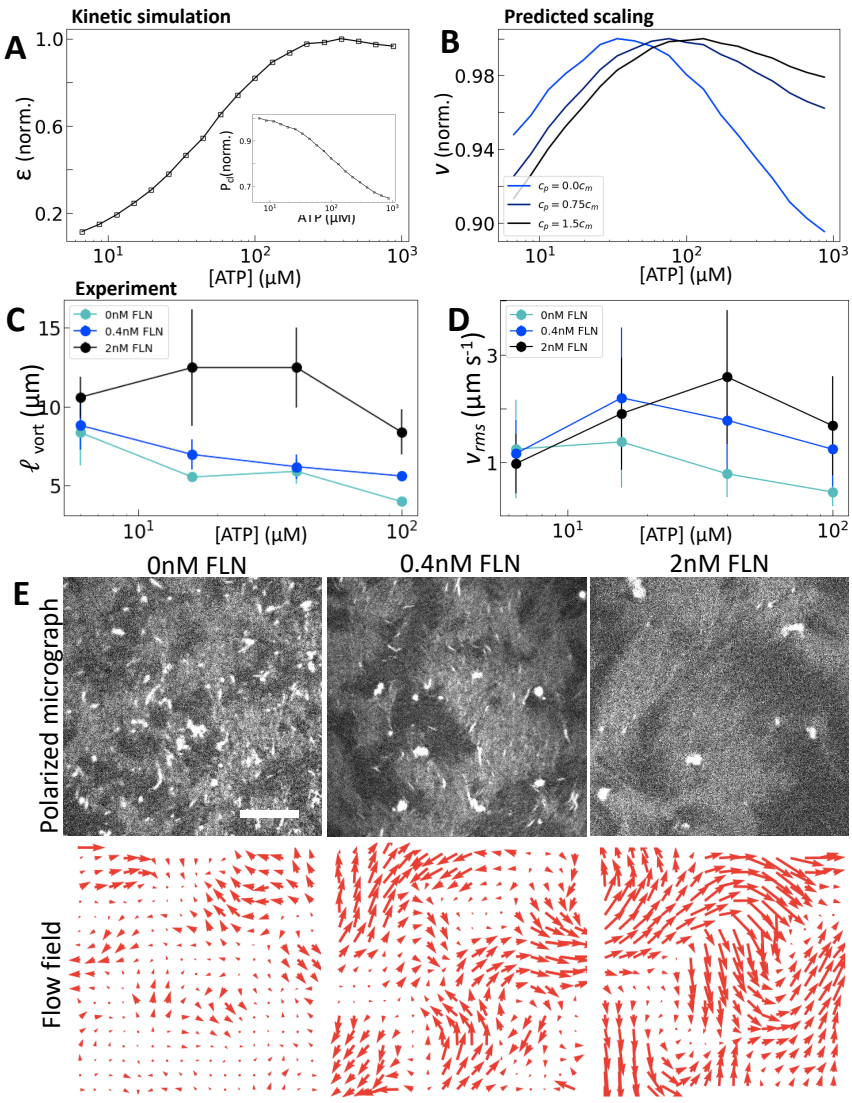

Figure 5.4: **Microscopic crosslinking alters nematic energy distribution.** A) Normalized ε and P_{cl} (inset) measured for trimeric motors in filament simulation. B) Normalized v as a function of ATP from scaling predictions incorporating $c_{ext} = 0$ (cyan), 0.008 (blue), or 0.015 (black) in the calculation of K. C) Experimental v_{rms} as a function of ATP concentration for trimeric driven nematics with 0 (cyan), 0.4 (blue), or 2 nM (black) filamin (FLN) added. D) ℓ_{vort} for the experiments in (C). E) Polarized fluorescence micrographs (gray) with corresponding flow fields below (red arrows) for trimeric driven nematics at 100 μM ATP with 0, 0.4 or 2 nM filamin (FLN) added. Scale arrow is $3\mu m s^{-1}$.

5.3 Conclusions

In this work we showed that crosslinking in cytoskeletal nematics has a profound effect on dynamics through alterations to nematic elasticity. In low processivity motors we found that reduced filament crosslinking at high ATP concentrations lead to a non-monotonic relationship between ATP concentration and nematic speed. We saw that this non-monotonicity is underpinned by large contributions of crosslinking to elasticity relative to that intrinsic to nematics through excluded volume between filaments. Furthermore we found that we could alter the precise location and degree of this non-monotonicity by changing motor valency affording us control over dynamics through tuning of motor properties. Finally we found that passive crosslinkers are able to affect changes in dynamics by altering the efficiency of energy transfer into a nematic. Together, these results underline both the importance of microscopic crosslinking to cytoskeletal nematics in particular but also the critical role of microscopic origins to mesoscale activity more generally.

One of our crucial findings in this work is the dominance of κ relative to K_0. While the precise ratio of these quantities surely depends on the microscopic properties of the nematic and the motor, the dominance of κ in this case indicates something deep about cytoskeletal nematics. Even in nematics in which crosslinking does not change between conditions—such as kinesin Verbrugge et al. [2009]—the fact that a motor must crosslink two filaments in order to generate sliding means that it always contributes in some way to elasticity. This is a fundamental interaction that lies at the heart of dynamics in these materials.

In a more general sense these results underline how hydrodynamic scaling in active materials arises from microscopic peculiarities. The fundamental interaction of nematic elasticity and filament crosslinking exists in cytoskeletal nematics because of the mechanism of activity. Other systems with varied activity mechanisms such as bacterial swarms

can be described in the hydrodynamic limit with similar nematic scaling laws. Understanding how mesoscopic behavior arises from microscopic nuances is necessary for understanding the differences between such systems and essential if we ever endeavour to tune active dynamics.

5.4 Materials and Methods

5.4.1 Experimental Procedures

Protein Purification

Monomeric actin was purified from rabbit skeletal muscle acetone powder (Sigma-Aldrich, St. Louis, MO) as described previously (Spudich and Watt [1971]) and stored in G-buffer [2mM Tris pH 8, 0.2mM ATP, 0.5mM DTT, 0.1mM CaCl2, 1mM NaN3, pH to 8]. Actin was labelled with Tetramethylrhodamine-6-maleamide (TMR; Life Technologies, Carlsbad, CA). F-Actin Capping Protein was purified as described (Burke et al. [2017]) and stored in CP buffer [10mM Tris pH 7.5, 40mM KCl, 0.5mM DTT, 0.01% NaN_3, 50% Glycerol].

Motors were a gift from the laboratory of Zev Bryant.

Assay Conditions

Actin filaments were polymerized at a 1:10 labelling ratio and a concentration of 2 μM in a 50μl polymerization mix. This mix contained 1X F-buffer [10 mM imidazole, 1 mM MgCl2, 50 mM KCl, 0.2 mM egtazic acid (EGTA), pH 7.5] with one of the various concentrations of ATP. To minimize photobleaching, an oxygen scavenging system (4.5 mg/mL glucose, 2.7 mg/mL glucose oxidase(cat#345486, Calbiochem, Billerica, MA), 17000 units/mL catalase (cat #02071, Sigma, St. Louis, MO) and 0.5 vol. % β-mercaptaethanol

is added. Actin filaments are crowded to the surface via the inclusion of 0.3% w% 400 cP methylcellulose in the polymerization mix. Capping protein is first thawed on ice, diluted to 500nM in 1X F-buffer, and then added at a final concentration of 30nM in the mix. The reaction is allowed to proceed for one hour on ice before adding to the imaging chamber.

The imaging chamber was created by first rinsing a small glass cloning cylinder (catalog no. 09-552-20, Corning Inc.) with ethanol and then attaching it to a silanated glass coverslip with two-part epoxy. To prevent the actin from sticking and maintain fluidity the coverslip is coated with a thin layer of Novec 7500 Engineered Fluid (3M, St. Paul, MN) that included PFPE-PEG-PFPE surfactant (catalog no. 008, RAN Biotechnologies, Beverly, MA) at 2% w/v before the polymerization mix is added. The mixture is allowed to sit in the sample chamber for about 30 minutes before imaging to allow for the formation of the LC.

The sample was imaged on an Eclipse-Ti inverted microscope (Nikon, Melville, NY) in confocal mode utilizing a spinning disk (CSU-X, Yokagawa Electric, Musashino, Tokyo, Japan) and a CMOS camera (Zyla-4.2 USB 3; Andor, Belfast, UK). Experiments were imaged collecting one frame every 2 seconds.

5.4.2 Data analysis

Flow fields were calculated between every two frames from time lapse images with optical flow using the 'classic+nl-fast' method Sun et al. [2010]. This method is based on the classic Horn–Schunck method which minimizes an objective function penalizing both brightness differences between start and end points (the data term) as well as enforcing smoothness in the estimated field. Flow is estimated at various spatial scales iteratively to capture first global and then local motion. The code can be found here: http:www.cs.brown.edu

Average flow speed v was calculated from the N vectors, v_i, as $v = \frac{\sum |v_i|}{N}$. Aver-

age vorticity response was calculated from flow fields using correlated displacement velocimetry as described in Molaei et al. [2023]. The code for which can be found here: https://github.com/Gardel-lab/ResponseFunction. Vorticity length scale, ℓ_{vort} was measured from this average response, U by finding the length scale at which U is maximized; $\ell_{vort} = argmax(U)$.

5.4.3 Motor Stepping Model

Walking Ansatz

We define the position of the motor cluster as the point where the n legs meet and keep track of it over time as $x(t)$. As motor heads are more likely to bind in the unstrained state, when one of the n heads h_i binds the position of the head $x_{h_i}(t)$ is drawn from $N(x(t) + \frac{S}{2}, \frac{S}{2})$ where S is the average motor step size. We assume that trailing head release is rate limiting such that upon a motor head binding or unbinding the position $x(t)$ is updated as a half step in front of the rearmost bound head; $min(x_{h_i}(t) + \frac{s}{2}$.

The catalytic cycle

We coarse grain the catalytic cycle as consisting of 3 states – unbound, ADP bound, and nucleotide free – with irreversible transitions between all states. The final unbinding rate is increased linearly with ATP concentration. To parameterize these rates we simulate a 4 headed cluster over a range of ATP concentrations and compare our simulated results to experiments performed with the same constructs from Schindler et al. [2014]. Rates are tuned by proposing a change and accepted if both the computed run length and velocity get closer to the experimental truth. The final rates we compute after 10,000 steps are $1821s^{-1}, 932s^{-1}, 6s^{-1}\mu MATP$.

The Gillespie Algorithm

Because our model for motor walking depends only on the biochemical state of the various motor heads, we will now focus on how we keep track of these states. We generalize our binding cycle for one head to n heads by simply considering n cycles that are simulated together. Because each motor head has its own cycle, the population of any given state is ever only either 1 or 0.

The Gillespie algorithm begins by calculating the overall reaction rate for every allowed transition in the next time step Gillespie [1977]. To do this we multiply the occupancy of each state by the rates for each allowed transition from that state. In this manner, because each head is simulated independently, only the transitions from the single occupied state that the motor head is in will be allowed for each head in turn. Because all other states are unoccupied by this single head, their rates will be zero after multiplication. The base rates are given as k_0 and the occupancy of the various states at time t as o_t, so for a given time the propensities are $a_t = k_0 * o_t$. The summed reaction rate is then given by

$$Y = \sum_{j=1}^{n} a_t$$

Using this total reaction rate and a pseudo-random number r_1, we calculate the time to the next reaction as

$$\tau = \frac{1}{Y} * log(\frac{1}{r_1})$$

Once a reaction time has been simulated, we must stochastically select which reaction amongst the various possibilities has occurred. To do so, we draw a second pseudo-random number r_2 and find the reaction j such that

$$\sum_{0}^{j-1} a_t < Y * r_2 < \sum_{0}^{j} a_t$$

Once a reaction j has been simulated, the simulation time is updated as $t = t + \tau$ and the state vector s_t is updated. Using this method, we can iteratively simulate stochastic transitions for the entire system of n heads.

CHAPTER 6

CONCLUSIONS

As we conclude it is important to ask what we have learned from the preceding chapters. It would be overly dramatic to say that we have made order out of chaos, however perhaps is not so far fetched to say that we found order in the chaos. We found that the spatial targeting of activity led to confined and directed flows. We found that the length of actin filaments specifically alters nematic bend elasticity leading to a novel dynamical state. We found that these chaotic states can be well described by data driven response functions. And finally, we found that the cross linking action of myosin motors intrinsically couples nematic elasticity and activity. In all these cases we were able to elucidate an important parameter, a change in which alters the dynamics in some predictable way. In this way we have not mastered the chaotic dynamics of these systems but at least reined them in. By demonstrating some degree of control over the dynamics of this specific system we have gained deeper insight into the contours of the underlying problem as a whole. Simply stated, the underlying question is this: what are the rules that govern the types of patterns that can form in a specific active system?

This is of course a question that is too big for this thesis alone. However we can begin to say something. Our results indicate that in a material with multiple deformation modes, a mismatch in the scale of these modes can lead to exotic dynamical states as energy freely passes through one mode but gets caught in the other. In our system this manifests as long lived elasticity bands that not only alter the distribution of stored elastic energy in the nematic but alter the probability distribution of defect speeds when they break. This behavior is reminiscent of recent work that showed that the softest dynamical mode in either mechanical or genetic network tends to 'absorb' variations in the system Husain and Murugan [2020]. If this same behavior holds true in active materials one might expect that the filament length change we explored in Chapter 3 would have ob-

fuscated the motor dependent elasticity we observed in Chapter 4 if the experiment had been performed in the long-filament limit. If so this would be precisely because the dynamics were already dominated by an increased bend modulus. Such a result would support one of this thesis's central findings with respect to general principles: the absolutely central role played by elasticity. In addition to filament length, the other line of evidence that supports this conclusion is the critical contribution of motor proteins to bulk material elasticity that we discovered here. It is perhaps not surprising that the mechanism of activity, or rather the mechanism of energy injection, plays a large role in character of resultant dynamical states. But, to our knowledge, it has yet to be shown precisely how various forms of activity play these different roles. The success of hydrodynamic descriptions combined with the difficulty of simulating multi-scale phenomena has left the field to merely muse at what different activity modalities might do. By demonstrating the inextricable link that myosin motors form between liquid crystal elasticity and the activity produced therein, we can begin to untangle how active modalities contribute to dynamical states. One could easily imagine that a polar activity could produce a dynamical state discernably different from that produced in a nematic if we knew where to look.

Beyond simply enumerating the rules that dictate the dynamics we observe, a major role of the work described here is to advance the quantification of these dynamics. At the outset of our work a number of disparate and specific methods were used to quantify length and timescales in active materials. While these descriptions certainly moved the field quite far, they lacked the completeness required to truly utilize them to compare between systems. The method we introduced in chapter four goes a long way towards gaining a complete understanding of active materials. By casting well known correlation analysis in terms of response functions we were able to wring more information out of these easily accessible experimental fields than anyone before. This allowed us distinguish compressible and incompressible active systems. It allowed us to distinguish be-

tween viscus and viscoelastic relaxation dynamics. We were even able to discern distinct modes of contractility inside of live cells. This new method promises to provide the field a much more complete description of complex active dynamics than before in a compact set of measurements. The ability to determine material properties as well as dynamical quantities lends these response functions broad applicability across not only known but also understudied systems. When trying to answer the big question we proposed earlier it will serve researchers well to understand how all of the different material and dynamical modes change as one switches from cross linking to, for example, polar driven active materials. By making the code readily available and describing the method as well as we possibly can, we hope that one of the lasting legacies of the work presented here will be the utilization of this fantastic tool in some of the important work to come in the field.

Looking forward there are many outstanding questions in the field but a few warrant specific enumeration. It has been noted many times before that biology is chiral. There has been paucity of work however into the manifestations of chiral phenomena in biological active systems. Unpublished work indicates that consistent symmetry breaking does occur in certain assemblies of actin and myosin. A deeper dive and more thorough understanding of how chiral structural components or chiral motors affect active flows would be fruitful avenue of investigation. Recent experiments in the field have demonstrated the beautiful phenomena that occur in three-dimensional active nematics Duclos et al. [2020]. This builds the great deal of intuition we have collectively built up from the study of two-dimensional active nematics. There is however an intermediate zone that warrants investigation. Recent work in development and cell biology has indicated a role for topological defects in the control and establishment of biological patterns. These patterns are oftentimes associated with behaviors that are emergently out of plane Copenhagen et al. [2021]. Some work has been done investigating how these out of plane behaviors emerge from a two-dimensional active material. However there is much more room to move in

this arena examining precisely what types of dynamics arise in a three-dimensional system with one definitively smaller dimension. We could imagine a situation arising similar to that which occurs in Chapter 2 where one deformation mode is significantly more energy intensive than others. Such a mismatch could lead to behavior that significantly diverges from bulk three-dimensional behavior and perhaps helps to explain the role of such nearly two dimensional systems in biology. While there are many outstanding questions, that is always the case in science. We hope that the tools we developed and the insights that we have gained may help future scientists at least a little bit as they continue to untangle the mysteries of active systems.

REFERENCES

R. Aditi Simha and Sriram Ramaswamy. Hydrodynamic Fluctuations and Instabilities in Ordered Suspensions of Self-Propelled Particles. *Phys. Rev. Lett.*, 89(5):058101, July 2002. doi:10.1103/PhysRevLett.89.058101. URL https://link.aps.org/doi/10.1103/PhysRevLett.89.058101. Publisher: American Physical Society.

Aphrodite Ahmadi, M. C. Marchetti, and T. B. Liverpool. Hydrodynamics of isotropic and liquid crystalline active polymer solutions. *Physical Review E*, 74(6):061913, December 2006. doi:10.1103/PhysRevE.74.061913. URL https://link.aps.org/doi/10.1103/PhysRevE.74.061913. Publisher: American Physical Society.

Bruce Alberts, Alexander Johnson, Julian Lewis, Martin Raff, Keith Roberts, and Peter Walter. *Molecular Biology of the Cell*. Garland Science, 4th edition, 2002. ISBN 978-0-8153-3218-3 978-0-8153-4072-0.

Ricard Alert, Jean-François Joanny, and Jaume Casademunt. Universal scaling of active nematic turbulence. *Nature Physics*, 16(6):682–688, June 2020. ISSN 1745-2473, 1745-2481. doi:10.1038/s41567-020-0854-4. URL http://www.nature.com/articles/s41567-020-0854-4.

Ricard Alert, Jaume Casademunt, and Jean-François Joanny. Active Turbulence. *Annual Review of Condensed Matter Physics*, 13:143–170, March 2022. doi:10.1146/annurev-conmatphys-082321-035957.

Jason Alicea, Leon Balents, Matthew P. A. Fisher, Arun Paramekanti, and Leo Radzihovsky. Transition to zero resistance in a two-dimensional electron gas driven with microwaves. *Phys. Rev. B*, 71(23):235322, June 2005. doi:10.1103/PhysRevB.71.235322. URL https://link.aps.org/doi/10.1103/PhysRevB.71.235322. Publisher: American Physical Society.

Debarghya Banerjee, Anton Souslov, and Vincenzo Vitelli. Hydrodynamic correlation functions of chiral active fluids. *Physical Review Fluids*, 7(4):043301, April 2022. doi:10.1103/PhysRevFluids.7.043301. URL https://link.aps.org/doi/10.1103/PhysRevFluids.7.043301.

Victor Bapst, T Keck, A. Grabska-Barwińska, C Donner, E D Cubuk, S S Schoenholz, A. Obika, A. W. R. Nelson, T. Back, D. Hassabis, and P. Kohli. Unveiling the predictive power of static structure in glassy systems. *Nature Physics*, 16(4):448–454, 2020. ISSN 1745-2473. doi:10.1038/s41567-020-0842-8. URL http://dx.doi.org/10.1038/s41567-020-0842-8%0Ahttp://www.nature.com/articles/s41567-020-0842-8.

Yohai Bar-Sinai, Stephan Hoyer, Jason Hickey, and Michael P. Brenner. Learning data-driven discretizations for partial differential equations. *Proceedings of the National Academy of Sciences of the United States of America*, 116(31):15344–15349, 2019. ISSN 10916490. doi:10.1073/pnas.1814058116.

G. K. Batchelor. *An Introduction to Fluid Dynamics*. Cambridge Mathematical Library. Cambridge University Press, Cambridge, 2000. ISBN 978-0-521-66396-0. doi:10.1017/CBO9780511800955. URL https://www.cambridge.org/core/books/an-introduction-to-fluid-dynamics/18AA1576B9C579CE25621E80F9266993.

Christopher Battle, Chase P Broedersz, Nikta Fakhri, Veikko F Geyer, Jonathon Howard, Christoph F Schmidt, and Fred C MacKintosh. Broken detailed balance at mesoscopic scales in active biological systems. *Science*, 352(6285):604–607, 2016. Publisher: American Association for the Advancement of Science.

Antony N. Beris and Brian J. Edwards. *Thermodynamics of Flowing Systems with Internal Microstructure*. Oxford University Press, Inc., New York and Oxford, 1994.

Laurent Blanchoin, Rajaa Boujemaa-Paterski, Cécile Sykes, and Julie Plastino. Actin dynamics, architecture, and mechanics in cell motility. *Physiological reviews*, 94(1):235–263, 2014. Publisher: Am Physiological Soc.

Marieke J Bloemink and Michael A Geeves. Shaking the myosin family tree: biochemical kinetics defines four types of myosin motor. In *Seminars in cell & developmental biology*, volume 22, pages 961–967. Elsevier, 2011. Issue: 9.

Antoine Bricard, Jean-Baptiste Caussin, Nicolas Desreumaux, Olivier Dauchot, and Denis Bartolo. Emergence of macroscopic directed motion in populations of motile colloids. *Nature*, 503(7474):95–98, 2013. Publisher: Nature Publishing Group.

Chase P Broedersz and Fred C MacKintosh. Modeling semiflexible polymer networks. *Reviews of Modern Physics*, 86(3):995, 2014. Publisher: APS.

J. Buhl, D. J. T. Sumpter, I. D. Couzin, J. J. Hale, E. Despland, E. R. Miller, and S. J. Simpson. From Disorder to Order in Marching Locusts. *Science*, 312(5778):1402–1406, 2006.

Thomas A Burke, Alyssa J Harker, Roberto Dominguez, and David R Kovar. The bacterial virulence factors VopL and VopF nucleate actin from the pointed end. *Journal of Cell Biology*, 216(5):1267–1276, 2017. Publisher: The Rockefeller University Press.

Stanislav Burov, SM Ali Tabei, Toan Huynh, Michael P Murrell, Louis H Philipson, Stuart A Rice, Margaret L Gardel, Norbert F Scherer, and Aaron R Dinner. Distribution of directional change as a signature of complex dynamics. *Proceedings of the National Academy of Sciences*, 110(49):19689–19694, 2013. Publisher: National Acad Sciences.

Giuseppe Carleo, Ignacio Cirac, Kyle Cranmer, Laurent Daudet, Maria Schuld, Naftali Tishby, Leslie Vogt-Maranto, and Lenka Zdeborová. Machine learning and the physical sciences. *Reviews of Modern Physics*, 91(4):45002, 2019. ISSN 15390756. doi:10.1103/RevModPhys.91.045002. URL https://doi.org/10.1103/RevModPhys.91.045002. Publisher: American Physical Society.

Juan Carrasquilla and Roger G. Melko. Machine learning phases of matter. *Nature Physics*, 13(5):431–434, 2017. ISSN 17452481. doi:10.1038/nphys4035.

Mirco Castoldi and Andrei V. Popov. Purification of brain tubulin through two cycles of polymerization–depolymerization in a high-molarity buffer. *Protein Expression and Purification*, 32(1):83 – 88, 2003.

Michael E. Cates and Julien Tailleur. Motility-Induced Phase Separation. *Annual Review of Condensed Matter Physics*, 6(1):219–244, 2015. doi:10.1146/annurev-conmatphys-031214-014710.

Andrea Cavagna and Irene Giardina. Bird Flocks as Condensed Matter. *Annual Review of Condensed Matter Physics*, 5(1):183–207, March 2014. ISSN 1947-5454, 1947-5462. doi:10.1146/annurev-conmatphys-031113-133834. URL https://www.annualreviews.org/doi/10.1146/annurev-conmatphys-031113-133834.

P. M. Chaikin and T. C. Lubensky. *Principles of Condensed Matter Physics*. Cambridge University Press, 1995. doi:10.1017/cbo9780511813467. Publication Title: Principles of Condensed Matter Physics.

Pooja Chandrakar, Minu Varghese, S Ali Aghvami, Aparna Baskaran, Zvonimir Dogic, and Guillaume Duclos. Confinement controls the bend instability of three-dimensional active liquid crystals. *Physical Review Letters*, 125(25):257801, 2020. Publisher: APS.

Nicholas G. Chisholm and Kathleen J. Stebe. Driven and active colloids at fluid interfaces. *Journal of Fluid Mechanics*, 914:A29, May 2021. ISSN 0022-1120, 1469-7645. doi:10.1017/jfm.2020.708. URL https://www.cambridge.org/core/journals/journal-of-fluid-mechanics/article/driven-and-active-colloids-at-fluid-interfaces/33AAD708E7F252F276C3DB090FA036BE. Publisher: Cambridge University Press.

Luca Cipelletti, S. Manley, R. C. Ball, and D. A. Weitz. Universal Aging Features in the Restructuring of Fractal Colloidal Gels. *Physical Review Letters*, 84(10):2275–2278, March 2000. doi:10.1103/PhysRevLett.84.2275. URL https://link.aps.org/doi/10.1103/PhysRevLett.84.2275. Publisher: American Physical Society.

Jonathan Colen, Ming Han, Rui Zhang, Steven A. Redford, Linnea M. Lemma, Link Morgan, Paul V. Ruijgrok, Raymond Adkins, Zev Bryant, Zvonimir Dogic, Margaret L. Gardel, Juan J. de Pablo, and Vincenzo Vitelli. Machine learning active-nematic hydrodynamics. *Proceedings of the National Academy of Sciences*, 118(10):e2016708118, March 2021. doi:10.1073/pnas.2016708118. URL https://www.pnas.org/doi/abs/10.1073/pnas.2016708118.

Katherine Copenhagen, Ricard Alert, Ned S. Wingreen, and Joshua W. Shaevitz. Topological defects promote layer formation in Myxococcus xanthus colonies. *Nature Physics*, 17(2):211–215, February 2021. ISSN 1745-2481. doi:10.1038/s41567-020-01056-4. URL https://www.nature.com/articles/s41567-020-01056-4. Number: 2 Publisher: Nature Publishing Group.

E. D. Cubuk, S. S. Schoenholz, J. M. Rieser, B. D. Malone, J. Rottler, D. J. Durian, E. Kaxiras, and A. J. Liu. Identifying structural flow defects in disordered solids using

machine-learning methods. *Physical Review Letters*, 114(10):1–5, 2015. ISSN 10797114. doi:10.1103/PhysRevLett.114.108001.

E. D. Cubuk, R. J. S. Ivancic, S. S. Schoenholz, D. J. Strickland, A. Basu, Z. S. Davidson, J. Fontaine, J. L. Hor, Y.-R. Huang, Y. Jiang, N. C. Keim, K. D. Koshigan, J. A. Lefever, T. Liu, X.-G. Ma, D. J. Magagnosc, E. Morrow, C. P. Ortiz, J. M. Rieser, A. Shavit, T. Still, Y. Xu, Y. Zhang, K. N. Nordstrom, P. E. Arratia, R. W. Carpick, D. J. Durian, Z. Fakhraai, D. J. Jerolmack, Daeyeon Lee, Ju Li, R. Riggleman, K. T. Turner, A. G. Yodh, D. S. Gianola, and Andrea J. Liu. Structure-property relationships from universal signatures of plasticity in disordered solids. *Science*, 358(6366):1033–1037, 2017. doi:10.1126/science.aai8830. URL `https://science.sciencemag.org/content/358/6366/1033`. Publisher: American Association for the Advancement of Science.

Gaudenz Danuser and Clare M. Waterman-Storer. Quantitative Fluorescent Speckle Microscopy of Cytoskeleton Dynamics. *Annual Review of Biophysics and Biomolecular Structure*, 35(1):361–387, 2006. doi:10.1146/annurev.biophys.35.040405.102114. URL `https://doi.org/10.1146/annurev.biophys.35.040405.102114`. _eprint: https://doi.org/10.1146/annurev.biophys.35.040405.102114.

Stephen J DeCamp, Gabriel S Redner, Aparna Baskaran, Michael F Hagan, and Zvonimir Dogic. Orientational order of motile defects in active nematics. *Nature materials*, 14(11): 1110–1115, 2015. Publisher: Nature Publishing Group.

Clara del Junco, Laura Tociu, and Suriyanarayanan Vaikuntanathan. Energy dissipation and fluctuations in a driven liquid. *Proceedings of the National Academy of Sciences*, 115 (14):3569–3574, April 2018. doi:10.1073/pnas.1713573115. URL `https://www.pnas.org/doi/abs/10.1073/pnas.1713573115`. Publisher: Proceedings of the National Academy of Sciences.

C. Denniston, D. Marenduzzo, E. Orlandini, and J. M. Yeomans. Lattice Boltzmann algorithm for three-dimensional liquid-crystal hydrodynamics. *Philosophical Transactions of the Royal Society A: Mathematical, Physical and Engineering Sciences*, 362(1821):1745–1754, 2004a. ISSN 1364503X. doi:10.1098/rsta.2004.1416.

C. Denniston, D. Marenduzzo, E. Orlandini, and J. M. Yeomans. Lattice Boltzmann algorithm for three–dimensional liquid–crystal hydrodynamics. *Philosophical Transactions of the Royal Society of London. Series A: Mathematical, Physical and Engineering Sciences*, 362 (1821):1745–1754, 2004b. Publisher: The Royal Society.

Colin Denniston, Enzo Orlandini, and J. M. Yeomans. Lattice Boltzmann simulations of liquid crystal hydrodynamics. *Physical Review E - Statistical Physics, Plasmas, Fluids, and Related Interdisciplinary Topics*, 63(5):1–10, 2001a. ISSN 1063651X. doi:10.1103/PhysRevE.63.056702.

Colin Denniston, Enzo Orlandini, and J. M. Yeomans. Lattice Boltzmann simulations of liquid crystal hydrodynamics. *Physical Review E*, 63(5):056702, 2001b. Publisher: APS.

Julien Deseigne, Olivier Dauchot, and Hugues Chaté. Collective Motion of Vibrated Polar Disks. *Phys. Rev. Lett.*, 105(9):098001, 2014.

Hideo Doi, Kazuaki Z. Takahashi, Kenji Tagashira, Jun ichi Fukuda, and Takeshi Aoyagi. Machine learning-aided analysis for complex local structure of liquid crystal polymers. *Scientific Reports*, 9(1):1–12, 2019. ISSN 20452322. doi:10.1038/s41598-019-51238-1. URL `http://dx.doi.org/10.1038/s41598-019-51238-1`. ISBN: 4159801951 Publisher: Springer US.

Christopher Dombrowski, Luis Cisneros, Sunita Chatkaew, Raymond E. Goldstein, and John O. Kessler. Self-Concentration and Large-Scale Coherence in Bacterial Dynamics. *Physical Review Letters*, 93(9):098103, August 2004. doi:10.1103/PhysRevLett.93.098103. URL `https://link.aps.org/doi/10.1103/PhysRevLett.93.098103`.

Amin Doostmohammadi, Michael F. Adamer, Sumesh P. Thampi, and Julia M. Yeomans. Stabilization of active matter by flow-vortex lattices and defect ordering. *Nat. Commun.*, 7:10557, 2016.

Amin Doostmohammadi, Tyler N. Shendruk, Kristian Thijssen, and Julia M. Yeomans. Onset of meso-scale turbulence in active nematics. *Nature Communications*, 8(15326), 2017.

Amin Doostmohammadi, Jordi Ignés-Mullol, Julia M. Yeomans, and Francesc Sagués. Active nematics. *Nature Communications*, 9(1):3246, August 2018. ISSN 2041-1723. doi:10.1038/s41467-018-05666-8. URL `http://www.nature.com/articles/s41467-018-05666-8`. Number: 1 Publisher: Nature Publishing Group.

G Duclos, C Blanch-Mercader, V Yashunsky, G Salbreux, J-F Joanny, J Prost, and Pascal Silberzan. Spontaneous shear flow in confined cellular nematics. *Nature physics*, 14(7): 728–732, 2018. Publisher: Nature Publishing Group.

Guillaume Duclos, Christoph Erlenkämper, Jean François Joanny, and Pascal Silberzan. Topological defects in confined populations of spindle-shaped cells. *Nature Physics*, 13 (1):58–62, 2017. doi:10.1038/nphys3876.

Guillaume Duclos, Raymond Adkins, Debarghya Banerjee, Matthew S.E. Peterson, Minu Varghese, Itamar Kolvin, Arvind Baskaran, Robert A. Pelcovits, Thomas R. Powers, Aparna Baskaran, Federico Toschi, Michael F. Hagan, Sebastian J. Streichan, Vincenzo Vitelli, Daniel A. Beller, and Zvonimir Dogic. Topological structure and dynamics of three-dimensional active nematics. *Science*, 367(6482):1120–1124, 2020. ISSN 10959203. doi:10.1126/science.aba1136.

Karthik Duraisamy, Gianluca Iaccarino, and Heng Xiao. Turbulence Modeling in the Age of Data. *Annual Review of Fluid Mechanics*, 51(1):357–377, 2019. ISSN 0066-4189. doi:10.1146/annurev-fluid-010518-040547.

Perry W. Ellis, Daniel J.G. Pearce, Ya Wen Chang, Guillermo Goldsztein, Luca Giomi, and Alberto Fernandez-Nieves. Curvature-induced defect unbinding and dynamics in active nematic toroids. *Nature Physics*, 14(1):85–90, 2018. ISSN 17452481. doi:10.1038/NPHYS4276.

M. Cristina Marchetti Ewan J. Hemingway, Prashant Mishra and Suzanne M. Fielding. Correlation lengths in hydrodynamic models of active nematics. *Soft Matter*, 12:7943, 2016.

Étienne Fodor, Cesare Nardini, Michael E. Cates, Julien Tailleur, Paolo Visco, and Frédéric van Wijland. How Far from Equilibrium Is Active Matter? *Phys. Rev. Lett.*, 117(3): 038103, July 2016. doi:10.1103/PhysRevLett.117.038103. URL `https://link.aps.org/doi/10.1103/PhysRevLett.117.038103`. Publisher: American Physical Society.

Eva Forgacs, Suzanne Cartwright, Takeshi Sakamoto, James R Sellers, John ET Corrie, Martin R Webb, and Howard D White. Kinetics of ADP dissociation from the trail and lead heads of actomyosin V following the power stroke. *Journal of Biological Chemistry*, 283(2):766–773, 2008. Publisher: ASBMB.

Dieter Forster. *Hydrodynamic Fluctuations, Broken Symmetry, and Correlation Functions*. CRC Press, 1 edition, March 2018. ISBN 978-0-429-49368-3. doi:10.1201/9780429493683. URL `https://www.taylorfrancis.com/books/9780429962233`.

Peter J Foster, Sebastian Fürthauer, Michael J Shelley, and Daniel J Needleman. Active contraction of microtubule networks. *eLife*, 4:e10837, 2015.

J. Fournier and P. Galatola. Modeling planar degenerate wetting and anchoring in nematic liquid crystals. *Europhys Lett.*, 72(3):403, January 2005.

Jun-ichi Fukuda, Hiroshi Yokoyama, Makoto Yoneya, and Holger Stark. Interaction between Particles in a Nematic Liquid Crystal: Numerical Study Using the Landau-de Gennes Continuum Theory. *Mol. Cryst. Liq. Cryst.*, 435:63–74, 2005.

Tong Gao, Robert Blackwell, Matthew A. Glaser, M.D. Betterton, and Michael J. Shelley. Multiscale Polar Theory of Microtubule and Motor-Protein Assemblies. *Physical Review Letters*, 114(4):048101, January 2015. doi:10.1103/PhysRevLett.114.048101. URL `https://link.aps.org/doi/10.1103/PhysRevLett.114.048101`. Publisher: American Physical Society.

M. L. Gardel, J. H. Shin, F. C. MacKintosh, L. Mahadevan, P. Matsudaira, and D. A. Weitz. Elastic Behavior of Cross-Linked and Bundled Actin Networks. *Science*, 304(5675):1301–1305, May 2004. doi:10.1126/science.1095087. URL `https://www.science.org/doi/full/10.1126/science.1095087`. Publisher: American Association for the Advancement of Science.

Margaret L. Gardel, Benedikt Sabass, Lin Ji, Gaudenz Danuser, Ulrich S. Schwarz, and Clare M. Waterman. Traction stress in focal adhesions correlates biphasically with actin

retrograde flow speed. *Journal of Cell Biology*, 183(6):999–1005, December 2008. ISSN 0021-9525. doi:10.1083/jcb.200810060. URL https://doi.org/10.1083/jcb.200810060.

P. G. de Gennes and J. Prost. *The Physics of Liquid Crystals*. Clarendon Press, 1993. ISBN 978-0-19-851785-6.

Daniel T Gillespie. Exact stochastic simulation of coupled chemical reactions. *The journal of physical chemistry*, 81(25):2340–2361, 1977. Publisher: ACS Publications.

Luca Giomi. Active nematics. *Phys. Rev. Lett.*, 2013.

Luca Giomi. Geometry and Topology of Turbulence in Active Nematics. *Physical Review X*, 5(3):031003, July 2015. doi:10.1103/PhysRevX.5.031003. URL https://link.aps.org/doi/10.1103/PhysRevX.5.031003. Publisher: American Physical Society.

Luca Giomi, Mark J. Bowick, Xu Ma, and M. Cristina Marchetti. Defect annihilation and proliferation in active Nematics. *Physical Review Letters*, 110(22):1–5, 2013. ISSN 00319007. doi:10.1103/PhysRevLett.110.228101.

Luca Giomi, Mark J Bowick, Prashant Mishra, Rastko Sknepnek, and M Cristina Marchetti. Defect dynamics in active nematics. *Philosophical Transactions of the Royal Society A: Mathematical, Physical and Engineering Sciences*, 372(2029): 20130365, November 2014. ISSN 1364-503X, 1471-2962. doi:10.1098/rsta.2013.0365. URL https://royalsocietypublishing.org/doi/10.1098/rsta.2013.0365.

Luca Giomi, Žiga Kos, Miha Ravnik, and Anupam Sengupta. Cross-talk between topological defects in different fields revealed by nematic microfluidics. *Proceedings of the National Academy of Sciences*, 114(29):E5771–E5777, 2017. Publisher: National Acad Sciences.

Ian Goodfellow, Jean Pouget-Abadie, Mehdi Mirza, Bing Xu, David Warde-Farley, Sherjil Ozair, Aaron Courville, and Yoshua Bengio. Generative Adversarial Nets. *Proceedings of the International Conference on Neural Information Processing Systems (NIPS)*, pages 2672–2680, 2014. doi:10.1109/ICCVW.2019.00369. ISBN: 9781728150239.

Richard Green, John Toner, and Vincenzo Vitelli. Geometry of thresholdless active flow in nematic microfluidics. *Phys. Rev. Fluids*, 2(10):104201, October 2017. doi:10.1103/PhysRevFluids.2.104201. URL https://link.aps.org/doi/10.1103/PhysRevFluids.2.104201. Publisher: American Physical Society.

P. Guillamat, J. Ignés-Mullol, and F. Sagués. Taming active turbulence with patterned soft interfaces. *Nature Communications*, 8(1):564, September 2017. ISSN 2041-1723. doi:10.1038/s41467-017-00617-1. URL https://www.nature.com/articles/s41467-017-00617-1. Number: 1 Publisher: Nature Publishing Group.

Pau Guillamat, Jordi Ignés-Mullol, and Francesc Sagués. Control of active liquid crystals with a magnetic field. *Proceedings of the National Academy of Sciences of the United States of America*, 113(20):5498–5502, 2016. ISSN 10916490. doi:10.1073/pnas.1600339113.

Zhaoli Guo and Chang Shu. *Lattice Boltzmann Method and its Applications in Engineering*. 2013. ISBN 978-981-4508-29-2. Publication Title: World Scientific.

Zhaoli Guo, Chuguang Zheng, and Baochang Shi. Discrete lattice effects on the forcing term in the lattice Boltzmann method. *Physical Review E - Statistical Physics, Plasmas, Fluids, and Related Interdisciplinary Topics*, 65(4):6, 2002a. ISSN 1063651X. doi:10.1103/PhysRevE.65.046308.

Zhaoli Guo, Chuguang Zheng, and Baochang Shi. Discrete lattice effects on the forcing term in the lattice Boltzmann method. *Physical review E*, 65(4):046308, 2002b. Publisher: APS.

Jérôme Hardoüin, Rian Hughes, Amin Doostmohammadi, Justine Laurent, Teresa Lopez-Leon, Julia M. Yeomans, Jordi Ignés-Mullol, and Francesc Sagués. Reconfigurable flows and defect landscape of confined active nematics. *Communications Physics*, 2(1):1–9, 2019. doi:10.1038/s42005-019-0221-x.

Yashodhan Hatwalne, Sriram Ramaswamy, Madan Rao, and R. Aditi Simha. Rheology of Active-Particle Suspensions. *Phys. Rev. Lett.*, 92(11):118101, March 2004. doi:10.1103/PhysRevLett.92.118101. URL `https://link.aps.org/doi/10.1103/PhysRevLett.92.118101`. Publisher: American Physical Society.

Kaiming He, Xiangyu Zhang, Shaoqing Ren, and Jian Sun. Deep Residual Learning for Image Recognition. *CoRR*, abs/1512.03385, 2015. URL `http://arxiv.org/abs/1512.03385`. _eprint: 1512.03385.

Ewan J. Hemingway, Prashant Mishra, M. Cristina Marchetti, and Suzanne M. Fielding. Correlation lengths in hydrodynamic models of active nematics. *Soft Matter*, 12(38): 7943–7952, 2016. ISSN 17446848. doi:10.1039/c6sm00812g. Publisher: Royal Society of Chemistry.

Pirta Hotulainen and Pekka Lappalainen. Stress fibers are generated by two distinct actin assembly mechanisms in motile cells. *Journal of Cell Biology*, 173(3):383–394, May 2006. ISSN 0021-9525. doi:10.1083/jcb.200511093. URL `https://doi.org/10.1083/jcb.200511093`.

Steven D Hudson and Edwin L Thomas. Frank elastic-constant anisotropy measured from transmission-electron-microscope images of disclinations. *Physical Review Letters*, 62(17):1993, 1989. Publisher: APS.

Kabir Husain and Arvind Murugan. Physical Constraints on Epistasis. *Molecular Biology and Evolution*, 37(10):2865–2874, October 2020. ISSN 0737-4038, 1537-1719. doi:10.1093/molbev/msaa124. URL `https://academic.oup.com/mbe/article/37/10/2865/5839750`.

Anthony Hyman, David Drechsel, Doug Kellogg, Steve Salser, Ken Sawin, Pam Steffen, Linda Wordeman, and Tim Mitchison. Preparation of modified tubulins. In *Molecular Motors and the Cytoskeleton*, volume 196 of *Methods in Enzymology*, pages 478 – 485. Academic Press, 1991. doi:https://doi.org/10.1016/0076-6879(91)96041-O. ISSN: 0076-6879.

Kohji Ito, Mitsuo Ikebe, Taku Kashiyama, Toshifumi Mogami, Takahide Kon, and Keiichi Yamamoto. Kinetic mechanism of the fastest motor protein, Chara myosin. *Journal of Biological Chemistry*, 282(27):19534–19545, 2007. Publisher: ASBMB.

Kohji Ito, Yukie Yamaguchi, Kenji Yanase, Yousuke Ichikawa, and Keiichi Yamamoto. Unique charge distribution in surface loops confers high velocity on the fast motor protein Chara myosin. *Proceedings of the National Academy of Sciences*, 106(51):21585–21590, December 2009. doi:10.1073/pnas.0910787106. URL https://www.pnas.org/doi/abs/10.1073/pnas.0910787106. Publisher: Proceedings of the National Academy of Sciences.

Ewan J. Hemingway, Prashant Mishra, M. Cristina Marchetti, and Suzanne M. Fielding. Correlation lengths in hydrodynamic models of active nematics. *Soft Matter*, 12(38): 7943–7952, 2016. doi:10.1039/C6SM00812G. URL https://pubs.rsc.org/en/content/articlelanding/2016/sm/c6sm00812g.

L. Ji and G. Danuser. Tracking quasi-stationary flow of weak fluorescent signals by adaptive multi-frame correlation. *Journal of Microscopy*, 220(3):150–167, 2005. ISSN 1365-2818. doi:10.1111/j.1365-2818.2005.01522.x. URL https://onlinelibrary.wiley.com/doi/abs/10.1111/j.1365-2818.2005.01522.x. _eprint: https://onlinelibrary.wiley.com/doi/pdf/10.1111/j.1365-2818.2005.01522.x.

Jean-François Joanny and Jacques Prost. Active gels as a description of the actin-myosin cytoskeleton. *HFSP Journal*, 3(2):94–104, 2009. doi:10.2976/1.3054712. Publisher: Taylor & Francis.

Abhijeet Joshi, Elias Putzig, Aparna Baskaran, and Michael F. Hagan. The interplay between activity and filament flexibility determines the emergent properties of active nematics. *Soft Matter*, 15(1):94–101, 2019.

Leo P Kadanoff and Paul C Martin. Hydrodynamic equations and correlation functions. *Annals of Physics*, 24:419–469, October 1963. ISSN 0003-4916. doi:10.1016/0003-4916(63)90078-2. URL https://www.sciencedirect.com/science/article/pii/0003491663900782.

Kyogo Kawaguchi, Ryoichiro Kageyama, and Masaki Sano. Topological defects control collective dynamics in neural progenitor cell cultures. *Nature*, 545(7654):327–331, 2017. Publisher: Nature Publishing Group.

Felix C. Keber, Etienne Loiseau, Tim Sanchez, Stephen J. DeCamp, Luca Giomi, Mark J. Bowick, M. Cristina Marchetti, Zvonimir Dogic, and Andreas R. Bausch. Topology and

dynamics of active nematic vesicles. *Science*, 345(6201):1135–1139, 2014. ISSN 10959203. doi:10.1126/science.1254784.

R. Kemkemer, D. Kling, D. Kaufmann, and H. Gruler. Elastic properties of nematoid arrangements formed by amoeboid cells. *The European Physical Journal E*, 1(2):215–225, February 2000.

K Kinosita, H Itoh, S Ishiwata, K Hirano, T Nishizaka, and T Hayakawa. Dual-view microscopy with a single camera: real-time imaging of molecular orientations and calcium. *The Journal of Cell Biology*, 115(1):67–73, 1991.

Maurice Kleman and Oleg Lavrentovich. *Soft Matter Physics: An Introduction*. Springer, 2007.

Colin-Marius Koch and Michael Wilczek. Role of Advective Inertia in Active Nematic Turbulence. *Physical Review Letters*, 127(26):268005, December 2021. doi:10.1103/PhysRevLett.127.268005. URL https://link.aps.org/doi/10.1103/PhysRevLett.127.268005.

Maciej Koch-Janusz and Zohar Ringel. Mutual information, neural networks and the renormalization group. *Nature Physics*, 14(6):578–582, 2018. ISSN 17452481. doi:10.1038/s41567-018-0081-4.

K. Kruse, J. F. Joanny, F. Jülicher, J. Prost, and K. Sekimoto. Asters, Vortices, and Rotating Spirals in Active Gels of Polar Filaments. *Phys. Rev. Lett.*, 92(7):078101, February 2004. doi:10.1103/PhysRevLett.92.078101. URL https://link.aps.org/doi/10.1103/PhysRevLett.92.078101. Publisher: American Physical Society.

Nitin Kumar, Rui Zhang, Juan J. de Pablo, and Margaret L. Gardel. Tunable structure and dynamics of active liquid crystals. *Science Advances*, 4(10):eaat7779, October 2018. doi:10.1126/sciadv.aat7779. URL https://www.science.org/doi/full/10.1126/sciadv.aat7779.

Nitin Kumar, Rahul Kumar Gupta, Harsh Soni, Sriram Ramaswamy, and A. K. Sood. Trapping and sorting active particles: Motility-induced condensation and smectic defects. *Phys. Rev. E*, 99(3):032605, March 2019. doi:10.1103/PhysRevE.99.032605. URL https://link.aps.org/doi/10.1103/PhysRevE.99.032605. Publisher: American Physical Society.

Nitin Kumar, Rui Zhang, Steven A. Redford, Juan J. de Pablo, and Margaret L. Gardel. Catapulting of topological defects through elasticity bands in active nematics. *Soft Matter*, 18(28):5271–5281, 2022. doi:10.1039/D2SM00414C. URL https://pubs.rsc.org/en/content/articlelanding/2022/sm/d2sm00414c.

L. D. Landau and I. M. Lifshitz. Surfaces. Statistical Physics, 1980.

Yann Lecun, Yoshua Bengio, and Geoffrey Hinton. Deep learning. *Nature*, 521(7553):436–444, 2015. ISSN 14764687. doi:10.1038/nature14539.

Gloria Lee, Gregor Leech, Michael J. Rust, Moumita Das, Ryan J. McGorty, Jennifer L. Ross, and Rae M. Robertson-Anderson. Myosin-driven actin-microtubule networks exhibit self-organized contractile dynamics. *Science Advances*, 7(6):eabe4334, February 2021. ISSN 2375-2548. doi:10.1126/sciadv.abe4334. URL https://www.science.org/doi/10.1126/sciadv.abe4334.

Linnea M. Lemma, Stephen J. DeCamp, Zhihong You, Luca Giomi, and Zvonimir Dogic. Statistical properties of autonomous flows in 2D active nematics. *Soft Matter*, 15(15): 3264–3272, April 2019. ISSN 1744-6848. doi:10.1039/C8SM01877D. URL https://pubs.rsc.org/en/content/articlelanding/2019/sm/c8sm01877d. Publisher: The Royal Society of Chemistry.

Martin Lenz, Todd Thoresen, Margaret L. Gardel, and Aaron R. Dinner. Contractile Units in Disordered Actomyosin Bundles Arise from F-Actin Buckling. *Physical Review Letters*, 108(23):238107, June 2012. ISSN 0031-9007, 1079-7114. doi:10.1103/PhysRevLett.108.238107. URL https://link.aps.org/doi/10.1103/PhysRevLett.108.238107.

Alex J. Levine and F. C. MacKintosh. Dynamics of viscoelastic membranes. *Physical Review E*, 66(6):061606, December 2002. doi:10.1103/PhysRevE.66.061606. URL https://link.aps.org/doi/10.1103/PhysRevE.66.061606. Publisher: American Physical Society.

He Li, Xia-qing Shi, Mingji Huang, Xiao Chen, Minfeng Xiao, Chenli Liu, Hugues Chaté, and HP Zhang. Data-driven quantitative modeling of bacterial active nematics. *Proceedings of the National Academy of Sciences*, 116(3):777–785, 2019. Publisher: National Acad Sciences.

C H Lin, E M Espreafico, M S Mooseker, and P Forscher. Myosin Drives Retrograde F-Actin Flow in Neuronal Growth Cones.

Julia Ling, Andrew Kurzawski, and Jeremy Templeton. Reynolds averaged turbulence modelling using deep neural networks with embedded invariance. *Journal of Fluid Mechanics*, 807:155–166, 2016. Publisher: Cambridge University Press.

Ian Linsmeier, Shiladitya Banerjee, Patrick W Oakes, Wonyeong Jung, Taeyoon Kim, and Michael P Murrell. Disordered actomyosin networks are sufficient to produce cooperative and telescopic contractility. *Nature communications*, 7(1):1–9, 2016. Publisher: Nature Publishing Group.

M. C. Marchetti, J. F. Joanny, S. Ramaswamy, T. B. Liverpool, J. Prost, Madan Rao, and R. Aditi Simha. Hydrodynamics of soft active matter. *Reviews of Modern Physics*, 85(3): 1143–1189, July 2013. ISSN 0034-6861, 1539-0756. doi:10.1103/RevModPhys.85.1143. URL https://link.aps.org/doi/10.1103/RevModPhys.85.1143.

D. Marenduzzo, E. Orlandini, M. E. Cates, and J. M. Yeomans. Steady-state hydrodynmaic instabilities of active liquid crystals: Hybrid lattice Boltzmann simulations. *Phys. Rev. E*, 76(3):031921, 2007a.

D. Marenduzzo, E. Orlandini, and J. M. Yeomans. Hydrodynamics and rheology of active liquid crystals: A numerical investigation. *Physical Review Letters*, 98(11):3–6, 2007b. ISSN 00319007. doi:10.1103/PhysRevLett.98.118102.

Sarkis S. Margossian and Susan Lowey. [7] Preparation of myosin and its subfragments from rabbit skeletal muscle. In *Structural and Contractile Proteins Part B: The Contractile Apparatus and the Cytoskeleton*, volume 85 of *Methods in Enzymology*, pages 55 – 71. Academic Press, 1982. URL http://www.sciencedirect.com/science/article/pii/0076687985009X. ISSN: 0076-6879.

Yonit Maroudas-Sacks, Liora Garion, Lital Shani-Zerbib, Anton Livshits, Erez Braun, and Kinneret Keren. Topological defects in the nematic order of actin fibers as organization centers of Hydra morphogenesis. *bioRxiv*, 2020. Publisher: Cold Spring Harbor Laboratory.

Berta Martínez-Prat, Jordi Ignés-Mullol, Jaume Casademunt, and Francesc Sagués. Selection mechanism at the onset of active turbulence. *Nature Physics*, 15(4):362–366, April 2019. ISSN 1745-2481. doi:10.1038/s41567-018-0411-6. URL https://www.nature.com/articles/s41567-018-0411-6.

Berta Martínez-Prat, Ricard Alert, Fanlong Meng, Jordi Ignés-Mullol, Jean-François Joanny, Jaume Casademunt, Ramin Golestanian, and Francesc Sagués. Scaling Regimes of Active Turbulence with External Dissipation. *Physical Review X*, 11(3):031065, September 2021. ISSN 2160-3308. doi:10.1103/PhysRevX.11.031065. URL https://link.aps.org/doi/10.1103/PhysRevX.11.031065.

Patrick M. McCall, Frederick C. MacKintosh, David R. Kovar, and Margaret L. Gardel. Cofilin drives rapid turnover and fluidization of entangled F-actin. *Proceedings of the National Academy of Sciences*, 116(26):12629–12637, June 2019. doi:10.1073/pnas.1818808116. URL https://www.pnas.org/doi/10.1073/pnas.1818808116. Publisher: Proceedings of the National Academy of Sciences.

Pankaj Mehta and David J Schwab. An exact mapping between the variational renormalization group and deep learning. *arXiv preprint arXiv:1410.3831*, 2014.

Pankaj Mehta, Marin Bukov, Ching-Hao Wang, Alexandre G.R. Day, Clint Richardson, Charles K. Fisher, and David J. Schwab. A high-bias, low-variance introduction to Machine Learning for physicists. *Physics Reports*, 810:1–124, 2019. Publisher: Elsevier.

Prashant Mishra. SURFACE Pattern Formation in Active Nematics. (August), 2017. URL https://surface.syr.edu/etd/787.

Mehdi Molaei, Nicholas G. Chisholm, Jiayi Deng, John C. Crocker, and Kathleen J. Stebe. Interfacial Flow around Brownian Colloids. *Physical Review Letters*, 126(22):228003, June 2021. doi:10.1103/PhysRevLett.126.228003. URL https://link.aps.org/doi/10.1103/PhysRevLett.126.228003.

Mehdi Molaei, Steven A. Redford, Wen-hung Chou, Danielle Scheff, Juan J. de Pablo, Patrick W. Oakes, and Margaret L. Gardel. Measuring response functions of active materials from data, March 2023. URL http://arxiv.org/abs/2303.17785. arXiv:2303.17785 [cond-mat, q-bio].

Romain Mueller, Julia M. Yeomans, and Amin Doostmohammadi. Emergence of Active Nematic Behavior in Monolayers of Isotropic Cells. *Physical Review Letters*, 122(4):048004, February 2019. ISSN 0031-9007, 1079-7114. doi:10.1103/PhysRevLett.122.048004. URL https://link.aps.org/doi/10.1103/PhysRevLett.122.048004.

Michael P. Murrell and Margaret L. Gardel. F-actin buckling coordinates contractility and severing in a biomimetic actomyosin cortex. *Proceedings of the National Academy of Sciences*, 109(51):20820–20825, December 2012. doi:10.1073/pnas.1214753109. URL http://www.pnas.org/doi/abs/10.1073/pnas.1214753109. Publisher: Proceedings of the National Academy of Sciences.

Muneaki Nakamura, Lu Chen, Stuart C. Howes, Tony D. Schindler, Eva Nogales, and Zev Bryant. Remote control of myosin and kinesin motors using light-activated gearshifting. *Nature Nanotechnology*, 2014. ISSN 17483395. doi:10.1038/nnano.2014.147.

Vijay Narayan, Sriram Ramaswamy, and Narayanan Menon. Long-Lived Giant Number Fluctuations in a Swarming Granular Nematic. *Science*, 317(5834):105–108, 2007.

Daniel Needleman and Zvonimir Dogic. Active matter at the interface between materials science and cell biology. *Nature Reviews Materials*, 2(9):17048, July 2017. ISSN 2058-8437. doi:10.1038/natrevmats.2017.48. URL https://www.nature.com/articles/natrevmats201748.

Mehrana R Nejad, Amin Doostmohammadi, and Julia M Yeomans. Memory effects, arches and polar defect ordering at the cross-over from wet to dry active nematics. *Soft Matter*, 17(9):2500–2511, 2021. Publisher: Royal Society of Chemistry.

Sriram Ramaswamy Nitin Kumar, Harsh Soni and A. K. Sood. Flocking at a distance in active granular matter. *Nat. Commun.*, 5:4688, 2014.

Patrick W. Oakes, Elizabeth Wagner, Christoph A. Brand, Dimitri Probst, Marco Linke, Ulrich S. Schwarz, Michael Glotzer, and Margaret L. Gardel. Optogenetic control of RhoA reveals zyxin-mediated elasticity of stress fibres. *Nature Communications*, 8(1):15817, June 2017. ISSN 2041-1723. doi:10.1038/ncomms15817. URL https://www.nature.com/articles/ncomms15817.

Achini Opathalage, Michael M Norton, Michael PN Juniper, Blake Langeslay, S Ali Aghvami, Seth Fraden, and Zvonimir Dogic. Self-organized dynamics and the transition to turbulence of confined active nematics. *Proceedings of the National Academy of Sciences*, 116(11):4788–4797, 2019. Publisher: National Acad Sciences.

Sandra Palmgren, Pauli J. Ojala, Martin A. Wear, John A. Cooper, and Pekka Lappalainen. Interactions with PIP2, ADP-actin monomers, and capping protein regulate the activity and localization of yeast twinfilin. *The Journal of Cell Biology*, 155:251–260, 2001.

Aurelio Patelli, Ilyas Djafer-Cherif, Igor S Aranson, Eric Bertin, and Hugues Chaté. Understanding dense active nematics from microscopic models. *Physical review letters*, 123 (25):258001, 2019. Publisher: APS.

Walter F. Paxton, Kevin C. Kistler, Christine C. Olmeda, Ayusman Sen, Sarah K. St. Angelo, Yanyan Cao, Thomas E. Mallouk, Paul E. Lammert, and Vincent H. Crespi. Catalytic Nanomotors: Autonomous Movement of Striped Nanorods. *Journal of the American Chemical Society*, 126(41):13424–13431, 2004.

D. J. G. Pearce, J. Nambisan, P. W. Ellis, A. Fernandez-Nieves, and L. Giomi. Orientational Correlations in Active and Passive Nematic Defects. *Physical Review Letters*, 127(19): 197801, November 2021. doi:10.1103/PhysRevLett.127.197801. URL `https://link.aps.org/doi/10.1103/PhysRevLett.127.197801`.

Chenhui Peng, Taras Turiv, Yubing Guo, Qi Huo Wei, and Oleg D. Lavrentovich. Command of active matter by topological defects and patterns. *Science*, 354(6314):882–885, 2016. doi:10.1126/science.aah6936.

A. Ponti, M. Machacek, S. L. Gupton, C. M. Waterman-Storer, and G. Danuser. Two distinct actin networks drive the protrusion of migrating cells. *Science (New York, N.Y.)*, 305(5691):1782–1786, September 2004. ISSN 1095-9203. doi:10.1126/science.1100533.

Alexander Radovic, Mike Williams, David Rousseau, Michael Kagan, Daniele Bonacorsi, Alexander Himmel, Adam Aurisano, Kazuhiro Terao, and Taritree Wongjirad. Machine learning at the energy and intensity frontiers of particle physics. *Nature*, 560(7716):41–48, 2018. Publisher: Nature Publishing Group.

Salima Rafaï, Levan Jibuti, and Philippe Peyla. Effective Viscosity of Microswimmer Suspensions. *Phys. Rev. Lett.*, 104(9):098102, March 2010. doi:10.1103/PhysRevLett.104.098102. URL `https://link.aps.org/doi/10.1103/PhysRevLett.104.098102`. Publisher: American Physical Society.

S. Ramaswamy, R. Aditi Simha, and J. Toner. Active nematics on a substrate: Giant number fluctuations and long-time tails. *Europhysics Letters*, 62(2):196, April 2003. ISSN 0295-5075. doi:10.1209/epl/i2003-00346-7. URL `https://iopscience.iop.org/article/10.1209/epl/i2003-00346-7/meta`. Publisher: IOP Publishing.

Sriram Ramaswamy. The Mechanics and Statistics of Active Matter. *Annual Review of Condensed Matter Physics*, 1(1):323–345, August 2010. ISSN 1947-5454, 1947-5462. doi:10.1146/annurev-conmatphys-070909-104101. URL `http://arxiv.org/abs/1004.1933`. arXiv:1004.1933 [cond-mat, physics:physics].

W. S. Rasband. ImageJ. Technical report, U.S. National Institutes of Heath, Bethesda, Maryland, USA, 1997. URL http://rsb.info.nih.gov/ij.

Mathias Reufer, Vincent A. Martinez, Peter Schurtenberger, and Wilson C. K. Poon. Differential Dynamic Microscopy for Anisotropic Colloidal Dynamics. *Langmuir*, 28(10): 4618–4624, March 2012. ISSN 0743-7463, 1520-5827. doi:10.1021/la204904a. URL https://pubs.acs.org/doi/10.1021/la204904a.

Tyler D Ross, Heun Jin Lee, Zijie Qu, Rachel A Banks, Rob Phillips, and Matt Thomson. Controlling organization and forces in active matter through optically defined boundaries. *Nature*, 572(7768):224–229, 2019. Publisher: Nature Publishing Group.

Paul V Ruijgrok, Rajarshi P Ghosh, Sasha Zemsky, Muneaki Nakamura, Rui Gong, Lin Ning, Robert Chen, Vipul T Vachharajani, Alexander E Chu, Namrata Anand, and others. Optical control of fast and processive engineered myosins in vitro and in living cells. *Nature Chemical Biology*, 17(5):540–548, 2021. Publisher: Nature Publishing Group.

Tim Sanchez, Stephen J. DeCamp, Michael Heymann, and Zvonimir Dogic. Spontaneous motion in hierarchically assembled active matter. *Nature*, 491(7424):431–434, November 2012. ISSN 0028-0836, 1476-4687. doi:10.1038/nature11591. URL http://www.nature.com/articles/nature11591.

Ichiro Sase, Hidetake Miyata, Shin'ichi Ishiwata, and Kazuhiko Kinosita. Axial rotation of sliding actin filaments revealed by single-fluorophore imaging. *Proceedings of the National Academy of Sciences*, 94(11):5646–5650, 1997. doi:10.1073/pnas.94.11.5646. Publisher: National Academy of Sciences.

Thuan Beng Saw, Amin Doostmohammadi, Vincent Nier, Leyla Kocgozlu, Sumesh Thampi, Yusuke Toyama, Philippe Marcq, Chwee Teck Lim, Julia M Yeomans, and Benoit Ladoux. Topological defects in epithelia govern cell death and extrusion. *Nature*, 544(7649):212–216, 2017. Publisher: Nature Publishing Group.

Volker Schaller, Christoph Weber, Christine Semmrich, Erwin Frey, and Andreas R. Bausch. Polar patterns of driven filaments. *Naure*, 467:73–77, 2010.

Tony D. Schindler, Lu Chen, Paul Lebel, Muneaki Nakamura, and Zev Bryant. Engineering myosins for long-range transport on actin filaments. *Nature Nanotechnology*, 9(1):33–38, January 2014. ISSN 1748-3395. doi:10.1038/nnano.2013.229. URL https://www.nature.com/articles/nnano.2013.229. Number: 1 Publisher: Nature Publishing Group.

Jürgen Schmidhuber. Deep Learning in neural networks: An overview. *Neural Networks*, 61:85–117, 2015. ISSN 18792782. doi:10.1016/j.neunet.2014.09.003. URL http://dx.doi.org/10.1016/j.neunet.2014.09.003. Publisher: Elsevier Ltd.

Mark J. Schnitzer and Steven M. Block. Kinesin hydrolyses one ATP per 8-nm step. *Nature*, 388(6640):386–390, 1997. ISSN 00280836. doi:10.1038/41111.

Samuel Schoenholz, Eikin Cubuk, Daniel Sussman, Efthimios Kaxiras, and Andrea Liu. A structural approach to relaxation in glassy liquids. *Nature Physics*, 12(5):469–471, 2016. Publisher: Nature Publishing Group.

Daniel S. Seara, Vikrant Yadav, Ian Linsmeier, A. Pasha Tabatabai, Patrick W. Oakes, S. M. Ali Tabei, Shiladitya Banerjee, and Michael P. Murrell. Entropy production rate is maximized in non-contractile actomyosin. *Nature Communications*, 9(1):4948, November 2018. ISSN 2041-1723. doi:10.1038/s41467-018-07413-5. URL https://www.nature.com/articles/s41467-018-07413-5.

Jonathan V Selinger and Robijn F Bruinsma. Hexagonal and nematic phases of chains. I. Correlation functions. *Physical Review A*, 43(6):2910, 1991. Publisher: APS.

Anis Senoussi, Shunnichi Kashida, Raphael Voituriez, Jean-Christophe Galas, Ananyo Maitra, and André Estevez-Torres. Tunable corrugated patterns in an active nematic sheet. *Proceedings of the National Academy of Sciences*, 116(45):22464–22470, 2019. Publisher: National Acad Sciences.

Suraj Shankar and M. Cristina Marchetti. Hydrodynamics of Active Defects: From Order to Chaos to Defect Ordering. *Phys. Rev. X*, 9(4):041047, December 2019. doi:10.1103/PhysRevX.9.041047. URL https://link.aps.org/doi/10.1103/PhysRevX.9.041047. Publisher: American Physical Society.

Suraj Shankar, Sriram Ramaswamy, M. Cristina Marchetti, and Mark J. Bowick. Defect Unbinding in Active Nematics. *Phys. Rev. Lett.*, 121(10):108002, September 2018. doi:10.1103/PhysRevLett.121.108002. URL https://link.aps.org/doi/10.1103/PhysRevLett.121.108002. Publisher: American Physical Society.

Simon A. Levin Shay Gueron and Daniel I. Rubenstein. The Dynamics of Herds: From Individuals to Aggregations. *Journal of Theoretical Biology*, 182(1):85 – 98, 1996.

Meng Shen, Honghao Li, and Monica Olvera De La Cruz. Surface polarization effects on ion-containing emulsions. *Physical review letters*, 119(13):138002, 2017. Publisher: APS.

H. Y.D. Sigaki, R. F. De Souza, R. T. De Souza, R. S. Zola, and H. V. Ribeiro. Estimating physical properties from liquid crystal textures via machine learning and complexity-entropy methods. *Physical Review E*, 99(1):1–10, 2019. ISSN 24700053. doi:10.1103/PhysRevE.99.013311. Publisher: American Physical Society.

Higor Y. D. Sigaki, Ervin K. Lenzi, Rafael S. Zola, Matjaz Perc, and Haroldo V. Ribeiro. Learning physical properties of liquid crystals with deep convolutional neural networks. 2020. URL http://arxiv.org/abs/2004.01691.

Andrey Sokolov and Igor S. Aranson. Reduction of Viscosity in Suspension of Swimming Bacteria. *Phys. Rev. Lett.*, 103(14):148101, September 2009. doi:10.1103/PhysRevLett.103.148101. URL https://link.aps.org/doi/10.1103/PhysRevLett.103.148101. Publisher: American Physical Society.

Andrey Sokolov, Ali Mozaffari, Rui Zhang, Juan J. de Pablo, and Alexey Snezhko. Emergence of Radial Tree of Bend Stripes in Active Nematics. *Phys. Rev. X*, 9(3):031014, July 2019a. doi:10.1103/PhysRevX.9.031014. URL https://link.aps.org/doi/10.1103/PhysRevX.9.031014. Publisher: American Physical Society.

Andrey Sokolov, Ali Mozaffari, Rui Zhang, Alexey Snezhko, and Juan J. de Pablo. Active nematics. *Phys. Rev. X*, 2019b.

A. P. Solon, Y. Fily, A. Baskaran, M. E. Cates, Y. Kafri, M. Kardar, and J. Tailleur. Pressure is not a state function for generic active fluids. *Nature Physics*, 11:673–678, 2015.

James A. Spudich and Susan Watt. The Regulation of Rabbit Skeletal Muscle Contraction: I. Biochemical studies of the interaction of the tropomyosin-troponin complex with actin and the proteolytic fragments of myosin. *Journal of Biological Chemistry*, 246: 4866–4871, 1971.

Pragya Srivastava, Prashant Mishra, and M Cristina Marchetti. Negative stiffness and modulated states in active nematics. *Soft matter*, 12(39):8214–8225, 2016. Publisher: Royal Society of Chemistry.

Samantha Stam, Jon Alberts, Margaret L. Gardel, and Edwin Munro. Isoforms Confer Characteristic Force Generation and Mechanosensation by Myosin II Filaments. *Biophysical Journal*, 108(8):1997–2006, April 2015. ISSN 00063495. doi:10.1016/j.bpj.2015.03.030. URL https://linkinghub.elsevier.com/retrieve/pii/S000634951500291X.

Samantha Stam, Simon L. Freedman, Shiladitya Banerjee, Kimberly L. Weirich, Aaron R. Dinner, and Margaret L. Gardel. Filament rigidity and connectivity tune the deformation modes of active biopolymer networks. *Proceedings of the National Academy of Sciences*, 114(47):E10037–E10045, November 2017. doi:10.1073/pnas.1708625114. URL http://www.pnas.org/doi/abs/10.1073/pnas.1708625114. Publisher: Proceedings of the National Academy of Sciences.

Radhika Subramanian and Jeff Gelles. Two distinct modes of processive kinesin movement in mixtures of ATP and AMP-PNP. *The Journal of General Physiology*, 130(5):445–455, 2007.

Deqing Sun, Stefan Roth, and Michael J. Black. Secrets of optical flow estimation and their principles. In *2010 IEEE Computer Society Conference on Computer Vision and Pattern Recognition*, pages 2432–2439, June 2010. doi:10.1109/CVPR.2010.5539939. ISSN: 1063-6919.

Sumesh P. Thampi. *Europhys Lett.*, 2013.

Sumesh P. Thampi, Ramin Golestanian, and Julia M. Yeomans. Instabilities and topological defects in active nematics. *EPL*, 105(1), 2013a.

Sumesh P. Thampi, Ramin Golestanian, and Julia M. Yeomans. Velocity Correlations in an Active Nematic. *Physical Review Letters*, 111(11):118101, September 2013b. ISSN 0031-9007, 1079-7114. doi:10.1103/PhysRevLett.111.118101. URL https://link.aps.org/doi/10.1103/PhysRevLett.111.118101.

Sumesh P. Thampi, Ramin Golestanian, and Julia M. Yeomans. Active nematic materials with substrate friction. *Physical Review E*, 90(6):062307, December 2014a. doi:10.1103/PhysRevE.90.062307. URL https://link.aps.org/doi/10.1103/PhysRevE.90.062307.

Sumesh P. Thampi, Ramin Golestanian, and Julia M. Yeomans. Vorticity, defects and correlations in active turbulence. *Philosophical Transactions of the Royal Society A: Mathematical, Physical and Engineering Sciences*, 372(2029):20130366, November 2014b. doi:10.1098/rsta.2013.0366. URL https://royalsocietypublishing.org/doi/full/10.1098/rsta.2013.0366.

Sari Tojkander, Gergana Gateva, and Pekka Lappalainen. Actin stress fibers – assembly, dynamics and biological roles. *Journal of Cell Science*, 125(8):1855–1864, April 2012. ISSN 0021-9533. doi:10.1242/jcs.098087. URL https://doi.org/10.1242/jcs.098087.

Sander Verbrugge, Siet M.J.L. Van Den Wildenberg, and Erwin J.G. Peterman. Novel Ways to Determine Kinesin-1's Run Length and Randomness Using Fluorescence Microscopy. *Biophysical Journal*, 97(8):2287–2294, October 2009. ISSN 00063495. doi:10.1016/j.bpj.2009.08.001. URL https://linkinghub.elsevier.com/retrieve/pii/S0006349509013162.

A B Verkhovsky and G G Borisy. Non-sarcomeric mode of myosin II organization in the fibroblast lamellum. *The Journal of Cell Biology*, 123(3):637–652, 1993. doi:10.1083/jcb.123.3.637. Publisher: Rockefeller University Press.

Tamás Vicsek and Anna Zafeiris. Collective motion. *Physics Reports*, 517(3):71–140, August 2012. ISSN 0370-1573. doi:10.1016/j.physrep.2012.03.004. URL https://www.sciencedirect.com/science/article/pii/S0370157312000968.

Andrej Vilfan. Elastic lever-arm model for myosin V. *Biophysical journal*, 88(6):3792–3805, 2005. Publisher: Elsevier.

Gaszton Vizsnyiczai, Giacomo Frangipane, Claudio Maggi, Filippo Saglimbeni, Silvio Bianchi, and Roberto Di Leonardo. Light controlled 3D micromotors powered by bacteria. *Nature communications*, 8(1):1–7, 2017. Publisher: Nature Publishing Group.

R. Voituriez, J. F. Joanny, and J. Prost. Spontaneous flow transition in active polar gels. *Europhysics Letters*, 70(3):404–410, 2005. ISSN 02955075.

Matthew L Walker, Stan A Burgess, James R Sellers, Fei Wang, John A Hammer, John Trinick, and Peter J Knight. Two-headed binding of a processive myosin to F-actin. *Nature*, 405(6788):804–807, 2000. Publisher: Nature Publishing Group.

Michael Walters, Qianshi Wei, and Jeff Z.Y. Chen. Machine learning topological defects of confined liquid crystals in two dimensions. *Physical Review E*, 99(6):1–10, 2019. ISSN 24700053. doi:10.1103/PhysRevE.99.062701. Publisher: American Physical Society.

Kimberly L. Weirich, Shiladitya Banerjee, Kinjal Dasbiswas, Thomas A. Witten, Suriyanarayanan Vaikuntanathan, and Margaret L. Gardel. Liquid behavior of cross-linked actin bundles. *Proceedings of the National Academy of Sciences*, 114(9):2131–2136, 2017. ISSN 0027-8424. doi:10.1073/pnas.1616133114. URL https://www.pnas.org/content/114/9/2131. Publisher: National Academy of Sciences _eprint: https://www.pnas.org/content/114/9/2131.full.pdf.

Henricus H. Wensink, Jörn Dunkel, Sebastian Heidenreich, Knut Drescher, Raymond E. Goldstein, Hartmut Löwen, and Julia M. Yeomans. Meso-scale turbulence in living fluids. *Proceedings of the National Academy of Sciences*, 109(36):14308–14313, September 2012. ISSN 0027-8424, 1091-6490. doi:10.1073/pnas.1202032109. URL https://pnas.org/doi/full/10.1073/pnas.1202032109.

Jin Long Wu, Heng Xiao, and Eric Paterson. Physics-informed machine learning approach for augmenting turbulence models: A comprehensive framework. *Physical Review Fluids*, 7(3):1–28, 2018. ISSN 2469990X. doi:10.1103/PhysRevFluids.3.074602. Publisher: American Physical Society.

Kun-Ta Wu, Jean Bernard Hishamunda, Daniel TN Chen, Stephen J DeCamp, Ya-Wen Chang, Alberto Fernández-Nieves, Seth Fraden, and Zvonimir Dogic. Transition from turbulent to coherent flows in confined three-dimensional active fluids. *Science*, 355 (6331):eaal1979, 2017. Publisher: American Association for the Advancement of Science.

Erik Sahai Xavier Trepat. Mesoscale physical principles of collective cell organization. *Nature Physics*, 14:671–682, 2018.

Rui Zhang and Juan J. de Pablo. Dynamic Structure of Active Nematic Shells. *Nat. Commun.*, 2016.

Rui Zhang, Tyler Roberts, Igor S. Aranson, and Juan J. De Pablo. Lattice Boltzmann simulation of asymmetric flow in nematic liquid crystals with finite anchoring. *Journal of Chemical Physics*, 144(8), 2016. ISSN 00219606. doi:10.1063/1.4940342. URL http://dx.doi.org/10.1063/1.4940342.

Rui Zhang, Nitin Kumar, Jennifer L. Ross, Margaret L. Gardel, and Juan J. De Pablo. Interplay of structure, elasticity, and dynamics in actin-based nematic materials. *Proceedings of the National Academy of Sciences of the United States of America*, 115(2):E124–E133, 2017. ISSN 10916490. doi:10.1073/pnas.1713832115.

Rui Zhang, Steven A. Redford, Paul V. Ruijgrok, Nitin Kumar, Ali Mozaffari, Sasha Zemsky, Aaron R. Dinner, Vincenzo Vitelli, Zev Bryant, Margaret L. Gardel, and

Juan J. de Pablo. Spatiotemporal control of liquid crystal structure and dynamics through activity patterning. *Nature Materials*, 20(6):875–882, June 2021. ISSN 1476-4660. doi:10.1038/s41563-020-00901-4. URL https://www.nature.com/articles/s41563-020-00901-4.

Shuang Zhou, Andrey Sokolov, Oleg D. Lavrentovich, and Igor S. Aranson. Living liquid crystals. *Proceedings of the National Academy of Sciences*, 111(4):1265–1270, 2014. ISSN 0027-8424. doi:10.1073/pnas.1321926111. URL https://www.pnas.org/content/111/4/1265. Publisher: National Academy of Sciences _eprint: https://www.pnas.org/content/111/4/1265.full.pdf.

Linyang Zhu, Weiwei Zhang, Jiaqing Kou, and Yilang Liu. Machine learning methods for turbulence modeling in subsonic flows around airfoils. *Physics of Fluids*, 31(1), 2019. ISSN 10897666. doi:10.1063/1.5061693. URL http://dx.doi.org/10.1063/1.5061693.

Jiawei Zhuang, Dmitrii Kochkov, Yohai Bar-Sinai, Michael P. Brenner, and Stephan Hoyer. Learned discretizations for passive scalar advection in a 2-D turbulent flow. pages 1–12, 2020. URL http://arxiv.org/abs/2004.05477.

Angelo Ziletti, Devinder Kumar, Matthias Scheffler, and Luca M. Ghiringhelli. Insightful classification of crystal structures using deep learning. *Nature Communications*, 9(1): 1–10, 2018. ISSN 20411723. doi:10.1038/s41467-018-05169-6. ISBN: 4146701805.

Simon Čopar, Žiga Kos, Tadej Emeršič, and Uroš Tkalec. Microfluidic control over topological states in channel-confined nematic flows. *Nature communications*, 11(1):1–10, 2020. Publisher: Nature Publishing Group.